



City Research Online

City, University of London Institutional Repository

Citation: Verma, S. (2023). Evaluation of Photonic Characteristics of Plasmonic Integrated Metallic Nanoparticles with the help of Artificial Neural Network Parameterisation. (Unpublished Doctoral thesis, City, University of London)

This is the accepted version of the paper.

This version of the publication may differ from the final published version.

Permanent repository link: <https://openaccess.city.ac.uk/id/eprint/31411/>

Link to published version:

Copyright: City Research Online aims to make research outputs of City, University of London available to a wider audience. Copyright and Moral Rights remain with the author(s) and/or copyright holders. URLs from City Research Online may be freely distributed and linked to.

Reuse: Copies of full items can be used for personal research or study, educational, or not-for-profit purposes without prior permission or charge. Provided that the authors, title and full bibliographic details are credited, a hyperlink and/or URL is given for the original metadata page and the content is not changed in any way.

City Research Online:

<http://openaccess.city.ac.uk/>

publications@city.ac.uk

**Evaluation of Photonic Characteristics of
Plasmonic Integrated Metallic
Nanoparticles with the help of Artificial
Neural Network Parameterisation**



Sneha Verma

School of Science and Technology

City, University of London

This dissertation is submitted for the degree of

Doctor of Philosophy

September 2023

I would like to dedicate this thesis to my parents and siblings...

Declaration

I, hereby declare that except where specific reference is made to the work of others, the contents of this dissertation are original and have not been submitted in whole or in part for consideration for any other degree or qualification in this, or any other university. This dissertation is my own work and contains nothing which is the outcome of work done in collaboration with others, except where specified in the text.

Sneha Verma

September 2023

Acknowledgements

I am thankful to almighty for giving me strength and ability to understand, learn, keeping me motivated and enthusiastic throughout my journey. I would like to thank my supervisor, Professor B. M. A. Rahman, for having me as a student and providing me persistent support, insightful advice, encouraging conversations throughout the duration of my graduate research, and makes everything today come true.

I am also very thankful to City University of London to award me scholarship for my PhD degree because of their immense support and infrastructure my studies are smoothly carrying out.

I also would like to thank every member and alumni of the Photonics Modelling Research group especially, I also want to extend my sincere thank to Dr. Souvik Ghosh and Dr. Sunny Chugh for all their constructive time, technical and moral support. Without their guidance and encouragement, I cannot imagine myself growing so fast for the past three years. I wish the best to your future career and academic achievements.

I am also very grateful to my friends for their never ending support and encouragement throughout my studies. Finally, I want to thank my parents, who always encourage me to insist my own dream at any cost. I will never stop my pace to pursue the career I love in the future.

Abstract

Plasmonic Nanostructures with its highly Localised Surface Plasmon Resonance (LSPRs), have opened up excellent opportunities for molecular biosensing applications. This PhD work studies a novel elliptical shaped gold nano antenna array surface as a sensing platform for Refractive Index (RI) diagnostics by using the finite element method (FEM) of COMSOL Multiphysics package. In this work, initially various computational approaches for characterising nanoantennas are benchmarked. Then, effect of various nano antenna parameters are optimised to achieve a high sensitivity and uniformity of the sensor chips. It has been shown that nanoantenna array with major axes (a) = 100 nm, minor axes (b) = 10 nm, height (h) = 40 nm and separation gap (g) = 10 nm with unit cell period of 400x200 nm yielding a very high sensitivity of 526-530 nm/RIU, FWHM = 110 nm and FOM = 8.1. Next, a hybrid coupled nano-structured antenna with stacked multilayer gold and Lithium Tantalate ($LiTaO_3$) or Aluminum Oxide (Al_2O_3) is designed. A 10 layers of gold (Au) and Lithium tantalate ($LiTaO_3$) or Aluminum oxide (Al_2O_3) with $h_1 = h_2 = 10$ nm exhibits very high bulk sensitivity (S) of 730 and 660 nm/RIU, respectively with major axis, (a) = 100 nm, minor axis, (b) = 10 nm, separation gap (g) = 10 nm, and height, (h) = 100 nm, which is a significant increase in its sensitivity (S). This innovative novel plasmonic hybrid nanostructures provide a framework for developing plasmonic nanostructures for use in various sensing applications. Additionally, as an alternative to the use of computationally expensive FEM, use of multi layer perception (MLP) deep learning method is developed with the help of Pytorch and scikit learn frameworks. The training of MLP model has been carried

out with the help geometrical data as a input layer and predicted the sensitivity, Full-Width Half-Maximum (FWHM), Figure of Merit (FOM), plasmonic wavelength and the spectral patterns of reflection, transmission and absorption spectra. The efficacy and reliability of the design strategy are confirmed through conventional FEM validations and evaluation shows that over 95 % accuracy and 40 time faster computational cost as compare to the conventional FEM method.

Table of contents

List of symbols and acronyms	xv
List of figures	xix
List of tables	xxix
Publications	xxxii
1 Introduction	1
1.1 Objectives and Motivations of Nano technology	1
1.2 Objectives and Motivations of Machine Learning	3
1.3 Challenges	5
1.4 History and Literature	6
1.4.1 Nanostructures	6
1.4.2 Nano materials	8
1.4.3 Artificial Intelligence	11
1.5 Outlines	12
2 Overview of Numerical Methods of Electromagnetics field theory	17
2.1 Maxwell's Equations	17
2.1.1 Differential Form	17
2.1.2 Integral Form	18

Table of contents

2.1.3	Constitutive Relations	19
2.1.4	The Wave Equations	20
2.2	Numerical Calculations: Finite Element Method	22
2.3	Surface Plasmon Resonance	23
2.3.1	Mathematical Description of Surface Plasmon Polaritons	25
2.4	Drude Free Electron Theory	28
2.5	LSPR on Nanospheres	31
2.6	COMSOL Model Methodology and Validation	33
2.6.1	Mie Theory	33
2.6.2	Gold nano sphere in air/water	34
2.6.3	Periodic Gold Nano Disk	40
2.6.4	Array of Gold Nano Holes	41
2.7	Mesh Considerations	42
2.8	Summary	44
3	Conceptualization of elliptical nano structures	47
3.1	Introduction	47
3.2	Expansion for Nanostructured Geometries	50
3.3	Plasmonic Interactions	52
3.3.1	Nanostructure-Substrate Coupling	52
3.3.2	Sensing Mechanisms of Nanoparticles	53
3.4	Summary	54
4	All-Opto plasmonic controlled bulk and surface sensitivity analysis of paired nano-structured antenna with label-free detection approach	55
4.1	Introduction	55
4.2	Numerical Methods and Model Optimization	56

4.2.1	Paired Elliptical shaped Nano Antenna	61
4.2.2	LSPR sensing calculation of optimised structure	66
4.3	Surface sensing Outcomes of the Paired Elliptical nano structured antenna .	71
4.3.1	Model Investigation and Its Applications	73
4.4	Summary	75
4.5	Novelties and Highlights	76
5	Artificial Neural Network Modelling for Optimizing the Optical Parameters of Plasmonic Paired Nanostructures	79
5.1	Introduction	79
5.2	The Convergence of Machine Learning with Nanostructural Devices	82
5.2.1	Artificial Neural Networks for Prediction of Output Parameters of Nanophotonic Structures	86
5.2.2	The Architecture of the Multilayer Artificial Neural Network	87
5.3	Neural Network Analysis with Empirical Evidences	92
5.3.1	Sensitivity (nm/RIU)	92
5.3.2	Plasmonic Wavelength	96
5.3.3	Full-Width Half Maximum (FWHM)	100
5.4	Comparison of Computational and Numerical Simulations Performance . .	101
5.5	Summary	103
6	Deep learning for spectral prediction and prospective validation of nanostructured dimers	105
6.1	Introduction	105
6.2	Deep Learning (<i>DL</i>) paradigm and its synchronizations with nanotechnology	107
6.3	Architectural framework of <i>DL</i> neural network with Empirical attestation .	111
6.4	Results and Discussion	112

Table of contents

6.5	Substantiation of in-house developed <i>DL</i> neural network for concealed nanostructures	121
6.5.1	Evaluation of in-house developed <i>DL</i> neural network for imperceptible geometric dimensions (beyond the training dataset)	123
6.5.2	Evaluation of in-house developed neural network on the experimental spectra	124
6.6	Summary	125
7	Advanced refractive index sensor using 3-dimensional metamaterial based nanoantenna array	127
7.1	Introduction	127
7.1.1	Approaches for computational design and optimization	130
7.2	The parameterized investigation of the multi layered structure	133
7.2.1	Performance of multi-layered elliptical shaped antenna stacked with Al_2O_3 and $LiTaO_3$	135
7.2.2	Study of field distribution around the single metal and ten layered (5 Pairs of gold and $LiTaO_3$ stacked elliptical shaped antenna	136
7.3	Effect of the separation distance on the $LiTaO_3$ and Al_2O_3 stacked nano structure.	139
7.4	Summary	142
8	Conclusion and Future Work	143
8.1	Future Scope	147
8.1.1	Future possibilities in the LSPR based sensors	147
8.1.2	Future possibilities in the Artificial intelligence based optical properties predictions	148
	References	151

List of symbols and acronyms

Symbols

c	Light velocity in free-space
μ	Magnetic permeability
ε	Electrical permittivity
$\varepsilon_m(\omega)$	Frequency dependent dielectric constant of a metal
$\varepsilon_d(\omega)$	Frequency dependent dielectric constant of dielectric
ω_p	Plasmon angular frequency
ε_r	Relative permittivity
ω_{SP}	Surface plasmon frequency
N	Conduction electron density
m_0	Effective optical mass
γ	Electron plasma oscillations
τ	Relaxation time
k_0	Wave vector
ω_{LSP}	Localized surface plasmon frequency
β	Propagation constant
λ_{res}	Resonating wavelength
δ	Environment refractive index

List of symbols and acronyms

E_x	Electric field in x-direction
E_y	Electric field in y-direction
E_z	Electric field in z-direction
h	Height of the antenna
g	Separation gap between the antennas
a	Major axis of the elliptical antenna
b	Minor axis of the elliptical antenna
d	Diameter of a circular antenna
n	Refractive index of surrounding media
n_s	Surrounding media of surface layer
λ	Wavelength
n_{eff}	Effective refractive index
Δn_{eff}	Effective index difference
k_0	Wavenumber
A_{eff}	Mode effective area
ϵ_0	Permittivity of free-space
Si	Silicon
SiO_2	Silicon dioxide

Acronyms

RI	Refractive index
IR	Infrared Region
EM	Electromagnetic
RF	Radio frequency
TE	Transverse electric

TM	Transverse magnetic
S	Sensitivity
PEC	Perfect electric conductor
PMC	Perfect magnetic conductor
PML	Perfectly matched layer
SBC	Scattering boundary condition
SPR	Surface plasmon resonance
LSPR	Localised surface plasmon resonance
SPW	Surface plasmon waves
SPP	Surface plasmon polaritons
FEM	Finite element method
FDTD	Finite difference time domain method
FWHM	Full width half maximum
FOM	Figure of merit
ML	Machine learning
MSE	Mean squared errors
AI	Artificial Intelligence
ANN	Artificial neural network
RELU	Rectified linear activation function
SGD	Stochastic gradient descent optimizer
GPU	Graphical processing unit
CPU	Central processing unit
MLP	Multi-layer perception
NaCl	Sodium chloride

List of figures

1.1	Nano Antenna Structures (a) Traditional RF Antenna System, (b) Designed nano antenna structure placed on the quartz substrate.	2
1.2	Categorical analysis of Nano Materials [35].	9
1.3	Classification of structures Nano-materials [36].	10
1.4	Classification properties of Nano-Structures	10
2.1	Schematic of Interaction of electric field with gold nanospheres resulting in electron cloud oscillation.	23
2.2	Schematic of Dielectric (ϵ_d) and Metal ($\epsilon_m(\omega)$) Semi-Infinite Interface Supporting SPP Propagation.	25
2.3	Comparison of Dispersion Curves for Surface Plasmon Polaritons (SPP) (black line) and Incident Light (blue line) Showing Wavevector Mismatch.	27
2.4	Real (a) and Imaginary (b) counterparts of dielectric constant of gold obtained from [65].	30
2.5	Comparison of in-house simulated results with already published work (a) Shows the absorption spectra of gold nano sphere of 10 nm radius. (b) Shows the absorption spectra of gold nano sphere of 20 nm radius. (c) Shows the absorption spectra of gold nano sphere of 40 nm radius. (d) Shows the absorption spectra of gold nano sphere of 70 nm radius, and all the referenced results are taken from [74] and compared with the my own model.	35

List of figures

2.6	Comparison of published results [74] with the in-house generated model the extinction Spectra of standalone gold nano sphere in air domain (a) 10 nm gold nano sphere in air (b) 20 nm gold nano sphere in air (c) 40 nm gold nano sphere in air (d) 70 nm gold nano sphere in air.	36
2.7	Comparison of in-house simulated model with the extracted [74] Scattering Spectra of standalone gold nano sphere in air domain (a) 40 nm gold nano sphere in air (b) 70 nm gold nano sphere in air.	37
2.8	Comparison of in-house simulated and extracted from [75] (a) Extinction Efficiency of standalone gold nano sphere of 40nm dia in water (b) Shows the inhouse simulated Normalised Electric Field of nano Sphere (c) Normalized electric field profiles profile reprinted from published article [75].	38
2.9	Response of the 40 nm in-house simulated nano sphere in different surrounding medium (a) Absorption efficiency of standalone 40 nm gold nano sphere in mentioned refractive indexes. (b) Scattering efficiency of the same structure (c) Extinction efficiency response of the different RIs.	38
2.10	Response of in-house simulated nano spheres submerged in water (a) Scattering coefficients of nano spheres (b) Absorption coefficients of the same structure (c) Extinction coefficients response of nano spheres with different radius.	39
2.11	Response of in-house simulated gold nano disk in different RIs (a) Absorption Efficiency of stand alone gold nano disk in different RIs (b) Linear Relation with RI and wavelengths (c) Model Profile of normalized Electric Field from the in-house simulated model.	40
2.12	Mode field distribution of in-house developed gold nano hole in water (a) Figure taken from [77] (b) In-house developed mode field distribution of the nano holes.	42

2.13	Transmission Spectra of in-house simulated gold nano holes (a) Shows the transmission spectra of gold nano hole when height is fixed at 50nm (b) Comparison of generated and extracted Transmission spectra of (c) Model profiles of 150nm gold nano holes with transmission spectra.	43
3.1	Schematic of (a) Sphere (b) Prolate ellipsoids (c) Oblate ellipsoids with Semi-Axis Lengths, a , b and c in x , y and z directions respectively.	50
3.2	Schematic of short and long axis oscillations of transverse and longitudinal resonance modes respectively.	52
3.3	Schematic representation of nano ellipsoid coupled to dipole image charges in substrate.	53
4.1	Designed model on COMSOL Multiphysics (a) Top and Side views of a paired elliptical shaped gold nano antenna (b) Computational model of paired gold nano antenna along with the boundary conditions.	57
4.2	Work approach of the designed computation model.	58
4.3	Sensitivity variation with the diameter of single nano disk of 10 nm, 40 nm and 80 nm height, sphere and single elliptical disk when $a = 100$ nm, $b =$ varied (10 nm to 100 nm), $h = 40$ nm.	60
4.4	(a) E_x , mode field profile of a single elliptical disk antenna when $a = 100$ nm, $b = 10$ nm and $h = 40$ nm (b) Electric field variation along the x -axis for a single elliptical disk when $a = 100$ nm, $b = 10$ nm and $h = 40$ nm.	61
4.5	(a) Transmission Spectra of paired 100 nm circular nano disk with 10 nm separation distance and 40 nm height (b) Sensitivity and R-Square Error calculation of 100 nm and 50 nm paired circular disk.	62
4.6	Sensitivity analysis of paired circular nano disk of 50 nm, 100 nm and 150 nm diameter with the different separation distance.	63

List of figures

4.7	(a) Transmission spectra of the optimized paired elliptical antenna with 100 nm, 10 nm major and minor axes, respectively with 10 nm separation distance g and 40 nm height, h (b) Absorption Spectra of the same structure (c) E_x , mode field profile of the optimized paired structure (d) Variation of Electric field along the x -direction of the optimized elliptical disk of 100 nm paired circular nano disk with 10 nm separation distance, g and 40 nm height, h	65
4.8	(a) Polynomial Fit at when a axes were at 100 nm, 80 nm and 60 nm at RI from 1.0 to 1.8 (b) Sensitivity variation with the minor, b when major axis, a were fixed at either 100 nm, 80 nm or 60 nm and with fixed at 10 nm separation gap, g and height, $h = 40$ nm.	67
4.9	(a) Variation of FWHM with the different minor axes, b when major and separation gap were fixed at 100 nm and 10 nm, respectively (b) Comparison of Figure-of-Merit (FOM) calculation at different minor axes when major axis and gap were fixed at 100 nm and 10 nm respectively.	68
4.10	(a) Sensitivity comparison of Single, Double disk and optimized Paired elliptical nano antenna with 10 nm separation gap and 100 nm major axes. (b) Sensitivity comparison of the variation of major axes a , minor axes b and paired disk variable.	70
4.11	(a) Transmission spectra for surface sensing of the optimized paired elliptical antenna disk when $a = 100$ nm, $b = 10$ nm, $h = 40$ nm, $g = 10$ nm and surface layer thickness = 4.5 nm (b) Surface sensitivity analysis of the optimized elliptical disk when $a = 100$ nm, $b = 10$ nm, $h = 40$ nm.	72
4.12	(a) Shows the transmission spectra of different IPA concentrations (b) Demonstrate the FWHM variation of 2-propanol (IPA) with different RIs (c) Shows the resonating plasmonic wavelength with refractive index values (d) Shows the shift in resonating wavelength with the 2-propanol (IPA) concentration.	75

5.1	(a) Schematic of circular and elliptical nanostructures placed on a quartz substrate (b) Mode profile E_x of paired gold (i) elliptical and (ii) circular nanoantennas (c) The line plot of the electric field confinement in the separation gap and at the corners of the nanoantennas.	84
5.2	Outlayer of Artificial Neural Network.	88
5.3	Mean squared error calculation for the above shown dataset in Table. 5.1: (a) The mean squared error at different hidden layers with 50 nodes (neurons) (b) Neuron variation in hidden layers.	91
5.4	The scatter plot of a data point location: (a) The comparison of the training, validation, and test data set (b) The efficiency of the developed neural network with epoch variance, with the comparison of actual sensitivity (nm/RIU) values (from the simulation) with respect to predicted values (calculated from the neural network).	93
5.5	Sensitivity visualization: (a) the predicted sensitivity over the major axes (nm) at different epochs (b) a contour plot of the absolute error values for sensitivity predictions over the major axes (nm) (c) the sensitivity response against the minor axes (nm) with epoch variation.	94
5.6	The scatter plot of a data point location shows improvement on a developed neural network with different epochs.	97
5.7	Plasmonic wavelength (nm) visualization: (a) the predicted plasmonic wavelength (nm) with major axes (nm) variation at different epoch; (b) the plasmonic wavelength (nm) response against the minor axes (nm) with epoch variation.	98

List of figures

5.8	Sensitivity (nm/RIU) and Plasmonic wavelength (nm) visualization: (a) show actual sensitivity (nm/RIU) and plasmonic wavelength (nm) response with predicted sensitivity (nm/RIU) and plasmonic wavelength (nm) over the major axis (nm) (b) the difference between actual predicted sensitivity (nm/RIU) and plasmonic wavelength (nm) and predicted sensitivity and (nm/RIU) plasmonic wavelength (nm) over the minor axis (nm).	99
5.9	FWHM (nm) visualization: (a) the predicted FWHM (nm) with major axes (nm) variation at different epochs (b) shows the FWHM (nm) response against the minor axes (nm) with epoch variation.	100
6.1	Schematic of the extended unit cell elliptical and circular nano antenna and its optical response in terms of transmitted and reflection spectra.	107
6.2	Schematic of the structure of two elliptical and circular nanostructures on SiO_2 substrate (The top and front views of a single unit cell with the geometrical parameters are represented in the insets). (b) A <i>DL</i> neural network model that predicts the optical response over a wavelength range for the given geometrical parameters (c) Shows the predicted optical response for a given geometrical structure.	109
6.3	Histogram of the Input and Output datasets for elliptical and Circular paired nano structure. (a) Shows the scaled input (Major, Minor Axis and Separation Distance) dataset used to train the neural network. (b) Shows the trend of the Output (Reflection, Transmission and Absorption Spectra) dataset used to train the developed neural network	113
6.4	Shows the <i>MSEs</i> values for 1, 3 and 5 <i>hidden layers</i> when <i>neurons</i> = 50 and <i>epoch</i> = 5000.	114

6.5 *Hidden layer = 1, Neurons = 50 and Epoch = 5000* (a) Shows the comparison between the predicted transmission spectra with respect to the original transmission spectra. (b) Shows the anticipated reflection spectra are compared to the original reflection spectra. (c) Shows the predicted absorption spectra against the original absorption spectra. 115

6.6 *Hidden layer = 5, Neurons = 50 and Epoch = 5000* (a) Shows the comparison between the predicted transmission spectra with respect to the original transmission spectra. (b) Shows the anticipated reflection spectra are compared to the original reflection spectra. (c) Shows the predicted absorption spectra against the original absorption spectra. 116

6.7 (a) Shows the computational Cost (Sec) for the *DL* neural network training with respect to different *epoch* (b) Represents the comparison in computational cost at different *hidden layers*. 117

6.8 *Hidden layers= 5 and Epoch = 5000* (a) Shows the comparison of predicted reflection spectra with respect to the original reflection spectra at *neuron = 1* (b) Represents the resemblance of predicted reflection spectra with respect to the original reflection spectra at *neuron = 30* 119

6.9 *Hidden layer = 5 and Epoch = 5000* (a) Shows the comparison of *MSEs* at different *neurons* (b) Represents the trend of the computational cost with respect to the variations in *neurons* 120

List of figures

- 6.10 *Hidden layer = 5, Neurons = 50 and Epoch = 5000* (a) Shows the comparison between the predicted transmission spectra with respect to the original transmission spectra when $d = 70$ nm, $g = 20$ nm and $h = 40$ nm. (b) Shows the anticipated reflection spectra are compared to the original reflection spectra $d = 70$ nm, $g = 20$ nm and $h = 40$ nm. (c) Shows the predicted absorption spectra against the original absorption spectra $d = 70$ nm, $g = 20$ nm and $h = 40$ nm. 122
- 6.11 *Hidden layer = 5, Neurons = 50 and Epoch = 5000* (a) Shows the comparison between the predicted transmission spectra against the original transmission spectra when $a = 155$ nm, $b = 55$ nm, $g = 35$ nm and $h = 40$ nm. (b) Shows the anticipated reflection spectra are compared to the original reflection spectra $a = 155$ nm, $b = 55$ nm, $g = 35$ nm and $h = 40$ nm. 123
- 6.12 *Hidden layer = 5, Neurons = 50 and Epoch = 5000* (a) Shows the comparison between the predicted transmission spectra with respect to the experimental transmission spectra when $a = 110$ nm, $b = 35$ nm, $g = 17$ nm and $h = 40$ nm. (b) Shows the anticipated reflection spectra are compared to the experimental reflection spectra $a = 110$ nm, $b = 35$ nm, $g = 17$ nm and $h = 40$ nm. 124
- 7.1 (a) Schematic of the computational domain designed on the FEM method enabled commercial software (b) Graphical representation of the designed hybrid refractive index sensor (c) Transmission spectra of the optimized paired elliptical nano structure with major axis, $a = 100$ nm and minor axis, $b = 10$ nm. 132
- 7.2 (a) Shows the performance of the single, coupled circular and coupled elliptical shaped gold nano antenna (b) Shows the sensitivity performance of the two-layer hybrid nanoantenna. 134

7.3 (a) Shows the sensitivity performance single metallic (Au) and Al_2O_3 stacked antenna when total height, $h = 100$ nm with or without stacked (b) Shows the sensitivity performance single metallic (Au) and $LiTaO_3$ stacked antenna when total height, $h = 100$ nm with or without stacked. 136

7.4 (a) Electric field distribution along the x plane in the gold elliptical and circular paired structure when $a = 100$ nm, $b = 10$, $g = 10$ nm and $h = 10$ (b) Electric field distribution along the x plane in the single gold and stacked 10 layers (with $LiTaO_3$ or Al_2O_3) elliptical paired structure when $a = 100$ nm, $b = 10$, $g = 10$ nm and $h_1 = h_2 = 10$ nm. (c) E_y , mode field profile of a single metallic elliptical nano structure when $a = 100$ nm, $b = 10$ nm, and $h = 100$ nm along the $x - z$ plane (d) Electric field variation along the $x - z$ plane for a 10 layered $LiTaO_3$ stacked nano structure when $a = 100$ nm, $b = 10$ nm, and $h_1 = h_2 = 10$ nm. 138

7.5 (a) E_x , mode field profile in the $x - y$ plane of a single metallic elliptical nano structure when $a = 100$ nm, $b = 10$ nm, and $h = 100$ nm (d) Electric field profile in the $x - y$ plane for a 10 layered $LiTaO_3$ stacked nano structure when $a = 100$ nm, $b = 10$ nm, and $h_1 = h_2 = 10$ nm. 139

7.6 Sensitivity comparison of 10 layered stacked antenna (5 gold layers with $h_1 = 10$ nm gold and 5 $LiTaO_3/Al_2O_3$ layers with $h_2 = 10$ nm) with respect to separation distance. 140

List of tables

2.1	Electromagnetic quantities and units	19
4.1	Comparison of published work with the optimized paired structure.	73
4.2	Comparison of published work with the optimized paired structure.	74
5.1	Dataset variation used for neural network training.	87
5.2	Comparison between actual and predicted values within the range.	102
5.3	Comparison between actual and predicted values outside the range.	103

Publications

Journals

1. **Sneha Verma**, Sunny Chugh, Souvik Ghosh and B. M. A. Rahman, "Artificial Neural Network Modelling for Optimizing the Optical Parameters of Plasmonic Paired Nanostructures," *Nanomaterials*, vol. 12, no. 1, pp. 170, 2022. <https://www.mdpi.com/2079-4991/12/1/170>
2. **Sneha Verma**, Souvik Ghosh, and B. M. A. Rahman, "All-Opto Plasmonic-Controlled Bulk and Surface Sensitivity Analysis of a Paired Nano-Structured Antenna with a Label-Free Detection Approach," *Sensors*, vol. 21, no. 19, pp. 6166, 2021. <https://www.mdpi.com/1424-8220/21/18/61664>
3. **Sneha Verma**, Sunny Chugh, Souvik Ghosh and B. M. A. Rahman, "Deep learning for spectral prediction and prospective validation of nano structured dimers," *Scientific Reports*. <https://doi.org/10.1038/s41598-023-28076-3>
4. **Sneha Verma** and B. M. A. Rahman, "Computational Investigation of Advanced Refractive Index Sensor Using 3-Dimensional Metamaterial Based Nanoantenna Array," *Sensors*. <https://doi.org/10.3390/s23031290>
5. B. M. Azizur Rahman, Charusluk Viphavakit, Ratchapak Chitaree, Souvik Ghosh, A. K. Pathak, **Sneha Verma** and Natsima Sakda, "Optical Fiber, Nanomaterial, and

Publications

- THz-Metasurface-Mediated Nano-Biosensors: A Review,” *Biosensors*, vol. 12, no. 1, pp. 42, 2022. <https://www.mdpi.com/2079-6374/12/1/42>
6. B. M. Azizur Rahman, Charusluk Viphavakit, Ratchapak Chitaree, Souvik Ghosh, A. K. Pathak, **Sneha Verma** and Natsima Sakda, “A Review on heavy metal detection,” *Biosensors*. [Ready for Submission](#)
7. **Sneha Verma**, A. K. Pathak, and B. M. Azizur Rahman, “Review and affirmation of Plasmonic Enhanced Nano Particles and their potential meta-material advancements,” *Biosensors*. [Under Consideration](#)
8. A. K. Pathak, **Sneha Verma**, Natsima Sakda, Charusluk Viphavakit, Ratchapak Chitaree, and B. M. Azizur Rahman, “Recent advances in optical hydrogen sensor including use of metal and metal alloys: A review,” *Photonics*. 2023, 10(2), 122. <https://doi.org/10.3390/photonics10020122>.

Conferences

1. **Sneha Verma** and B. M. A. Rahman, “Advanced refractive index sensor using 3-dimensional metamaterial based nanoantenna array,” in *Journal of Physics: Conference Series, Fifth International Conference on Applications of Optics and Photonics (AOP2022)*, 2022. [doi:10.1088/1742-6596/2407/1/012054](https://doi.org/10.1088/1742-6596/2407/1/012054)
2. **Sneha Verma**, Souvik Ghosh and B. M. A. Rahman, “Sensitivity analysis of a label-free detection using Opto-plasmonic nano-structured antenna,” in *IEEE International Conference on Sensors and Nanotechnology (SENNANO)*, 2021. <https://ieeexplore.ieee.org/document/9642511>
3. **Sneha Verma**, Sunny Chugh, Souvik Ghosh and B. M. A. Rahman, “Artificial Neural Networks for Sensitivity Estimation of Paired Nano Particles,” in *The 34th IEEE*

*International Conference on Tools with Artificial Intelligence (ICTAI), 2022. Under
Consideration*

Chapter 1

Introduction

1.1 Objectives and Motivations of Nano technology

The main concept of the paired gold nano antenna are recently gaining lot of popularity among all researchers due to its versatile application and, establishing a new perspective for the development of nano technology for optical bio-sensing applications. Nano shaped antenna can be a good aspirant for the micro level bio sensing application due to its exciting property called Localized Surface Plasmon Resonance (*LSPR*). *LSPRs* have extremely high electromagnetic field confinements, making them an excellent contender for bio-molecular sensor applications including like biomedical detection, photovoltaic cells, spectroscopy, energy generation, and disease therapy and avoidance. Nanotechnology has garnered tremendous popularity in recent years due to its great efficiency in terms of scattering, absorption, extinction, and reflection/transmission at the nanoscale.

Figure 1.1 shows the structural comparison between traditional RF and nano optical antenna. Figure 1.1a shows a traditional Yagi-Uda RF antenna, which can be 1 m long and Figure 1.1b shows a sub micron size optical nano antenna along with its prominent results due to their property called as Surface Plasmon Resonance (*SPR*), and due to its compact

Introduction

size and structure it can be extremely useful to overcome a number of challenges for many applications.

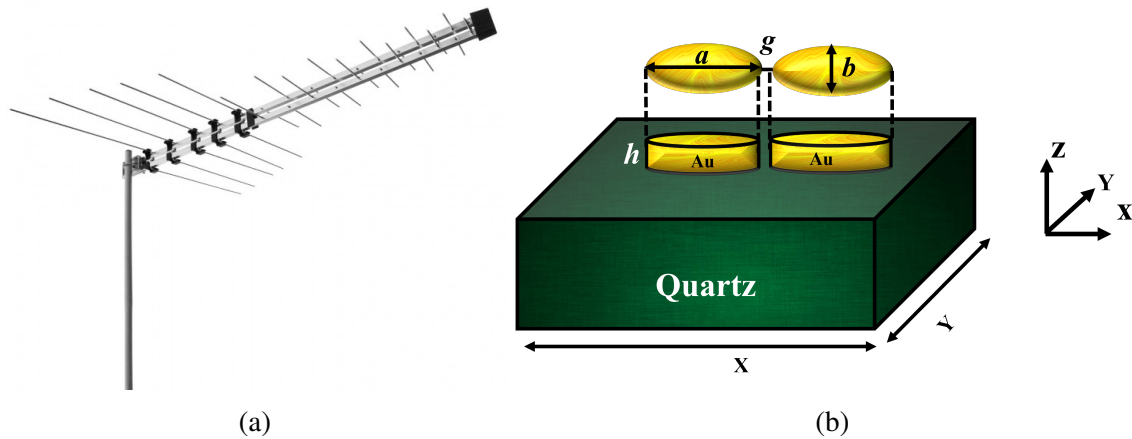


Fig. 1.1 Nano Antenna Structures (a) Traditional RF Antenna System, (b) Designed nano antenna structure placed on the quartz substrate.

Figure. 1.1b shows a nano sensing platform which can be utilised for a range of purposes, with environmental monitoring and biosensing applications possible through the addition of a sensing platform. Ideally, a biosensor must be cost-effective and user-friendly with the ability to obtain stable and reproducible results in a timely manner. Additionally, the sensor must be both sensitive and specific to the required detection events. As a consequence, optical nanosensors for biological diagnostic applications must be able to detect and efficiently monitor biomolecules, providing a signal proportional to the molecule concentration by modifying the geometries and ambient media; although, there are still many possibilities to consider. As a result, I have developed an effective refractive index sensor based on nanostructures in this research.

Many industrial applications, including the development of photonic devices, need time-consuming stages such as design, optimisation, manufacturing, characterization, error analysis, and potential reconfiguring. Several mathematical simulations and software pack-

1.2 Objectives and Motivations of Machine Learning

ages (both open platform and commercialized) have been created for diverse nano photonic applications to reduce both costs and time of the development process. With the growth of computing technology, the accuracy of these modelling tools has rapidly increased. 2-D and 3-D optical devices may be studied using a variety of models and simulators. Although approximate two-dimensional computations can elucidate some concepts and phenomena, but comprehensive three-dimensional computations are required to determine the characteristics of practical devices that will be employed in real systems. Furthermore, depending on the size of the optical device, studying the temporal response of the nano structures might render the modelling procedure computationally costly.

To study the plasmonic response of 3-D nano structures, the Finite Element Method (*FEM*) approach is often adopted, and it typically consists of a triangular mesh with one grid resolution for the *FEM*. For complex devices with curved edges, this grid approach can become inefficient. To address this, an in-house Finite Element Method (*FEM*) model was created, which employs a very small sized triangular mesh and allows for varying mesh resolutions in the computational domain. Despite the availability of super computing machines, a thorough optimization of plasmonic nano structured device parameters by parameter sweep is typically a time-consuming procedure as the *FEM* approach can take a few hours or even a days to evaluate its optical transmission response.

1.2 Objectives and Motivations of Machine Learning

Machine learning algorithms have been used in the day-to-day applications of tech firms such as Google, Microsoft, Facebook and others. Machine learning (*ML*) approaches have recently been applied to optical systems to effectively optimise various optical characteristics at a reduced computation cost. This provides an inspiration to investigate the new field of using machine learning algorithms to effectively predict the optical characteristics for various nano structured plasmonic devices. The aim here is to achieve automatised *ML* neural

Introduction

network that can adapt the changes in the geometrical dimensions and have the ability to predict the optical properties in a small computational time. Although, when it comes to the experimental fabrication such uncertainties may come about if the system is very dynamic or complex. Hence, this problem can be solved with the help of neural network.

The design of neural network is important as it is very difficult to observe and calculate the optical characteristics and make immediate understanding through observing. The *ML* has shown to be a promising approach for enhancing the potential of monitoring the nano structured devices. *ML* neural network can also learn the patterns from the generated data by using the *FEM* method and provides interesting insights of the training dataset, and assist the neural network in making additional predictions and conclusions. Generated training dataset acts as an automated reasoning tool to overcome the aforementioned *FEM* uncertainty.

In addition, conventional *FEM* method consumes considerable computing resources and time to achieve the desired outcomes. Even a tiny mistake in the *FEM* model input parameters may lead to unacceptable optical properties. Conversely, most *ML* models (especially supervised learning) are straight-forward statistical mapping algorithms between the system inputs and outputs. They have the potential to bypass the problems associated with complex traditional models and solve the prediction problem in a reverse way using monitoring. Therefore, given the *ML* neural network capability, intelligent learning agents can calculate accurate and cost effective desired optical characteristics.

Finally, in the following work I have designed high sensitive nano antenna device for RI detection using the conventional *FEM* method. In the second phase, the *ML* algorithm have been developed to overcome the computation cost of the system. The designed algorithm shows its effective performance for predicting the optical characteristics of the nano structured antenna.

1.3 Challenges

In the initial part of this project, traditional *FEM* software was utilised to construct the nano antenna computation model. However, I employed a variety of methodologies and boundary conditions for building the nano antenna system. But, in order to be confident in the computational model design, I adopted one reputable publication and benchmarked their work, culminating in comparable findings. As a result, the initial challenge of this research was to produce equivalent results using a computational model. Following the successful benchmarking, this computational model was further refined with the use of geometrical parameter variations. Similar computational model is used to produce a very high sensitive nanoscale antenna system for *RI* sensing applications after establishing complete confidence in it. However, while building a high-sensitivity nanoscale antenna system, it was discovered that traditional *FEM* software has a large computation complexity and takes a long time, maybe even a day, to generate useful conclusions.

As a result of this shortcoming in traditional *FEM* software, the second challenge comes into the frame. To address this limitation, Machine Learning (*ML*) was used to deal with the problem of predicting optical properties of the nano systems and comparing them to *FEM* outcomes to visualize the accuracy of the predictions. However, Machine learning neural network also need sufficient training dataset to make an accurate prediction. This problem still remains a big challenge for learning in the field nanotechnology. Hence to generate the dataset one needs specific optical domain knowledge to justify whether the accurate procedure was adopted during data generation. Although the performance of the *ML* neural network also depends on intrinsically design trade-off between the training data size and the prediction performance. In addition to increasing the training data size, another solution is generative methods. Due to the lack of monitoring data, learning agents are forced to make

Introduction

decisions based on incomplete information. Data curation turn out to be a potential solution to tackle such data size limitation problems when the agent is not omniscient.

In summary, *ML* neural network are applied extensively in nano structured sensing devices. Some of the challenges to be solved by *ML* are addressed here. Firstly, as aforementioned, *ML* is used to confirm the ubiquitous uncertainty during the nano structures fabrication. *ML* models are expected to learn from monitoring data and generate updated knowledge of the uncertain geometrical parameters. The prediction accuracy is the most common to assess the model performance with the help of Mean Squared Errors (*MSE*). This learning capability forms the foundation for neural network diagnosis and reliability. Secondly, *ML* can be useful in optimising the control plane decision-making process. This is commonly achieved by generating a utility (cost) function and optimising it with uncertainty. Thirdly, *ML* is a promising method for complementing traditional optimisation models, such as *FEM*, due to the high computational complexity. Although such applications sometimes sacrifice the learning accuracy, they can reduce the redundant computation and speed up the learning process, while maintaining acceptable levels of optimisation performance. Amongst all these challenges, the *ML* capability is critical for capturing the optical characteristics of any nano structured devices.

1.4 History and Literature

1.4.1 Nanostructures

Nanostructures and nanomaterials have rapidly received considerable attention from researchers due to their wide range of applications, and the worldwide market value of nanotechnology reached USD 90 billion by 2021 [1], as automotive and commercial applications of nanotechnology keep expanding [2]. Syngge introduced the theory of near-field region microscopy for the first time in 1928, but owing to several manufacturing limitations at that

time, no one acknowledged it. Bailey and Fletcher filed a patent for Electromagnetic Wave Converters in 1973, it marked as the first commencement of nanoscale antennas comparable which have been used nowadays [3]. Later, in 1985, Wessel published a concept for electric fields confinement caused by small nano metallic particles using Scanning Microscopy [4]. He also emphasised the significance of surface plasmon resonance in nanoparticles. Alvin M. Marks published a super submicron electron beam writer enabling immediate light energy is conversion into electric current in 1989 [5]. Subsequently, nano antenna gained its popularity among the researchers.

In recent days nano antenna still holds its popularity to carry out research. According to the literature there are a number of published articles shows the great effectiveness in regards of functionality. In 2004 Tolga Atay *et al.* have reported round periodical arrangements of gold antennas with significant resonance and wide field patterning [6]. Likewise another group of researchers designed asymmetric split ring resonators for organic substance detection [7]. Nano antenna can be used as a shared substrate for Surface Enhanced Raman Spectroscopy (SERS and SEIRS) respectively. In this way it can resonates in the visible and infrared region at the same time [8]. Additionally, Nano paired antenna used in different shapes as the Bow-Tie [9–12], Nanodisks [13–15], Nanorods [16–18, 11] and Nano elliptical shaped antenna have been reported [19, 20] in visible region. The preceding overview of the literature demonstrates the impressive outcomes of strong resonance and field confinement obtained through mathematical analysis and empirical research over the last few years. Some very well-known approaches, such as the finite element method [FEM], have been used to describe the numerical design and modelling of gold nano antennas [19, 20, 12, 21, 22, 9] and finite difference time domain method [FDTD] [23–27].

1.4.2 Nano materials

The four major types of nanomaterials are as follows: (I) Carbon nanomaterials, which include carbon compounds and comes in geometries such as tubular wires, elliptical, spherical, and cavities. Diamond, fullereness, carbon nano-fibers (CNTs), nano-tubes (C60, C80, and C240), and onion are some of the nanomaterials in this category. [28, 29]. Because of their extraordinary properties and unique carbon hybridization condition (e.g., sp^2 , sp^3 hybridization), nanomaterials have driven advancements in electronics, physics, optics, mechanics, biology and medicines since the 1990s [30]. Additionally, (II) Inorganic nanomaterials consist variety of nano metals and its alloys/oxides. In this category, several metals such as gold (Au), silver (Ag), and aluminium (Al) can be included, as well as TiO_2 and ZnO as oxides. (III) Organic nano-materials are primarily formed of organic components. The use of non-covalent (weak) interaction in molecular individual-assembly and layout aids in the transformation of organic NMs into desirable structures such as nanocarriers, nanocapsules, nanostructured lipid carriers, and polymeric nano materials [31]. Lastly (IV) Composites nanomaterials are primarily multi-phase nanostructures. It is also referred to as a hybrid composite since one phase of nanoparticles could either interact with another phase of the substance or blend with a broader bulk material. These are the most intricate structures since they are made up of organic metallic framework. Such nanomaterials are mostly composed of carbon atoms, ceramic, metals and other polymers/monomers with various morphology and functions. Here are a couple of good example: Floral rods of gold/zinc oxide (Au/ZnO) used for protein delivery identification, titanium dioxide/cerium oxide (TiO_2/CeO_2) nanowires seen as a relatively low cost, excellent-performance catalyst scheme, and a hybrid nanobelt of molybdenum trioxide-reduced graphene oxide (MoO_3 -rGO) used as a cathode material for lithium batteries [32–34]. Figure 1.2 depicts different classes of the nano materials.

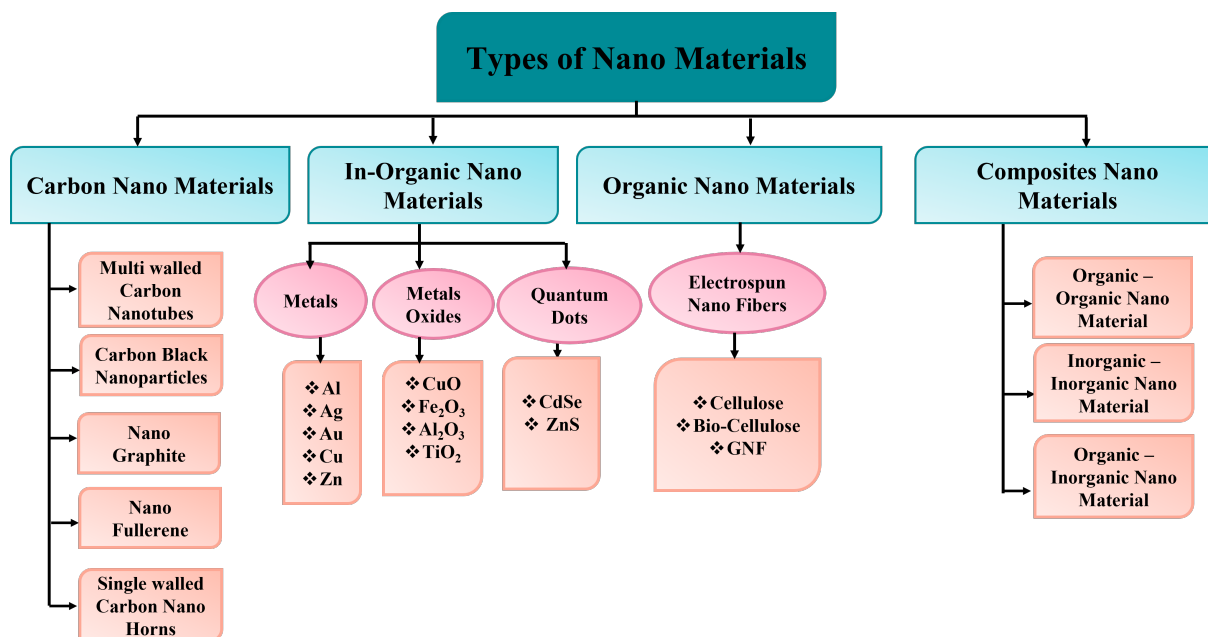


Fig. 1.2 Categorical analysis of Nano Materials [35].

When I emphasis on Einstein's conception of relativity theory, it's simple to observe that "physics is the synthesis of various physical and geometrical principles." This concept may indeed be repeated for nanotechnologies as follows: "Nanophysics is the discipline that comprises of the size/structure/surface and dimension of nano structures, as well as the fundamental elements of the physical laws inherent in substances." To gain a better understanding among the most frequent dimensions of nanostructures, I have classified them into four categories: 0D, 1D, 2D, and 3D nanostructures shown in Figure 1.3 [31].

Introduction

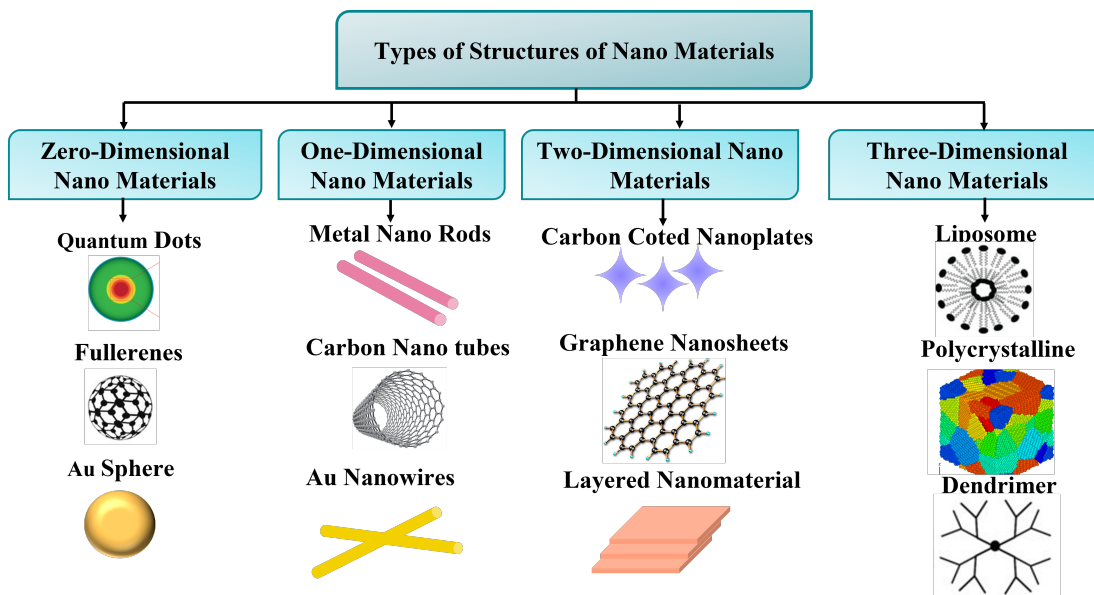


Fig. 1.3 Classification of structures Nano-materials [36].

Nano structures also have several distinct chemical and physical properties, including as a high specific surface area, strong electromechanical and optical conductance, and excellent chemical reactivity, which renders them attractive candidates for a wide range of applications. The brief description of the properties consisting in nano-structures shown in Figure 1.4.

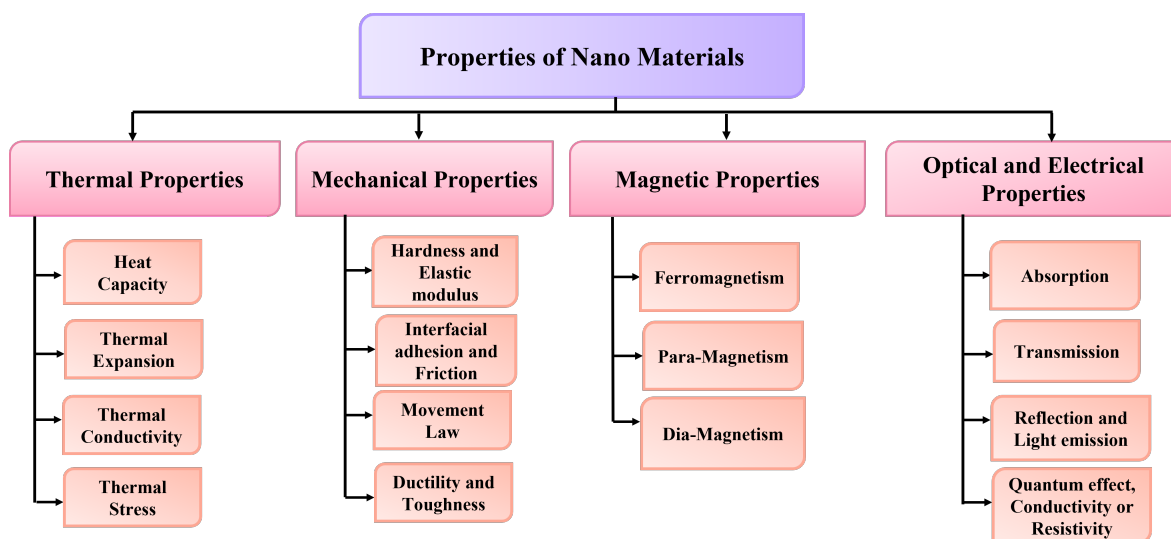


Fig. 1.4 Classification properties of Nano-Structures

1.4.3 Artificial Intelligence

Similarly, Artificial Intelligence (AI) has experienced substantial progress in the recent years and now being used by computer scientists and specialists, as well as other investigators in a range of sectors [37]. It has gained universal acceptance in dealing with complicated data-driven challenges in sciences and development, [38]. These models have an unequalled capacity to find and foresee data patterns, as well as uncover unexpected trends that a human observer may overlook [39]. It is particularly good at finding underlying data model and categorising exceedingly asymmetric data, making it appropriate for a wide variety of technical procedures. All scientists are working on light-matter interactions have advanced to a different extreme with the support of Machine Learning (*ML*), helped by materials engineering, mathematics, and optoelectronic innovations. This is demonstrated by following recent developments: The first one is the creation of intelligent optoelectronic systems, while the second is the incorporation of *ML* into physical and chemical sciences enabling in-depth active learning and innovative basic insights [40].

Eventually, optoelectronics equipment advanced its usefulness by allowing *ML* approaches, outperforming conventional optical sensors, which was inefficient in terms of time and resources, and offered restricted functionality. As a result, numerous investigators had also turned their attention to *ML* being used in a wide range of application domains such as comprehensible optical interaction systems [41], plasmonics [42, 43], fibre channels [10, 44], sensors [45–49], photonic crystal fibres [50] and nanotechnology [51–55]. Nanophotonics with *ML* is a prime instance of fast predictions of electro-optic resonant frequencies and strong localised field, which may be adjusted for diverse purposes by modifying the shape and materials choices of the nanostructures. Feed forward convolutional neurological systems have the capability to solve complicated challenges in nano-optics as well.

1.5 Outlines

This dissertation is divided into eight chapters, including the present introductory chapter. The following is a synopsis of the chapter's contents:

Chapter 2 presents the review of analytical and numerical methods used in the literature for design, optimisation, and performance analyses of gold nano antenna. These numerical methods generally use Maxwell's equations (in differential or integral form) when solving the computational domain for electromagnetic wave propagation. It has been identified that the mesh size plays a crucial role in improving the accuracy of the numerical methods. A trade-off is required as decreasing the mesh element size might significantly increase the computation time and resources. It also describes the numerical method for designing the nano structures and the effect of all the parameters such as substrate height, geometries of the antenna and surrounding medium. A detailed study has been carried out to obtain the transmission/reflection and absorption spectra, optical mode profiles, power confinements, and optical power density. I have also considered to design a replica of the paired nano antenna to get a confidence on the designed model and tried to measure all the given parameters. Regular and irregular mesh arrangements were considered and compared in terms of accuracy and dip ratio. Irregular meshes can use dense mesh inside the core, while coarse mesh can be used outside the core to further reduce the computational times in comparison to when using a regular mesh arrangement.

Chapter 3 The modelling approaches used to evaluate the optical behaviour of the array surface are described in depth in this chapter. The nano particle and the substrate interaction plasmonically have been discussed. This chapter also delves over the sensing mechanism with finite element method (*FEM*) modelling and the evolution of the computational model employed in the study.

Chapter 4 In this chapter, I discuss the use of gold nano antennas in a number of healthcare applications owing to their appealing electrical and optical characteristics that vary depending on size and shape. Due to their strong electromagnetic field confinement and diffraction limit, a periodical coupled gold nano structure exploiting surface plasmon resonance is described herein, which displays impressive outcomes for index of refraction (RI) detection. Solitary and coupled gold nano-structured sensors have been used in this research for real-time RI monitoring. Full-Width Half-Maximum (*FWHM*) and Figure-of-Merit (*FOM*) are also computed, which associate sensitivities with the sharpness of the peak. The influence of multiple geometric structural sizes and designs is researched to enhance the sensitivity response of nano sensing-structures and identifies an optimised elliptical nano antenna with major axis a , minor axis b , gap between the pair g , and heights h of 100 nm, 10 nm, 10 nm, and 40 nm, respectively. Therefore in this chapter, I explored the bulk sensitivity, which is the spectrum displacement each refractive indices unit caused by fluctuations in the neighbouring medium, and this value was estimated as 526-530 nm/RIU, as well as the *FWHM* was obtained approximately 110 nm with a Figure-of-Merit (*FOM*) of 8.1.

Chapter 5 Artificial Neural Network (*ANN*) has recently emerged as a promising method for analysing a complicated statistics challenge in Machine Learning (ML). It has gained popularity in several fields of science, including mathematics, optoelectronics, and mechatronics, because to its own time-efficient breakthroughs. This chapter discusses a novel way to designing and optimising electromagnetic plasmonic nanoparticles relying on an *ANN* based computationally inexpensive technique. The nano particles in this work were designed through using the Finite Element Method (*FEM*), and afterwards Artificial Intelligence (*AI*) has been used to predict associated sensitivity (S), Full Width Half Maximum (*FWHM*), Figure of Merit (*FOM*), and Surface plasmon resonance wavelength (PW) for various paired nanostructures. At the start, the computational model is created by preparing the dataset using the Finite Element Method (*FEM*). To create the dataset, the input variables were the

Introduction

Major axis, a , the Minor axis, b , and the separation gap, g , and these were used to determine the associated sensitivity (nm/RIU), $FWHM$ (nm), FOM , and plasmonic wavelength (nm). Second, the neural network was created in such a way that the number of hidden layers and neurons were improved as part of a complete evaluation to increase the ML model's performance. This method was then used to produce predictions for certain inputs and their related outcomes after successfully optimising the computational model. This chapter also examines the difference between anticipated and simulated results. For estimating outputs for multiple input device settings, this methodology outperforms conventional computational approaches.

Chapter 6 In this chapter, I have presented nanophotonics which is the science of photonics and nanotechnology that has transformed optics in recent years by allowing subwavelength structures to enhance light-matter interactions. Despite these breakthroughs, design, fabrication, and characterization have remained iterative processes that are often computationally costly, memory-intensive, and time-consuming. In contrast, deep learning (DL) approaches have recently shown excellent performance as practical computational tools, providing an alternate avenue for speeding up nanophotonics simulations. This study presents a DL framework for transmission, reflection, and absorption spectra predictions by grasping the hidden correlation between the independent nanostructure properties and their corresponding optical responses. The proposed DL framework is shown to require a sufficient amount of training data to achieve an accurate approximation of the optical performance derived from computational models. The fully trained framework can outperform a traditional EM solution based on the COMSOL Multiphysics approach by 1000 times. Furthermore, employing deep learning methodologies, the proposed DL framework makes an effort to optimise design elements that influence the geometrical dimensions of the nanostructure, offering insight into the universal transmission, reflection, and absorption spectra predictions at the nanoscale. This paradigm improves the viability of complicated nanostructure design

and analysis, and it has a lot of potential applications involving exotic light-matter interactions between nanostructures and electromagnetic fields. In terms of computational times, the designed algorithm is around 700 times faster as compare to conventional *FEM* method. Hence, this approach paves the way for fast yet universal methods for the characterization and analysis of the optical response of nanophotonic systems.

Chapter 7 Photonic researchers have increasingly exploiting nanotechnology due to the advent of numerous prevalent nanosized manufacturing technology, which has enabled novel shaped nanostructures to be manufactured and investigated as a method of exploiting these nano-structures. Owing to the variety of optical modes, hybrid nanostructures that integrate dielectric resonators with plasmonic nanostructures are also offering enormous potentials. In this work, I have explored a hybrid coupled nano-structured antenna with stacked multilayer Lithium Tantalate ($LiTaO_3$) and Aluminum Oxide (Al_2O_3) operating at visible and infrared ranging from 400 nm–2000 nm. Here, the sensitivity response has been explored of these hybrid nano-structured array made of gold elliptical disk placed on the top of the quartz substrate and excite different modes in both the materials. It shows a large electromagnetic confinement in the separation gap (g) of the dimers due to strong surface plasmon resonance (SPR). The influences of the structural dimensions are investigated to optimize the sensitivity of the stacked elliptical dimers. The designed hybrid coupled nano-structure with the combination 10 layers of gold (Au) and Lithium Tantalate ($LiTaO_3$) or Aluminum Oxide (Al_2O_3) with (5 layers each) $h_1 = h_2 = 10$ nm exhibits high bulk sensitivity (S). The bulk sensitivity, which is the spectrum shift per unit refractive index (RI) change in the surrounding medium, was calculated to be 730 and 660 nm/RIU for and Lithium tantalate ($LiTaO_3$) /Aluminum oxide (Al_2O_3), respectively when the major axis, (a) = 100 nm, minor axis, (b) = 10 nm, separation gap (g) = 10 nm, and height, (h) = 100 nm. The sensitivity of the proposed hybrid nano-structure has been compared with a single metallic (only gold) elliptical paired nano-structure to demonstrate a significant improvement in the sensitivity using a

Introduction

hybrid nano-structure. Depending on these findings, I have demonstrated a roughly two-fold increase in sensitivity (S) can be obtained by utilizing a hybrid nano linked nano-structure compared to identical nano structure, which competes with traditional sensors with the same height, (h) based on localized surface plasmon resonances. Our innovative novel plasmonic hybrid nanostructures provide a framework for developing plasmonic nanostructures for use in various sensing applications.

This dissertation concludes with **Chapter 8** which summarises all the findings and explores possible directions of future work.

Chapter 2

Overview of Numerical Methods of Electromagnetics field theory

2.1 Maxwell's Equations

Maxwell's equations play an important role to describe the propagation of EM waves in any kind of electromagnetic systems, such as waveguides or antenna systems. The concept of these equations were presented by Lord James Clerk Maxwell, which are completely based on the classical electromagnetic field theory. From these equation one can calculate the relations between electric and magnetic fields which are generated by charges, flow of electrons, and changes of the fields propagating in any kind of medium. These set of four partial differential equations can be presented in both differential and integral forms.

2.1.1 Differential Form

Differential form of Maxwell's equations are used for calculating the time and space dependent relationships of electromagnetic field and also useful for solving any kind of analytical and numerical problems for complicated structures. These equations are also used in any

Overview of Numerical Methods of Electromagnetics field theory

modelling as Finite Element Method (COMSOL Multiphysics) and Finite Difference Time Dome (FDTD) analysis [56].

The differential form of Maxwell's equations for the time varying electromagnetic fields is more widely used, and is defined as follows:

$$\nabla \cdot \mathbf{D} = \rho \quad (2.1)$$

$$\nabla \cdot \mathbf{B} = 0 \quad (2.2)$$

$$\nabla \times \mathbf{E} = -\frac{\partial \mathbf{B}}{\partial t} \quad (2.3)$$

$$\nabla \times \mathbf{H} = \mathbf{J} + \frac{\partial \mathbf{D}}{\partial t} \quad (2.4)$$

where, \mathbf{E} is the vector electric field, \mathbf{H} is the vector magnetic field, \mathbf{D} is the vector electric flux, \mathbf{B} is the vector magnetic flux, \mathbf{J} is the vector form of current density of the medium and ρ is the charge density of the medium.

2.1.2 Integral Form

The integral form of Maxwell's equations has been used to describe the underlying physical laws. This form of the equations are required to establish the calculations for boundary conditions, and also used to describe the electromagnetic fields having a higher degree of symmetry. These equations can be easily derived from the differential form by applying Stokes theorem [57]. They can also be used in some finite difference algorithms [58, 59] and finite integration methods [60]. The integral form of Maxwell's equations are given as follows:

$$\oint_S \mathbf{D} \cdot d\mathbf{S} = Q_{enclosed} \quad (2.5)$$

$$\oint_S \mathbf{B} \cdot d\mathbf{S} = 0 \quad (2.6)$$

$$\oint \mathbf{E} \cdot d\mathbf{l} = -\frac{\partial}{\partial t} \int_S \mathbf{B} \cdot d\mathbf{S} \quad (2.7)$$

$$\oint \mathbf{H} \cdot d\mathbf{l} = \oint_S \mathbf{J} \cdot d\mathbf{S} + \frac{\partial}{\partial t} \int_S \mathbf{D} \cdot d\mathbf{S} \quad (2.8)$$

where $d\mathbf{S}$, $d\mathbf{l}$ are the vectors denoting the change in the surface \mathbf{S} and change on the line \mathbf{l} , respectively. The quantities involved in Equations 2.1–2.8 and their respective units are listed below:

Table 2.1 Electromagnetic quantities and units

Quantity	Description	Units
E	Electric field amplitude	<i>Volt/meter</i> (V/m)
H	Magnetic field amplitude	<i>Amp/meter</i> (A/m)
D	Electric flux density	<i>Coulomb/meter²</i> (C/m ²)
B	Magnetic flux density	<i>Weber/meter²</i> (Wb/m ²)
J	Current density	<i>Amp/meter²</i> (A/m ²)
ρ	Charge density	<i>Coulomb/meter³</i> (C/m ³)
Q	Charge	<i>Coulomb</i> (C)

2.1.3 Constitutive Relations

The electric and magnetic flux densities (**D** and **B**) are related to the electric and magnetic field amplitudes (**E** and **H**) by the constitutive relations. The functional form of the relationship

Overview of Numerical Methods of Electromagnetics field theory

depends upon the nature of the medium. For linear and isotropic media, the relations between electric flux, magnetic flux, electric field and magnetic field are given by:

$$\mathbf{B} = \mu \mathbf{H} \quad (2.9)$$

$$\mathbf{D} = \epsilon \mathbf{E} \quad (2.10)$$

where μ is the magnetic permeability of the medium (in Henry/meter) and ϵ is the electrical permittivity of the medium (in Farad/meter). The values of μ and ϵ in vacuum are symbolically denoted by μ_0 and ϵ_0 , respectively and are given as:

$$\mu_0 = 4\pi \times 10^{-7} \quad \text{Henry/m}$$

$$\epsilon_0 = 8.854 \times 10^{-12} \quad \text{Farad/m}$$

2.1.4 The Wave Equations

The electromagnetic wave equation can be derived using Maxwell's equations. For a source free ($\rho = 0, J = 0$), linear (μ and ϵ are independent of \mathbf{E} and \mathbf{H}), and isotropic medium conditions, Equations 2.1–2.4 become:

$$\nabla \cdot \mathbf{D} = \rho \quad (2.11)$$

$$\nabla \cdot \mathbf{B} = 0 \quad (2.12)$$

$$\nabla \times \mathbf{E} = -\frac{\partial \mathbf{B}}{\partial t} \quad (2.13)$$

$$\nabla \times \mathbf{H} = \frac{\partial \mathbf{D}}{\partial t} \quad (2.14)$$

Where, \mathbf{E} is the vector electric field, \mathbf{H} is the vector magnetic field, \mathbf{D} is the vector electric flux, \mathbf{B} is the vector magnetic flux, and ρ is the charge density of the medium.

Equations 2.11–2.14 are strongly coupled first-order differential equations and it is not easy to implement these equations in a computer program for the solution of many problems. Therefore, it is usual practice for many algorithms to use decoupled second-order differential equations that consist of only one field value (either \mathbf{E} or \mathbf{H}). It should be noted that the choice of a coordinate system is critical in obtaining the wave equation

The wave equation in terms of the electric field amplitude is given by [57]:

$$\nabla^2 E - \mu\epsilon \frac{\partial^2 \mathbf{E}}{\partial t^2} = 0 \quad (2.15)$$

While, the wave equation in terms of the magnetic field amplitude is given by [57]:

$$\nabla^2 H - \mu\epsilon \frac{\partial^2 \mathbf{H}}{\partial t^2} = 0 \quad (2.16)$$

As both wave equations consist of only one field amplitude, discretisation of the computational domain for different numerical methods becomes easier in comparison to when using the coupled equations [61]

2.2 Numerical Calculations: Finite Element Method

The Finite Element Method (FEM) is a quantitative approach for addressing a wide range of engineering problems, includes computational electromagnetics, and is especially beneficial for difficulties with variable shapes and steep gradients. The FEM was initially introduced for the modelling of mechanical applications related to aerospace and civil engineering structures. Later on, it was employed in different areas of interest including structural analysis, heat transfer, fluid flow, biomechanics, biomedical, and electromagnetics, among others.

The main feature of FEM is to break the spatial domain (one-, two- or three-dimensional) into a number of simple geometric elements such as triangles or quadrilaterals called element. These elements are assumed to be connected with one another, but only at interconnected joints, known as nodes. The complete arrangement of the elements is known as a mesh. The FEM formulation of the problem results in a system of algebraic equations. Each element represents a set of equations. All sets of element equations are then systematically recombined into a global system of equations that models the entire problem. FEM theory is well developed and offers great freedom in the selection of discretisation. The precision of this procedure is also influenced by the mesh size. A finer mesh throughout the entire region potentially prove more effective, but at the expense of additional processing complexity. In order to reduce this computation time different element sizes for the discretisation can also be considered. In the region where the field fluctuates rapidly, a finer mesh might well be employed. A coarser mesh, on the other hand, can be employed if there is minimal fluctuation or magnetic vibrations are nearly insignificant.

2.3 Surface Plasmon Resonance

In 1902, Wood explained the concept of Surface Plasmon Resonance (*SPR*) [62]. As I have already discuss Maxwell's Equations for electromagnetics, hence it would be easy to understand the concept of Plasmons. When polarized incident wave launched in any medium it consists both electric and magnetic vectors and I can solve the coupled equation with the help of Maxwell's Equations. The free electrons which got excited due to *EM* waves are known as Polaritons and if these free electrons are bounded at the surface of any structures then it is known as Surface Polaritons but if these free electrons in any metal react with polarized light then it is known as surface plasmon resonance (*SPR*). There are some restriction in surface plasmon resonance that they can only occur in the metals due to its negative dielectric constant, at high plasmon frequencies and large amount of electrical conductivity, hence can shown prominent results of Surface Plasmons.

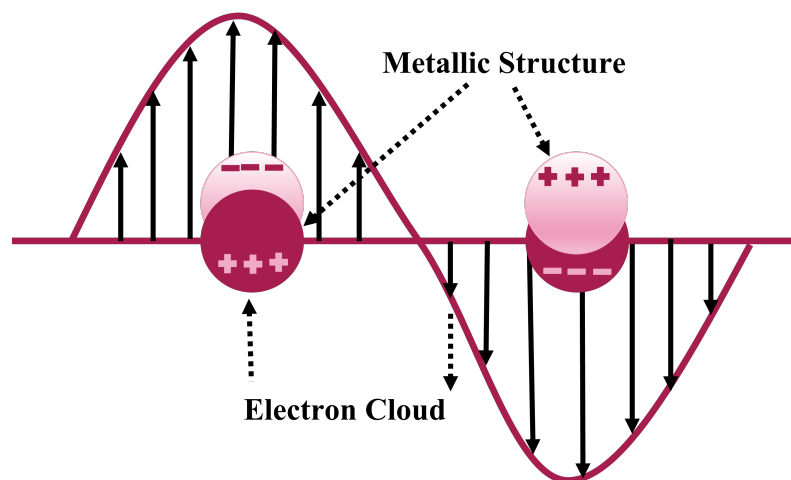


Fig. 2.1 Schematic of Interaction of electric field with gold nanospheres resulting in electron cloud oscillation.

Figure 2.1 shows the *SPR* is associated to charge densities oscillations at the interface at metallic layer because it depends on the optical characteristics of the metal nano structure and environmental variations. As a consequence, biomolecular are extremely sensitive to

Overview of Numerical Methods of Electromagnetics field theory

plasmon resonance, obviating the need for exogenous biomolecular labelling. *SPR* has the benefit that it does not pass the light beam through the surrounding medium, therefore the impact of light absorption in the analyte may be neglected. As a result, the principal use of *SPR* is to characterise the surrounding medium. In other words, the resonance conditions has been formed when the frequencies of the photons satisfies the natural frequency of metal electron oscillations against the force applied of positive nuclei, supplied the metals does indeed have a large negative real part and very small positive imaginary part of the dielectric constant. Surface plasmons are classified into two categories in the nanometer scale: localised and propagating plasmons. The aggregate synchronized electromagnetic oscillation is restricted at the subatomic particle surface in the first example, forming an electromagnetic field surrounding it that is referred as localised surface plasmon resonance (*LSPR*). Surface charge oscillations naturally interface with electromagnetic waves or incoming photons in the second scenario, propagating along the metal dielectric intersection can be defined as Surface plasmon polariton (*SPP*). This is restricted to a two-dimensional environment because *SPP* does not couple to EM illumination at the flat metal and vacuum interface, gratings or prismatic matching techniques are used to create energy coupling. However, *SPP* propagation is hampered by damping, which becomes a major issue when it is used in sensors, nano circuits, and plasmonic lasers. *LSPR* and *SPP* are depicted schematically in Figure 2.1. For the physical world, both *SPR* and *LSPR* have distinct features. Electromagnetic waves propagate in a transverse direction is known as Surface plasmon waves (*SPW*). The *SPWs* might be either radiative or nonradiative. With planar electromagnetic waves, coupling occurs, resulting in visual phenomena such as transitional radiation and plasma resonance absorption. The frequency of *LSPR* varies depending on the material type (platinum, gold, silver, etc.) and is greatly influenced by the form, shape, and thickness of nanostructures as well as their nearby environment. These days researchers are giving more importance to gold and silver due to its ease in fabrication and good affect in resonance. Some metals

like aluminium can also use for surface plasmons but it suffers from low durability and oxidization, hence it has never achieved that much popularity. The minor changes in the surrounding dielectric environment, such as molecular adsorptions on the surface of the nanoparticle, impact the frequencies of *LSPR*, which may be seen as light scattering and absorption frequency shifts. These shifts then be readily converted into simple optical transmission or reflection observations with great spectrum precision, allowing nano-sized *LSPRs* to be used as excellent sensors for chemical and biological analytes detection.

2.3.1 Mathematical Description of Surface Plasmon Polaritons

The simplest geometry for sustaining Surface Plasmon Polaritons, a planar metal-dielectric interface which is semi-infinite in the x - z plane. The metal has a frequency-dependent, complex dielectric function, $\epsilon_m(\omega)$ and the dielectric has a real, positive dielectric constant, ϵ_d as shown in Figure 2.2.

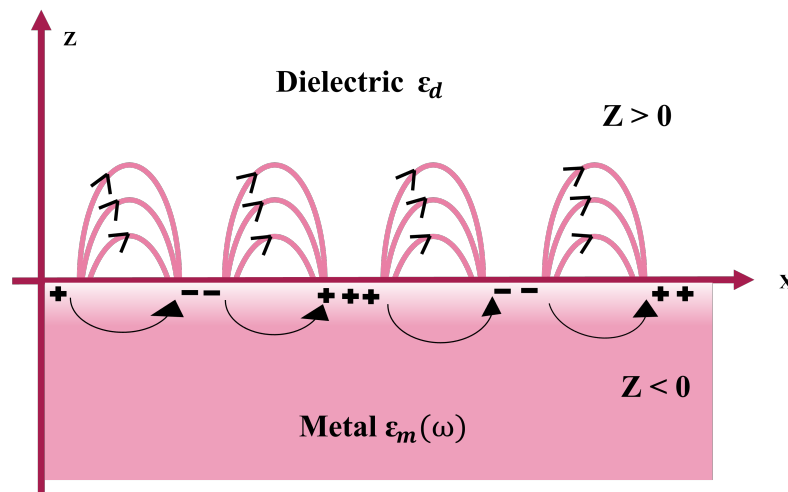


Fig. 2.2 Schematic of Dielectric (ϵ_d) and Metal ($\epsilon_m(\omega)$) Semi-Infinite Interface Supporting SPP Propagation.

The *SPPs* will propagate along the boundary ($z=0$) in the x direction, with an infinite y plane preventing scattering effects from the edges of the media. If the *SPPs* travel in the z -direction, they experience exponential decay with distance into either media. Therefore,

Overview of Numerical Methods of Electromagnetics field theory

the SPPs must have a wavevector, k with real part in x -direction and imaginary component in z -direction. In addition, as the *SPPs* propagate along the interface then field components must be continuous across the boundary. It can be shown that for these conditions, no surface modes exist for transverse electric (*TE*) polarisation [63] and only transverse magnetic (*TM*) polarisation will excite *SPPs*.

Transverse magnetic waves have perpendicular magnetic field and parallel electric field components, H_y , E_x and E_z respectively. The electric and magnetic fields of the *TM* wave can then be described in the metal ($z < 0$) by equations 2.17–2.18 respectively and dielectric ($z > 0$) by equations 2.19–2.20 respectively.

For Metal when $z < 0$:

$$\mathbf{E}_m = (\mathbf{E}_{mx}, 0, \mathbf{E}_{mz})e^{i(\mathbf{k}_x x - \mathbf{k}_{mz} z - \omega t)} \quad (2.17)$$

$$\mathbf{H}_m = (0, \mathbf{H}_{my}, 0)e^{i(\mathbf{k}_x x - \mathbf{k}_{mz} z - \omega t)} \quad (2.18)$$

For Dielectric when $z > 0$:

$$\mathbf{E}_d = (\mathbf{E}_{dx}, 0, \mathbf{E}_{dz})e^{i(\mathbf{k}_x x - \mathbf{k}_{dz} z - \omega t)} \quad (2.19)$$

$$\mathbf{H}_d = (0, \mathbf{H}_{dy}, 0)e^{i(\mathbf{k}_x x - \mathbf{k}_{dz} z - \omega t)} \quad (2.20)$$

By applying Maxwell's Equations in absence of charges and currents, and suitable boundary conditions to equations 2.17–2.18 and 2.19–2.20, the surface plasmon dispersion relation can be derived [64] and is given in 2.21.

$$\mathbf{k}_x = \mathbf{k}_{spp} = \mathbf{k}_0 \sqrt{\frac{\epsilon_d \epsilon_m(\omega)}{\epsilon_d + \epsilon_m(\omega)}} \quad (2.21)$$

Where $\epsilon_m(\omega)$ shows the dependence of the metal dielectric function (and behaviour) on the optical frequency. For surface plasmon polaritons (*SPPs*) to exist, the real part of the dielectric function must be negative in the metal will be concluded in next section, and its magnitude must be greater than that of the dielectric. Figure. 2.3 below compares the dispersion relation of *SPPs* with that of incident light in air.

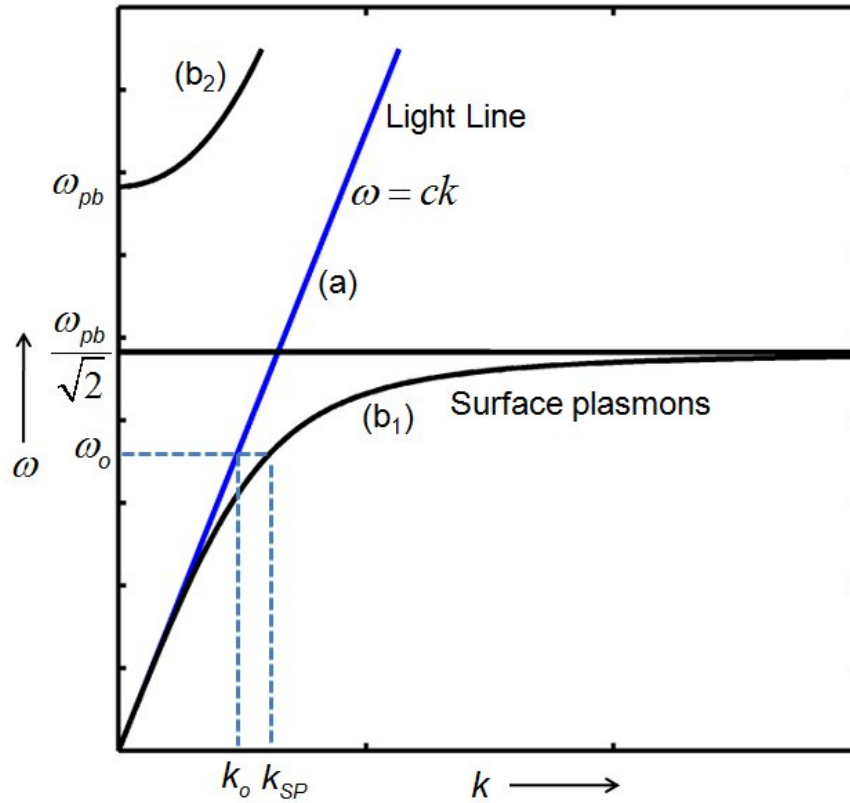


Fig. 2.3 Comparison of Dispersion Curves for Surface Plasmon Polaritons (SPP) (black line) and Incident Light (blue line) Showing Wavevector Mismatch.

At large wavevectors, the *SPPs* approach the surface plasmon frequency, as given by equation 2.22.

$$\omega_{SP} = \frac{\omega_p}{\sqrt{1 + \epsilon_d}} \quad (2.22)$$

If damping of the free electron oscillations is considered negligible, then as the frequency tends toward the surface plasmon frequency, the wavevector tends towards infinity and gradient (group velocity, $d\omega/dk$) tends to zero. In this case, the mode is electrostatic and represents a surface plasmon. Hence the surface plasmon frequency is an asymptotic limit for the *SPPs*. The dispersion relations of light and *SPPs* never overlap, which visually represents the wavevector momentum mismatch between the two. This means that incident light cannot directly excite the *SPPs* and a coupling method is required to overcome this mismatch.

2.4 Drude Free Electron Theory

Sir Paul Drude, in 1900, discussed the behaviour of free electrons in any kind of metal. This model can be used to find the optical and structural properties of any metallic structure. This approach concentrates on the free electrons that reside in metal and produce surface plasmons; therefore, I could simply compute the surface plasmon resonance using transmission/reflection and absorption spectra using this framework. This can also show the good results on insulators with any kind of doping which consist free electrons.

The function calculated by Drude theory is shown below:

$$\epsilon_r = \epsilon_\infty - \frac{\omega_p^2}{\omega(\omega + j\gamma)} \quad (2.23)$$

Where ϵ_r is considered as Drude constant, ϵ_∞ is the permittivity of the metal, ω_p is known as plasmon frequency which is defined as the natural frequency of undamped oscillations of the free electrons i.e. $\sqrt{\frac{4\pi N e^2}{m_0}}$, where N and m_0 is considered as conduction electron density

2.4 Drude Free Electron Theory

and effective optical-mass respectively. γ is the free electron plasma oscillations that occurs due to damping through electron collisions with collision frequency is shows as $\gamma = \frac{1}{\tau}$. Where τ is the relaxation time and, which is typically around 10^{-14} sec. Approximating the metal as a driven, damped oscillator, the dielectric function can be described as a combination of phase lag between the driving frequency and natural frequency of the free electrons and the loss of energy through damping. By considering these factors, the dielectric function can be rewritten as complex with real and imaginary parts as given in equations 2.24–2.25.

$$\epsilon_{real} = 1 - \frac{\omega_p^2 \tau^2}{1 + \omega^2 \tau^2} \quad (2.24)$$

$$\epsilon_{imag} = \frac{\omega_p^2 \tau}{\omega(1 + \omega^2 \tau^2)} \quad (2.25)$$

For metallic structure at near-infrared frequencies are considered when $\omega \gg 1/\tau$, Equations (2.24 and 2.25) simplify to [65].

$$\epsilon(\omega) = 1 - \frac{\omega_p^2}{\omega^2} + j \frac{\omega_p^2}{\omega^3 \tau} = \epsilon_{real}^f + j \epsilon_{imag}^f \quad (2.26)$$

The real part relates to the phase lag, which is due to the slowing down of an incident electromagnetic wave through the metal, dependent on the metal's permittivity to the light. At angular frequencies less than the plasma frequency, the real dielectric function of metals will be negative. The imaginary part is due to damping of the wave within the metal, through losses from resistance and absorption of the incident light. The complex dielectric function can be rewritten in terms of its real and imaginary counterparts as shown in equation 2.26. Figure 2.4 depicts the computed real and imaginary components of the dielectric permittivity for gold, which have been used to computed the reflection and transmission coefficients.

Overview of Numerical Methods of Electromagnetics field theory

Equation 2.24 shows that the real dielectric function with the optical frequencies. This value becomes smaller through the ultraviolet regime, before turning negative in the visible region and is largely negative in the infrared spectrum. This optical property of the real dielectric function gives rise to the various optical behaviour of metals, including the existence of plasmons. Plasmons are the oscillations of the free electrons within the plasma. Plasmons can exist in bulk or at a metal-dielectric boundary, where they are referred to as a surface plasmon. To support plasmons, the real dielectric function of the metal must be negative in the specified wavelength range and the imaginary part, which determines absorption, must be small to prevent lossy waves.

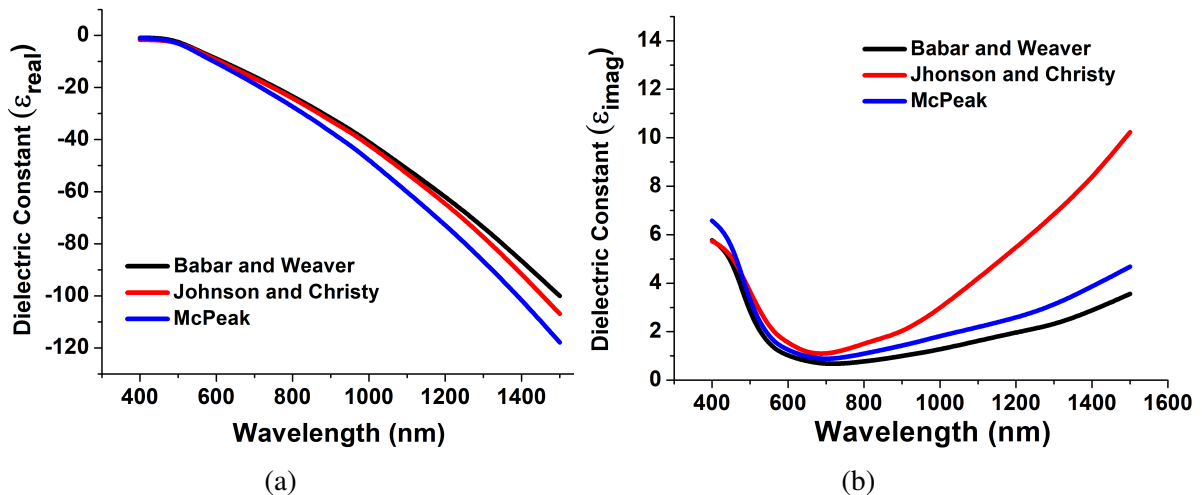


Fig. 2.4 Real (a) and Imaginary (b) counterparts of dielectric constant of gold obtained from [65].

Here, in the Figure 2.4 data-sets have been collected data from the Babar and Weaver [65], Jhonson and Christy [65] and McPeak [65] for achieving the accurate and strong resonance. Furthermore, I have implemented the model in Comsol Multiphysics by importing these data sets.

2.5 LSPR on Nanospheres

The optical properties of colloidal gold particles have been utilized throughout history, from use in paints and in the famous Lycurgus cup [66]. In 1908, Gustav Mie published his research in describing the underlying mechanisms producing these properties [67]. It describes the interactions between electromagnetic fields and colloidal gold nanoparticles, considering them as homogeneous metal spheres of arbitrary size surrounded by an isotropic, non-absorbing dielectric media. That work focused on the nanostructures smaller than the wavelength of incident light, where nanosphere interactions can be analysed through use of the quasi-static approximation.

The approximation assumes that the nanosphere experiences a surrounding uniform external electric field and Maxwell's equations can then be solved for this quasiparticle field. A complete derivation of the approximation which solves the Laplace equation under suitable boundary conditions can be found elsewhere [63, 68]. The treatment concludes that the applied field induces a dipole moment, \mathbf{p} at the centre of the nanosphere, given by equation 2.27.

$$\mathbf{p} = 4\pi\epsilon_0\epsilon_d r^3 E_0 \frac{\epsilon_m - \epsilon_d}{\epsilon_m + 2\epsilon_d} \quad (2.27)$$

Where \mathbf{E}_0 is the applied field, r is the nanosphere radius and ϵ_m and ϵ_d are the dielectric function of the metal and dielectric constant of the surrounding media, respectively. The polarisation of the nanoparticle is in the same direction as the applied field, with strength proportional to the field as shown in equation 2.28.

$$\mathbf{p} = \epsilon_0\epsilon_d \alpha \mathbf{E}_0 \quad (2.28)$$

Overview of Numerical Methods of Electromagnetics field theory

Where the polarizability of the nanosphere, α is given by equation 2.29.

$$\alpha = 4\pi r^3 \left(\frac{\epsilon_m(\omega) - \epsilon_d}{\epsilon_m(\omega) + 2\epsilon_d} \right) \quad (2.29)$$

The polarisability occurs due to the external field, which induces a dipole moment proportional to the field. Equation 2.28 shows that the response of the charge distribution to external perturbations is dependent on the nanoparticle shape, material and surrounding media. As the dielectric function of the metal is frequency dependent, therefore the polarizability is also frequency dependent. When the denominator approaches a minimum, the polarizability shows a resonant enhancement. Light scattering off the nanosphere and absorbed by the nanosphere also experiences a resonance enhancement which can be expressed through scattering and absorption cross-sections. The cross sections can be derived from the Poynting vector of the electromagnetic fields from the nanosphere, treated as an oscillating dipole [63]. The scattering and absorption cross-sections are given in equations 2.30 and 2.31, respectively.

$$C_{sca} = \frac{\mathbf{k}_0^4}{6\pi} |\alpha|^2 = \frac{8\pi}{3} k_0^4 r^6 \left[\frac{\epsilon_m - \epsilon_d}{\epsilon_m + 2\epsilon_d} \right]^2 \quad (2.30)$$

$$C_{abs} = \mathbf{k}_0 \text{Im}|\alpha| = 4\pi k_0 r^3 \text{Im} \left[\frac{\epsilon_m - \epsilon_d}{\epsilon_m + 2\epsilon_d} \right] \quad (2.31)$$

Where \mathbf{k}_0 is the wavevector given by the angular frequency, ω over speed of light, c . The sum of these two cross-sections gives the resonant enhanced extinction cross-section, given by equation 2.32.

$$\mathbf{C}_{ext} = \mathbf{C}_{sca} + \mathbf{C}_{abs} = 9 \frac{\omega}{c} \epsilon_d^{\frac{3}{2}} V \left(\frac{\epsilon_i}{(\epsilon_{real} + 2\epsilon_d)^2 + \epsilon_{imag}^2} \right) \quad (2.32)$$

Where V is the volume of the nanosphere and ϵ_{real} and ϵ_{imag} are the real and imaginary portions of the metal sphere's dielectric permittivity (equation 2.26). Plotting extinction data shows a peak at a specific frequency, corresponding to the *LSP* mode and is given by equation 2.33, assuming the metal follows the Drude model.

$$\omega_{LSP} = \frac{\omega_p}{\sqrt{\epsilon_d + 2}} \quad (2.33)$$

2.6 COMSOL Model Methodology and Validation

This section reviews the popular modelling techniques for plasmonic systems, including theoretical, analytical and numerical methods. The development of the model used in this research is discussed, showing the progression from isolated nanoparticle models to the final nano elliptical antenna array surface. In addition, the effect of approximations and restrictions of the system are also considered. The validity of the final model is also examined, through comparison of simulated data to other model outputs.

2.6.1 Mie Theory

Mie theory, as detailed in Section 2.5, provides a mechanism of determining the absorption and scattering behaviour of spherical nanoparticles in an isotropic and homogeneous environment [67, 69]. Expansions of the theory have also been carried out to provide approximate solutions for other simple geometries such as infinite cylinders and ellipsoids [70, 71]. In this work, the theoretical Mie scattering from nanospheres was determined using MiePlot

Overview of Numerical Methods of Electromagnetics field theory

v4.6 software [72]. The program utilises the BHMIE algorithm [73] to determine the Mie scattering profile. Scattering from ellipsoids was also calculated using the Mie-Gans approximation outlined in Chapter 4. The main limitation of Mie theory-based models is the inability to accurately model the resonant behaviour of many fabricated structures, including elliptical nano antennas, nanorods, holes and domes. In addition, Mie theory calculations do not consider the density of the nanostructures and can only model isolated structures in homogeneous media. However, as Mie theory can accurately determine the optical behaviour of simple specific systems, it was used at the start as a validation method for the models utilised in this research shown in Section 2.6.2.

2.6.2 Gold nano sphere in air/water

In this section, I have optimized the performance of standalone gold nano sphere and benchmarked it with the available Mie theory [74] and calculated the absorption, extinction and scattering efficiency at different radius of sphere when the surrounding medium was air.

2.6 COMSOL Model Methodology and Validation

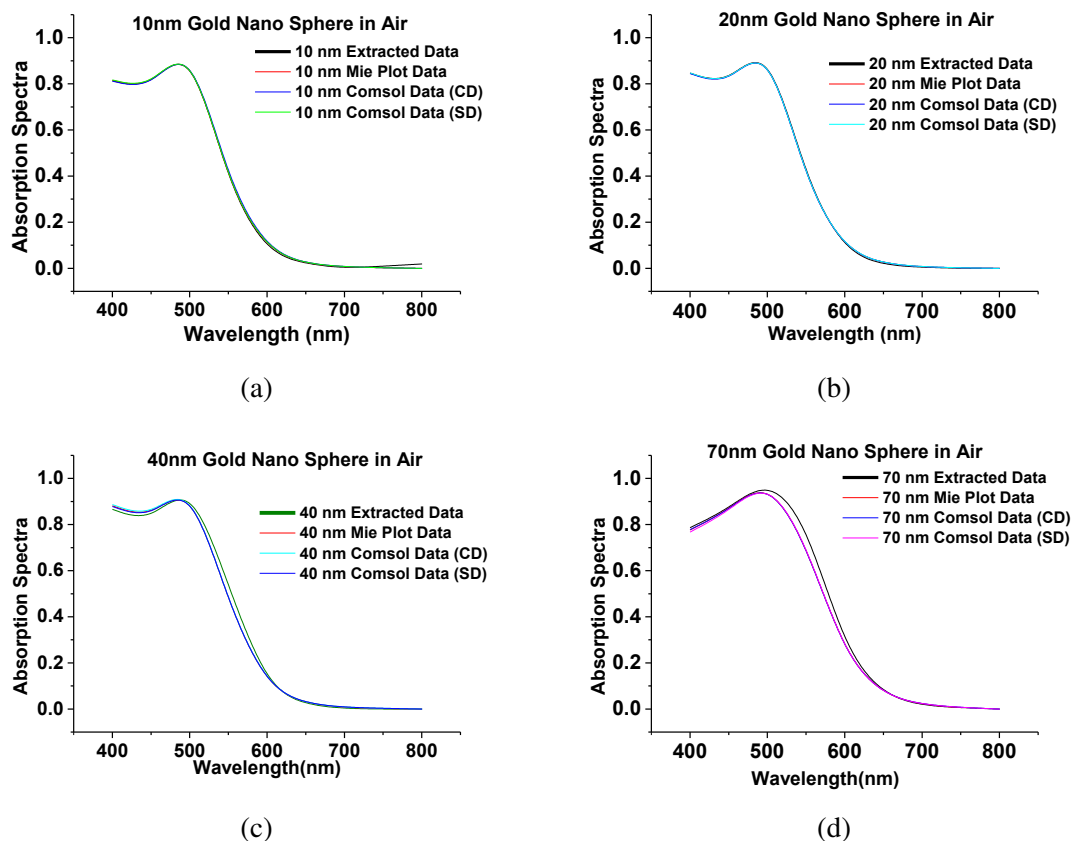


Fig. 2.5 Comparison of in-house simulated results with already published work (a) Shows the absorption spectra of gold nano sphere of 10 nm radius. (b) Shows the absorption spectra of gold nano sphere of 20 nm radius. (c) Shows the absorption spectra of gold nano sphere of 40 nm radius. (d) Shows the absorption spectra of gold nano sphere of 70 nm radius, and all the referenced results are taken from [74] and compared with the my own model.

Figure 2.5 shows the simulated absorption spectra using Comsol multiphysics of the gold nano sphere (in Cartesian and Spherical domain shown by blue and green curve, respectively as carried out here) and compared with the available Mie plot theory [72] (also simulated here) and the published work [74]. As the above results shows the excellent agreements on the Absorption Spectra, hence it can be concluded that our designed model working fine in both Cartesian and spherical co-ordinate systems as achieved results are almost similar with the published work. The performance of extinction efficiency for sphere with 10 nm, 20 nm,

Overview of Numerical Methods of Electromagnetics field theory

40 nm and 70 nm radius are shown in Figure 2.6 and compared with the published work to benchmark the accuracy of the designed model.

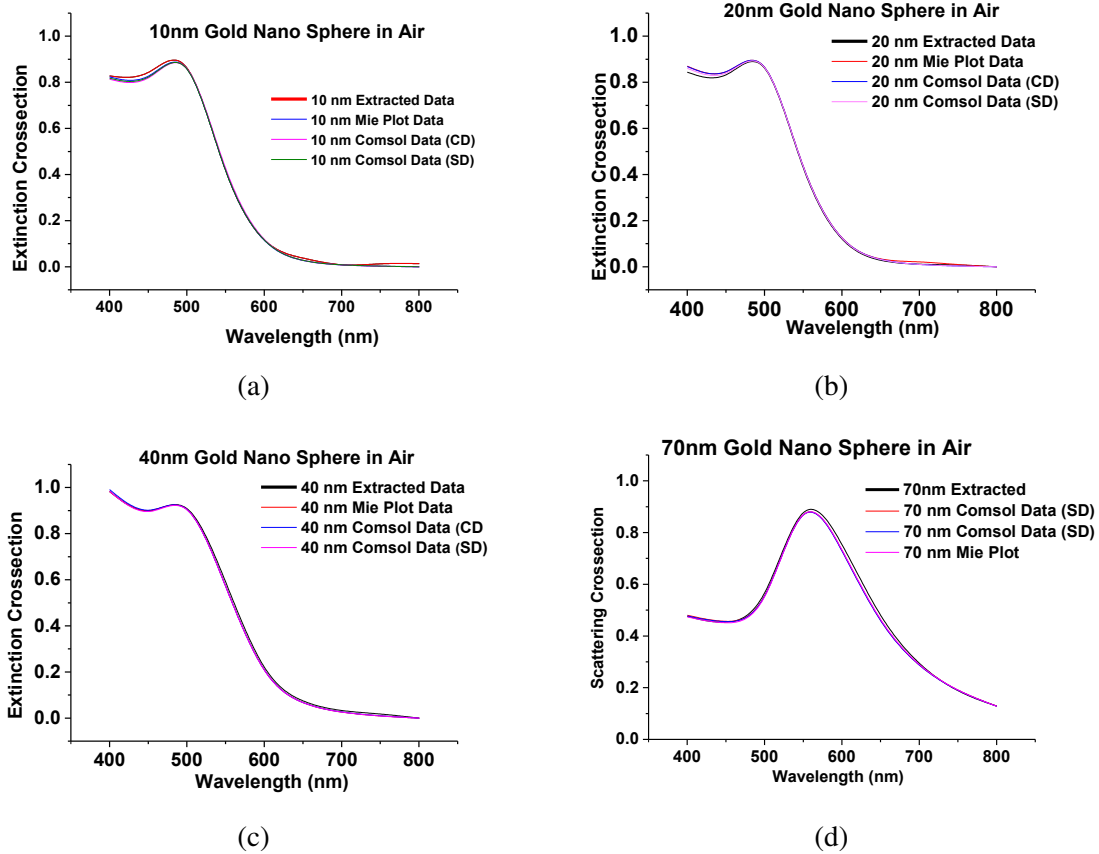


Fig. 2.6 Comparison of published results [74] with the in-house generated model the extinction Spectra of standalone gold nano sphere in air domain (a) 10 nm gold nano sphere in air (b) 20 nm gold nano sphere in air (c) 40 nm gold nano sphere in air (d) 70 nm gold nano sphere in air.

However, I have also calculated scattering efficiency for 40 nm and 70 nm radius as shows in Figure 2.7. Where black curve shows the results of the published work and red curve shows the dataset generated by using the Mie plot software. However, blue and pink curve shows the designed Comsol module dataset carried out by the candidate for 40 nm and 70 nm radius sphere to show the confidence in using Comsol by benchmarking

2.6 COMSOL Model Methodology and Validation

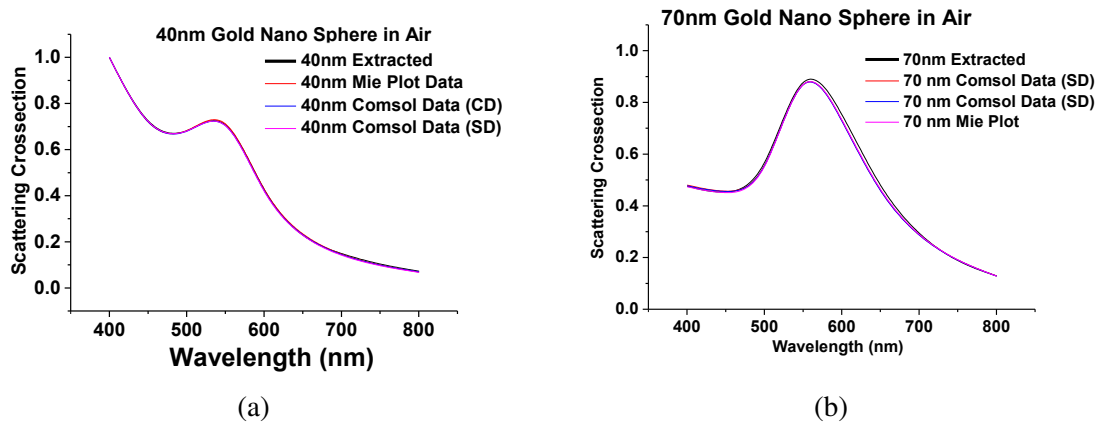


Fig. 2.7 Comparison of in-house simulated model with the extracted [74] Scattering Spectra of standalone gold nano sphere in air domain (a) 40 nm gold nano sphere in air (b) 70 nm gold nano sphere in air.

Additionally, the performance of the gold nano sphere submerged in water have also been carried out (design adopted from [75]). In this work, I have modelled the 40 nm radius gold nano sphere which was submerged in the water environment. Here, Figure 2.8a shows the comparison of our simulated work on of the extinction efficiency of the sphere (shown by blue curve) with the published work (shown by pink curve). Figures 2.8b and 2.8c show the normalized electric field profiles of the simulated and published works, respectively. In this way, to start the original research work I have tried to do sufficient benchmarking to get more familiarity of the FEM software by benchmarking the accuracy of our results.

Overview of Numerical Methods of Electromagnetics field theory

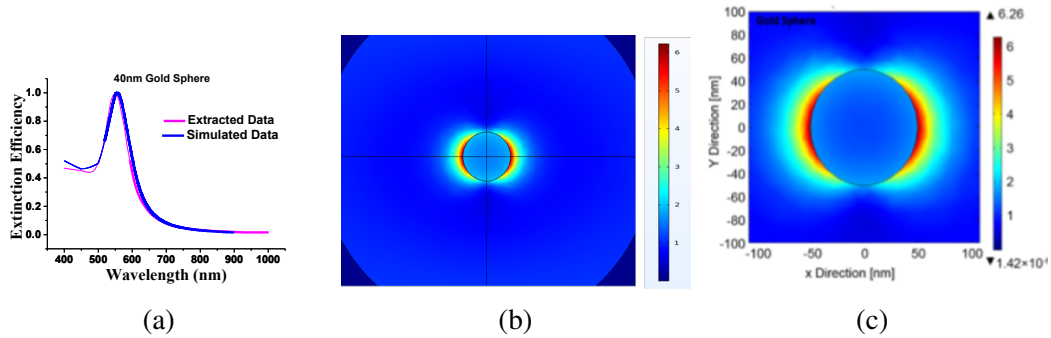


Fig. 2.8 Comparison of in-house simulated and extracted from [75] (a) Extinction Efficiency of standalone gold nano sphere of 40nm dia in water (b) Shows the inhouse simulated Normalised Electric Field of nano Sphere (c) Normalized electric field profiles profile reprinted from published article [75].

Next, I have extended the above shown results with the evaluation of the performance of different surrounding medium (from RI 1.2 to 1.42 with 0.01 step size) and simulated the designed FEM model to calculate the absorption cross-section shown in Figure 2.9a. Here, it can be seen that as the refractive index of the surrounding media in changing the spectra is shifting toward the higher wavelength. However, the similar patterns can be seen while calculating the scattering and extinction cross-section as shown in Figures 2.9b and 2.9c.

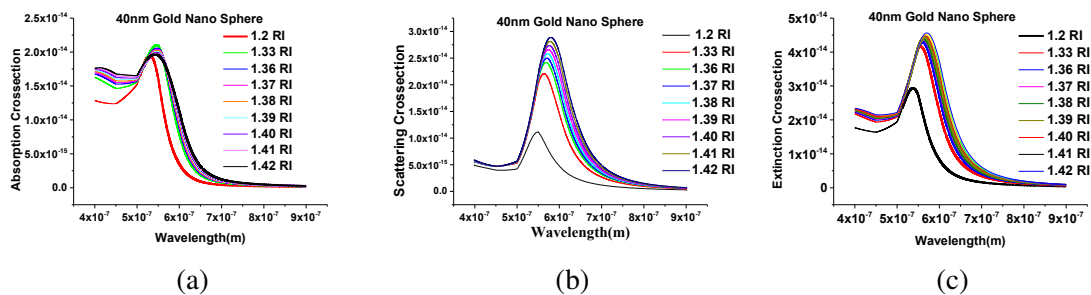


Fig. 2.9 Response of the 40 nm in-house simulated nano sphere in different surrounding medium (a) Absorption efficiency of standalone 40 nm gold nano sphere in mentioned refractive indexes. (b) Scattering efficiency of the same structure (c) Extinction efficiency response of the different RIs.

Furthermore, I have also studied the effect of the change in radius of the nano sphere. To study the structural effect of the nano sphere, I have simulated from 10 nm to 80 nm. In this

2.6 COMSOL Model Methodology and Validation

case, I have started from 10 nm radius to 80 nm with 10 nm step size, and calculated the scattering, absorption and extinction efficiencies, which are shown in Figures 2.10a, 2.10b and 2.10c, respectively.

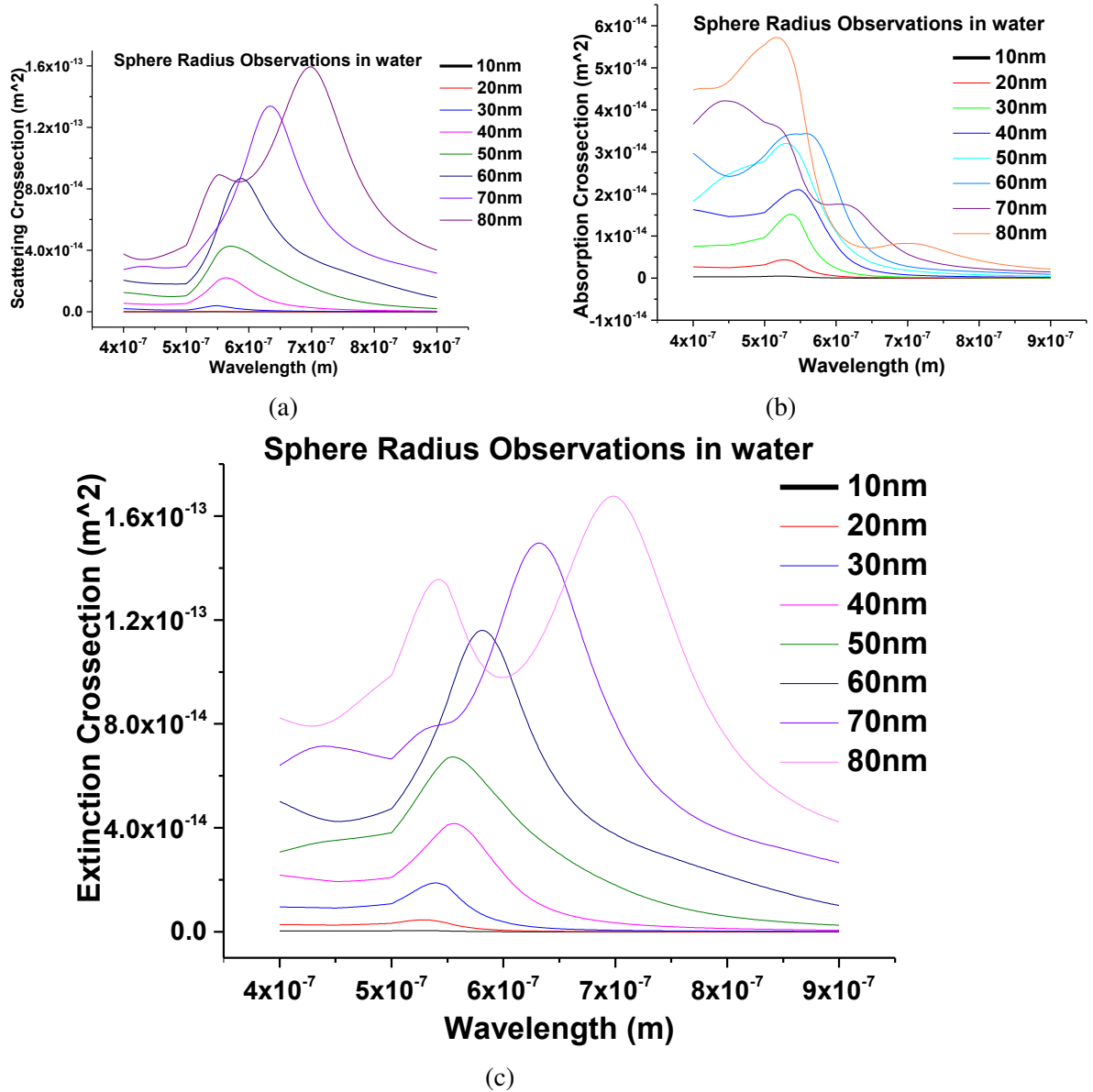


Fig. 2.10 Response of in-house simulated nano spheres submerged in water (a) Scattering coefficients of nano spheres (b) Absorption coefficients of the same structure (c) Extinction coefficients response of nano spheres with different radius.

One important thing here is to notice that as I am changing radius of the sphere the modes are changing after 70 nm radius as shown in Figure 2.10. It can also be seen that as the

radius of the sphere is increasing the intensity of the peak increases, hence from here it can be concluded that the geometrical structure plays an important role in *LSPRs*.

2.6.3 Periodic Gold Nano Disk

After successfully benchmarking and analysing the structural properties of gold nano sphere, next I have considered the periodic nano disk placed on the quartz substrate and benchmarked it with the Rizzato *et al.* [76]. The motivation behind this task was to benchmark this work to both experiment and theoretical work, and I can get stronger confidence in our developed model. In this work, Rizzato *et al.* [76] have not clearly mentioned the surrounding media; however they have used sodium chloride (*NaCl*) in their experiment for surrounding media. Hence, I have simulated for the refractive indexes (*RI* from 1 to 1.7 with 0.1 in step size) to identify which one is closer to their published result for sodium chloride (*NaCl*) to study the performance of the developed model with respect to the published work.

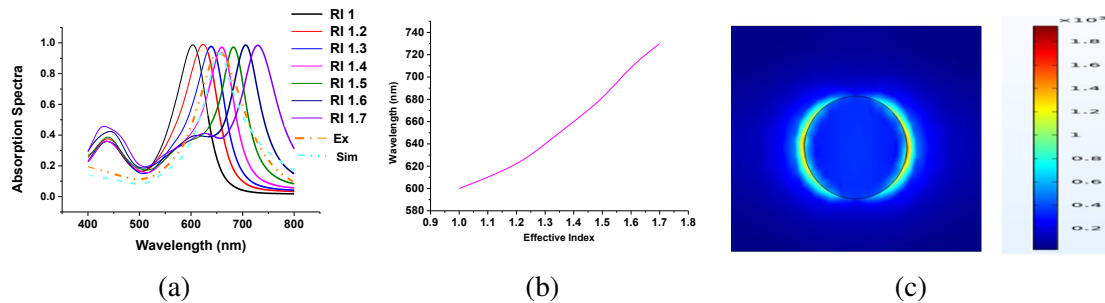


Fig. 2.11 Response of in-house simulated gold nano disk in different RIs (a) Absorption Efficiency of stand alone gold nano disk in different RIs (b) Linear Relation with RI and wavelengths (c) Model Profile of normalized Electric Field from the in-house simulated model.

Figure 2.11a shows the absorption spectra of the gold nano disk of 80 nm diameter and surrounding refractive index was varied from 1.0 to 1.7. The performance of the developed model was compared with the published experimental and simulation spectra shown by dashed orange and sky blue curves, respectively. From this, it can be concluded that when

2.6 COMSOL Model Methodology and Validation

the refractive index of the surrounding media was close to 1.4 in this case our simulated results agree well with the published work. From this findings I got the confidence on our modelling knowledge and extended it to visualize the plasmonic wavelength shift which is plotted with respect to refractive index variation of surrounding medium as shows in Figure 2.11b. From this figure, it can be concluded that wavelength shift is following linearly when the refractive index changes in the surrounding media. Additionally, Figure. 2.11c shows the electric field distribution of the gold nano disk along the $x - y$ plane.

2.6.4 Array of Gold Nano Holes

In this section, I have designed the gold nano holes where all the parameters are adopted from an earlier report [77]. Here, I have calculated the reflection/transmission and absorption spectra. All these nano holes designed here are surrounded by the water. I have shown the two modes from the transmission spectra/absorption spectra and their associated field distributions. Similar as above, the nano holes has been excited from the top and it generated the *SPR* which can be a good candidate for sensing applications and I can consider it for fluorescent molecules which can be attached with any analyte, and each molecule of fluorescent will behave as an amplifier and the detected signal can inform the concentration of any kind of analyte. Figure 2.12a shows the results published by Wu *et al.* [77] and in order to get confidence on our modelling skill, I have compared the mode profile of our designed model shown in Figure 2.12b. However, field distributions at the resonant wavelength are different for these two modes. As I discussed earlier that the slight change in geometries of any nano structures can create a difference in the spectral values. From here, it can be seen that the peak of the first mode do not agree fully, however the response of the mode profile for peak of second mode is more convincing. On the other-hand, it can also be seen that the mode profile of the nano hole are perfectly matching with the published results. The mode profile is analysed here to understand the fundamental difference between the two modes.

Overview of Numerical Methods of Electromagnetics field theory

These findings are particularly useful to guide the design of a metallic nanostructure-based plasmonic sensing system.

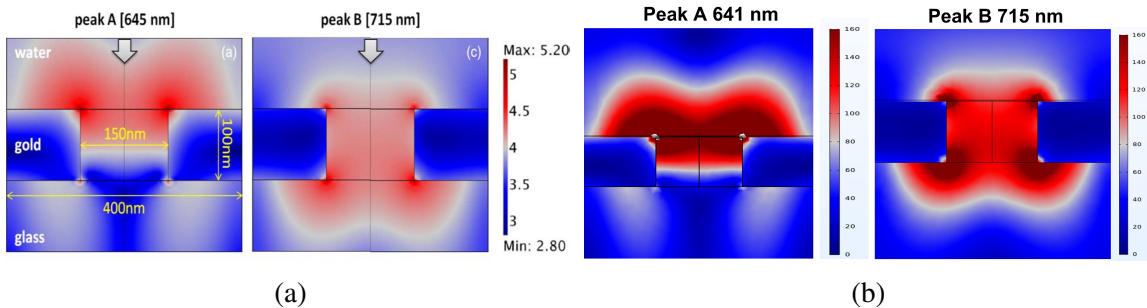


Fig. 2.12 Mode field distribution of in-house developed gold nano hole in water (a) Figure taken from [77] (b) In-house developed mode field distribution of the nano holes.

2.7 Mesh Considerations

In *FEM* modelling the size of the discrete element is determined by the mesh. Reducing the mesh size increases the number of elements and improves the accuracy of the model. However, the mesh size also significantly affects the computation time of the model, with large element numbers causing issues with memory allocation and ultimately preventing the model running. Therefore, a compromise between accuracy and computation time must be considered. Figure 2.13 shows a comparison of mesh sizes and the corresponding effect on plasmonic resonances must be identical at every mesh boundaries, it is necessary to match mesh conditions to reduce errors in the simulated data. This is especially important for the boundaries at the sides of the unit cell used to form an array. If the meshes are not identical at opposite sides, the perfect electric conductor and perfect magnetic conductor boundary condition will be affected and cause errors in the program. Therefore, copy face operations were used to match meshes on opposite boundaries of the nanorod unit cell. A larger mesh size can be used for larger dimensions, such as the matrix, glass substrate and *PML* without much effect on the accuracy. However, as the matrix and glass layers were in contact with the

2.7 Mesh Considerations

thinner gold underlayer and nano holes' dimensions, the mesh conditions had to be similar. In this research a custom mesh size was used, which allowed for equivalent mesh sizes on the boundaries. A maximum mesh size of 10 nm was used, with a minimum of 0.5nm in the surrounding media and a minimum value from sequence, obtained during computation, in the gold nanostructured media. These conditions allowed for larger elements throughout the most of the matrix and glass layers, which provided a compromise between the accuracy and the computation time.

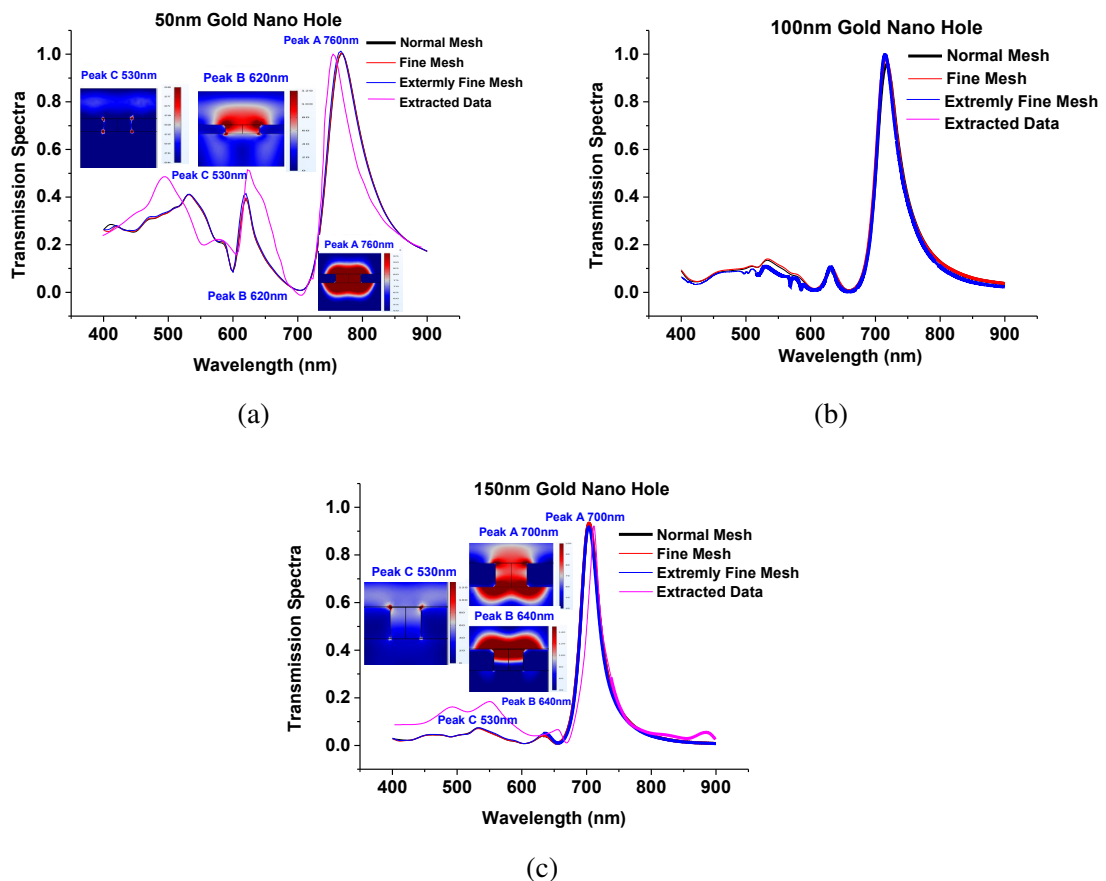


Fig. 2.13 Transmission Spectra of in-house simulated gold nano holes (a) Shows the transmission spectra of gold nano hole when height is fixed at 50nm (b) Comparison of generated and extracted Transmission spectra of (c) Model profiles of 150nm gold nano holes with transmission spectra.

Overview of Numerical Methods of Electromagnetics field theory

The transmission spectra has been calculated for the 150 nm hole diameter with 400 nm-pitch at different mesh sizes where it can be seen that as the mesh size is changing the spectral values are shifting a bit. Figure 2.13 shows transmission spectra for nanohole arrays in gold films of thickness 50, 100, 150, and 200 nm and compared with the published results [77] (shown by pink curves). In the calculations, one illumination conditions has been considered i.e from the water. It is clear from Figure. 2.13 that the transmission spectrum varies with the gold film thickness for transmission modes. As the film thickness is increased from 50 nm to 200 nm gradually, peaks at the lower wavelength of smaller the transmission spectra gradually reduced peak which was present in the Figure 2.13a. The mode profiles have also been shown by the inset figures.

Finally, it is well established that the finite element mesh components have a significant impact on the precision of *FEM*-based modal solutions also as the mesh size is refined the results are conversed very well with respect to the published work [77]. As a result, the quadrilateral mesh was utilised in all our simulations. As, *FEM* is heavily mesh dependent so refining is needed for two main reasons. One geometrical and other is mathematical. However, if we will have smaller elements with same degreed shape functions, the solution will be more accurate as seen in Figure 2.13 where, the performances of normal, fine, and extremely fine mesh size have been shown by black red and blue curves and show very nice agreement with the published work [77].

2.8 Summary

In summary, the Maxwell's equations in the differential and integral forms have been introduced. Maxwell's equations are generally used as a starting point for solving the computational domain problem by using different numerical approaches such as finite differences, finite elements, boundary integral, surface integral, and others. The importance of Finite Element Method has been discussed and explained that it can be used for numerical

simulations for more accurate representation of complex structures. In this chapter, the modelling techniques used to simulate the gold nanorod array surface have been presented. The development of the modelling sets made it possible to evaluate the model's underlying physics and mimic ideal conditions while also comparing it to theory and other modelling techniques. The finite element method (*FEM*) was chosen as it could be used to model any complex system with nanoparticle of any shape. It also allows in-depth visualisation of the simulated fields surrounding the nano particles and the position of intense field, which are the areas of localised field enhancement.

FEM software, COMSOL Multiphysics 5.5 was used to model single nanoparticles in free-space, on a substrate and finally nanorod array surface. The simulated results were compared with the theory, other reported numerical and experimental results, where applicable. Nanosphere results were in good agreement with the Mie theory. I have discussed the behaviour of the surface plasmon resonance including mathematical description. In addition, we have also shown the successfully benchmark of the result obtained from the in-house developed *FEM* model and compared with some key published articles in order to optimize the designed model to get the expertise in model design. For different nano structured shapes and index values, modal field components e.g. E_x , E_y obtained by using in-house model and these were compared with the published work, which have shown good agreement. I have also presented in-depth studies on exciting the SPR of an air(or water)–gold–glass structure illuminated from either water or air. Our studies show that reflection and scattering modes can excite the resonance at the air/water gold interface. Due to the changed optical power flow and surface layer power absorption, the optical field distributions have also been observed at the illumination direction or the form of nanostructures. These benchmarking could assist in determining the favourable illumination direction and also the effect of nano structures' shape in the design of the metallic nanostructure-based plasmonic sensing systems. Finally, in the last section of this chapter I have observed the effect of increasing mesh refinement

Overview of Numerical Methods of Electromagnetics field theory

which can increase the accuracy, but at the cost of increased simulation times. An irregular mesh with only increased resolution inside the nano structure with generated FEM code can be used. This does not increase the overall simulation times significantly, unlike regular mesh arrangement. Different types of mesh arrangements including progressive type and extra elements type mesh have been evaluated. Hence, the FEM method has been used as an alternative of any other available technique as it provides better meshing.

Chapter 3

Conceptualization of elliptical nano structures

3.1 Introduction

Nanostructures have lately attracted a lot of attention due to their numerous capabilities, and they have opened up a new way of thinking about growing nanotechnology for optical bio-sensing applications. Due to its effective localised surface plasmon resonance (*LSPRs*), nano shape antennas can give an excellent opportunity for single-molecule biological sensing applications [75]. Pharmacological sensors, bio-medicines, networking, photovoltaic panels, scanning, fuel cells, treatment of water, disease detection and mitigation, or enhancements all benefit from intense electromagnetic confinement due to *LSPR*. Nanotechnology has gained a lot of attention recently due to its great efficiency in absorbance, dispersion, extinction, and reflection/transmission at nanometer dimensions; yet, there are still a lot of untapped possibilities. The Drude Lorentz model is employed to compute the dielectric constant of a metal with free electrons in this research, and an unique coupled gold elliptical shaped nanoscale structure is evaluated.

Conceptualization of elliptical nano structures

Despite the fact that Synge presented the theory of near field microscopes in 1928, it was never extensively investigated due to the manufacturing limitations of that era [78]. Bailey and Fletcher acquired a patent for Electromagnetic Wave Converters in 1973 [3], that was the first report of a nano antenna that resembles contemporary nano-antennas [3]. Wessel later revealed a notion for high field containment due to small nanoscale metallic surfaces, that can be observed by using Scanning Microscopy [79], and emphasised the relevance of surface plasmon resonance of these nano-sized particles in 1985. Alvin M. Marks published a super sub-micron electron beam writer for visible sunlight to electrical power transformation in 1989 [5]. The influence of various plasmonic antenna designs and characteristics for an array of applicants were discussed in that article. In 2004, Atay *et al.* successfully manufactured circular periodical array of gold antennas exhibiting high resonance and far-field patterning [6]. Likewise, Lahiri *et al.* developed unevenly split ring resonators for biological substance identification [7].

Surface Enhanced Raman Spectroscopy (*SERS*) employs nano antennas, that have the benefit of resonating concurrently in the visible and infrared ranges [8]. Nano paired antennas of various forms, including the Bow-Tie, are also available [9–12]. Nanodisks [13–15], Nanorods [16–18, 11] and Nano elliptical-shaped antennas have also been reported [19, 20] in visible region. In 2008, Fisher and Martin reported [80] a sensitivity of 500-510 nm/RIU for a Bow-Tie plasmonic nanoantenna with a 10 nm gap between their 20 nm narrower tips. In the same year, Anker *et al.* [81] reviewed the effect of shape and size of plasmonic nano-antennas and also sensing by surface enhanced Raman spectroscopy. In 2011, Sage *et al.* [82] reported the advances on localized SPR for spectroscopy-based biosensing using triangular shaped Ag nanoparticles with a thickness of 10 nm. They had functionalized multiples spectrally distinct nanoparticles by changing the material, shape, and size of constituent antennas to target different species for multiplexing. Recently, Chao *et al.* [83] reported higher sensitivity of 1120 nm/RIU using a metal-insulator-metal bus

waveguide side-coupled to a ring resonator comprised of many Ag nano rods. More recently, Armstrong *et al.* [84] and Mauriz and Lechuga [85] reviewed the rapid advancement of plasmonic biosensors for single-molecule biosensing.

Many reports of biosensors employing artificially produced metamaterials have lately been surfaced. In 2009, Kabashin *et al.* demonstrated a sensitivity of 30000 nm/RIU for two-dimensional porous gold nanorod arrangements a best plasmonic parabolic metamaterial for bio - sensing devices [16]. This bulk Kretschmann configuration, although being downsized for commercialized biomedical application, is not suited for further miniature integrated photonic detectors. In 2016, Sreekanth *et al.* [86] claimed a comparable sensitivities of 30000 nm/RIU for a grating linked parabolic metamaterial for bulk refractive index sensing. Despite the fact that the system was simpler and therefore more multiplexed than [16], it nevertheless used bulk plasmonic modes and required relatively sophisticated manufacturing and stimulation procedures. The usage of metamaterials and metasurfaces for sensing applications was examined by Lee *et al.* [87] in 2017. Garoli *et al.* [88] lately proposed a feasible reduced production and convenient excitation procedures employing nano-porous gold metamaterials, achieving a sensitivity of 15000 nm/RIU. Through numerical modelling and experimental studies, the foregoing talks demonstrate the potential outcomes of intense resonating and field confinement. Recently, a computationally efficient finite element method (*FEM*) [19, 20, 12, 21, 22, 9] and the versatile finite difference time domain method (*FDTD*) [23–27] gained popularity.

This chapter is organized as follows. Section 3.2 elaborates the description of the elliptical nanostructured geometries. Section 3.3 demonstrate the plasmonic interaction between the nano particles, coupling mechanism between the nanostructures and substrate. This section also covers the sensing mechanism of nano particles.

3.2 Expansion for Nanostructured Geometries

Provided nanospheres remain small enough, their optical properties can be determined accurately through use of the quasistatic approximation. However, for other nanoparticles typically utilised in plasmonics, such as nanorods; Mie theory is unable to predict light scattering and absorption behaviour. To predict the behaviour of non-spherical geometries, additional expansions are required, such as Mie-Gans theory [70]. By considering nanorods as ellipsoids, their optical properties can be approximated using the quasistatic approximation through the inclusion of a geometrical factor. Ellipsoids, described by equation 3.1, can be either prolate or oblate, referring to either elongated or flattened ellipsoid with shapes similar to a needle or disk respectively as shown in Figure 3.1

$$\frac{x^2}{a^2} + \frac{y^2}{b^2} + \frac{z^2}{c^2} = 1 \quad (3.1)$$

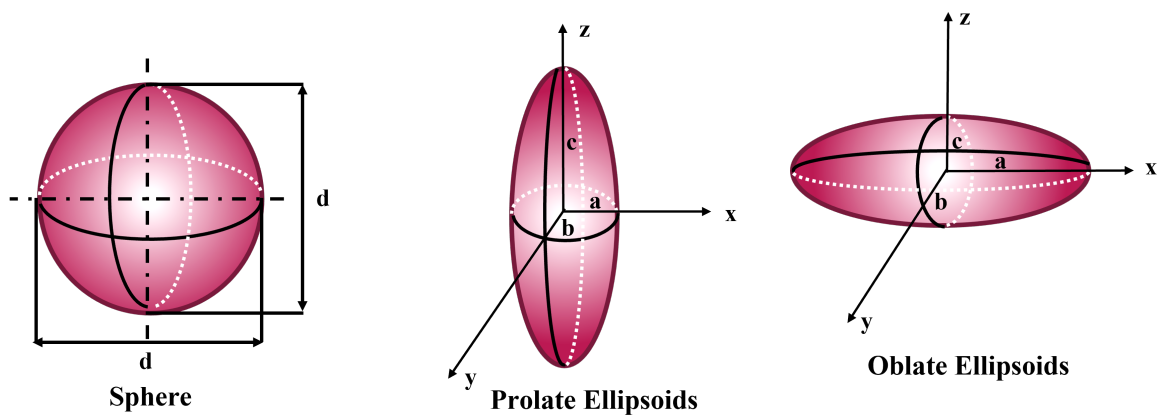


Fig. 3.1 Schematic of (a) Sphere (b) Prolate ellipsoids (c) Oblate ellipsoids with Semi-Axis Lengths, a , b and c in x , y and z directions respectively.

The ellipsoids are considered to have equal semi-axes ($a = b$) with solutions for prolate ellipsoids ($c > a = b$) used, rather than oblate ($c < a = b$) to approximate the shape of the

3.2 Expansion for Nanostructured Geometries

cylindrical nanorods. The polarisability can be derived through the quasistatic approximation, however the full derivation can be found in [89]. Considering the three axes of the ellipsoid, the polarisability depends on the orientation of the ellipsoid in the field, as given by equation 3.2 [90].

$$\alpha_i = \frac{4\pi}{3} abc \frac{\epsilon_m - \epsilon_d}{\epsilon_d + L_i(\epsilon_m - \epsilon_d)} \quad (3.2)$$

Where i represents the three axes and L_i is the depolarisation (or geometrical) factor in each direction. For cylindrical nanorods approximated by a prolate ellipsoid, the geometrical factor in the z -direction is given by L_1 in equation 3.3 [90].

$$L_i = \frac{1 - e^2}{e^2} \left(\frac{1}{2e} \ln \frac{1+e}{1-e} - 1 \right) \quad (3.3)$$

Where e is the eccentricity given by equation 3.4:

$$e = \sqrt{1 - \frac{a^2}{b^2}} \quad (3.4)$$

The geometrical factor in the x and y directions is equal ($L_2 = L_3$) and is given as a function of L_1 as shown in equation 3.5.

$$L_2 = L_3 = \frac{1 - L_1}{2} \quad (3.5)$$

Due to the different polarisation along the short and long axes of the ellipsoid, the optical properties along the axes will vary. At resonance, when the denominator of 3.4 approaches

Conceptualization of elliptical nano structures

zero, there are two examples are associated with the short and long axis oscillations, as seen in Figure 3.2, known as transverse and longitudinal modes respectively.

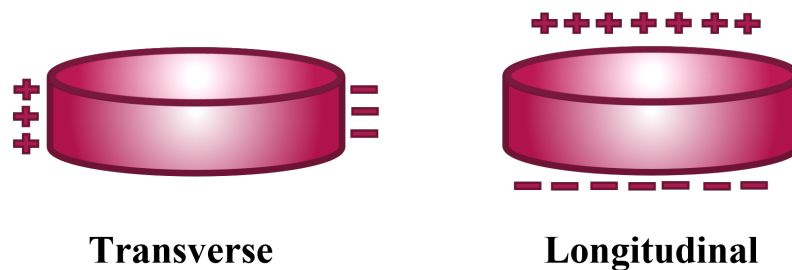


Fig. 3.2 Schematic of short and long axis oscillations of transverse and longitudinal resonance modes respectively.

3.3 Plasmonic Interactions

The theoretical solutions for nanoparticles assume that a single particle is isolated in a homogenous media. In reality, the nanostructures will typically be interacting with others while suspended in solution, evaporated, or fabricated on a substrate or aligned within an array. Each of these interactions affects the measured optical properties of the nanostructures. Additionally, the dependence of the resonance on the dielectric function of the surrounding media, as seen in equations 2.29 and 3.2 can be utilised for measuring changes in the local refractive index for sensing applications.

3.3.1 Nanostructure-Substrate Coupling

At a significant distance from a substrate, the optical response of the nanoparticle is similar to that in an isolated, homogeneous media. With decreasing distance between the nanoparticle and surface, the substrate interrupts the symmetrical field distribution surrounding the nanoparticles. For metal substrates, strong coupling between nanoparticles and surfaces occur with hybridisation of the localised plasmons on the nanoparticle and SPPs on the metal substrate. Nanoparticles also couple with image charges, which are multipoles induced on

the surface by the proximity of the plasmonic nanoparticle [90], as shown in Figure 3.3. Coupling between the nano-particle and substrate results in a red shift of resonance peak which is dependent on the separation between substrate and nanoparticle and thickness of substrate [91].

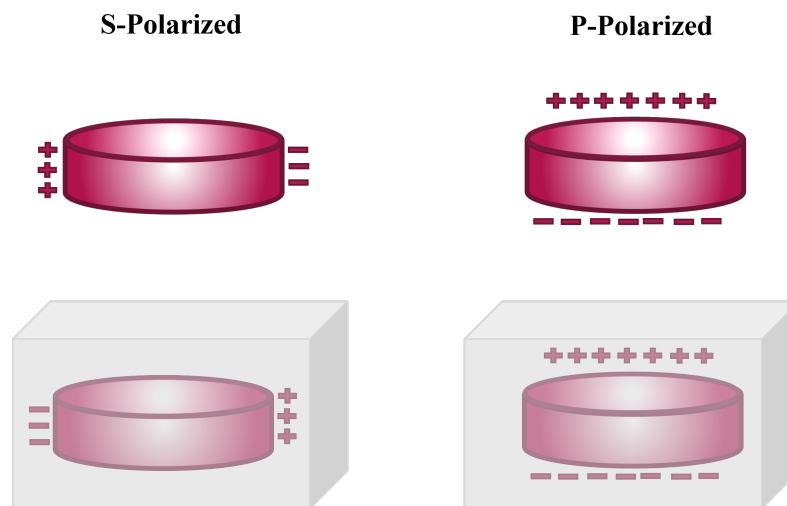


Fig. 3.3 Schematic representation of nano ellipsoid coupled to dipole image charges in substrate.

Dielectric substrates also couple with nanoparticles, with weaker interactions due to coupling only with image charges on the surface. However, the strength of nanoparticle dielectric substrate interaction can still be significant, with strength increasing for increasing dielectric permittivity (refractive index). With increased permittivity, the strength of the image and resultant interactions increase with image charges reduced by a factor of $(\epsilon - 1)/(\epsilon + 1)$ [92]. Additionally, the inclusion of the substrate which breaks the field symmetry surrounding the nanoparticles can result in higher order plasmon modes [90].

3.3.2 Sensing Mechanisms of Nanoparticles

Excitation of localised surface plasmons is dependent on the size, shape and material of the host nanoparticle, as defined in equations 2.28 and 3.1. However, the optical behaviour is also affected by the surrounding media, where a change in the dielectric constant (and refractive

Conceptualization of elliptical nano structures

index), results in a change of resonant properties. This inherent sensitivity can be exploited for detecting molecules for a variety of sensing applications as detailed in Section 4.2, where a change in surrounding media results in a shift in the resonance peak. Single nanoparticle-based sensors are capable of ultra-low limits of detection with 40 nm shifts reported for a single Ag nanoparticle [93]. Array based sensing results in a significantly smaller shift of peak but provides a better signal-to-noise ratio as signal occurs over a larger sensing platform. Due to the simpler setup, array devices are easier to use and take measurements and allow for higher throughput. In the sensor setup utilised in this research (Section 4), changes in the resonance peak are detected by a dip or peak in the signal measured through a sensor-gram. When a solution change or binding event occurs, the resonance peak is shifted from the baseline, causing either a peak or dip in the real-time response due to a higher or lower refractive index respectively.

3.4 Summary

The principle of the paired nano structure has been explained in this chapter and concept of an elliptical-shaped nanostructure has been thoroughly discussed with detailed optical characteristics of paired nanostructures. The effect of the coupling between the nanostructure and the substrate is also discussed in this chapter. Finally, the nano particle's sensing mechanism after it was placed on the substrate is also explained in this chapter.

Chapter 4

All-Opto plasmonic controlled bulk and surface sensitivity analysis of paired nano-structured antenna with label-free detection approach

4.1 Introduction

Gold nano antennas have been used in a variety of biomedical applications due to their attractive electronic and optical properties which are shape and size dependent. Here, a Periodic paired gold nano structure exploiting surface plasmon resonance is proposed which shows promising results for refractive index (RI) detection due to its high electric field confinement and diffraction limit. Here, single and paired gold nano structured sensors are designed for real-time RI detection. Full-Width Half-Maximum (FWHM) and Figure-of-Merit (FOM) are also calculated, which relate sensitivity with the sharpness of the peak. The effect of different possible structural shapes and dimensions are studied to optimise

All-Opto plasmonic controlled bulk and surface sensitivity analysis of paired nano-structured antenna with label-free detection approach

the sensitivity response of nano sensing-structures and identifies an optimised elliptical nano antenna with its major axis a , minor axis b , gap between the pair g , and heights h being 100 nm, 10 nm, 10 nm and 40 nm, respectively. In this work, I have investigated the bulk sensitivity, which is the spectral shift per refractive index unit due to change in the surrounding material, and this value was calculated as 526-530 nm/RIU and the FWHM was calculated around 110 nm with a Figure-of-Merit (FOM) of 8.1. On the other hand, surface sensing is related to spectral shift due to refractive index variation of the surface layer near to the paired nano antenna surface, and this value for the same antenna pair was calculated as 250 nm/RIU for surface layer thickness of 4.5 nm.

Section 4.2 describes numerical methods and model optimization with 2 subsections containing the performances of the optimized nano structure and comparison of the optimized structure with the published work. Section 4.3 shows the performance surface sensing for the designed nano structure after that this chapter concludes in Section 4.4. Finally novelties of the proposed work is described in Section 4.5.

4.2 Numerical Methods and Model Optimization

A frequency domain technique based on *FEM* has been used in this study [19, 20, 12, 21, 22, 9] to evaluate the plasmonic field scattering of gold nano-particles. Figure 4.1 illustrates the dimensions of nanostructures, with a and b representing the major and minor axes, h indicating the height, and g identifying the separation gap.

Figure 4.1a shows a graphical representation of a paired gold nanostructured antennas on a quartz substrate. The single cell of quartz substrate on which a coupled nanosized structure is implanted is referred to as a 3D arrangements. Comsol Multiphysics, which is based on the FEM, was used to perform all of the computational simulations. The electron transfer in metals are precisely similar to the complex dielectric permittivity, and the electric and magnetic fields are coupled by this permittivity to keep the computational findings. Drude

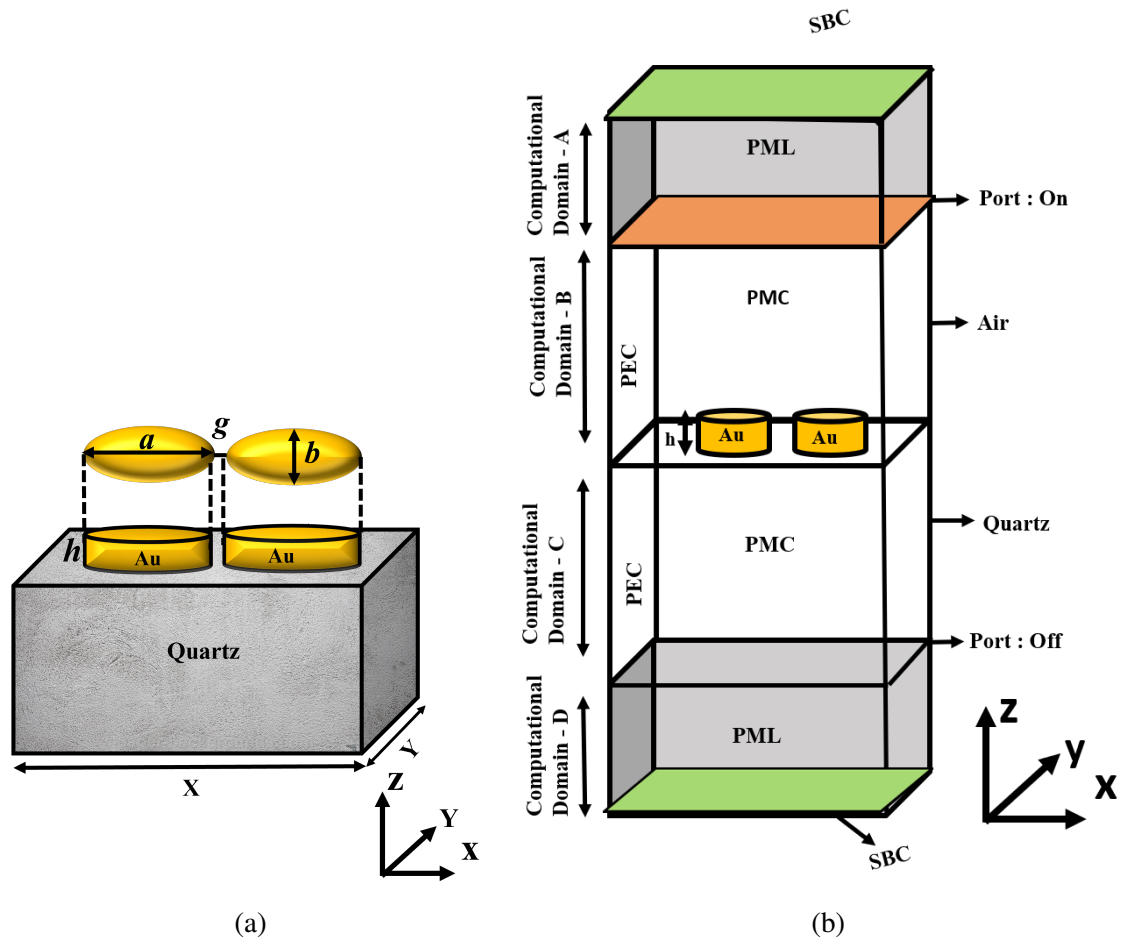


Fig. 4.1 Designed model on COMSOL Multiphysics (a) Top and Side views of a paired elliptical shaped gold nano antenna (b) Computational model of paired gold nano antenna along with the boundary conditions.

Lorentz model has been used to obtain the property of the gold because it focuses on the free-electron present in the metals which causes surface plasmons resonance. To minimize the computational cost, I have modelled single unit cell with appropriate boundary conditions, as shown in Figure 4.1b with waves activation ON, a metallic nano structure was stimulated in the z -direction from the top by x -polarized light, and Scattering boundary conditions (*SBC*) were positioned at the bottom and top of the finite element model. To get the field distribution, transmission and reflection patterns, the complete numerical problem was solved in the frequency domain. The whole structure was discretized into 'study' mesh elemental

All-Opto plasmonic controlled bulk and surface sensitivity analysis of paired nano-structured antenna with label-free detection approach

scale in the *FEM* method. To eliminate backward reflection distortions in the calculations, Perfectly matched layer (*PML*) with a height of 200 nm was added at the top of the air domain and bottom of the quartz substrate. The periodicity were 400 nm and 200 nm in the x and y axes, respectively. The metal discs were first set at a height of 40 nm from the quartz substrate's surface. Perfect magnetic conductor (*PMC*) and Perfect electric conductor (*PEC*) have been employed to enforce the structure's periodicity in the x and y directions, respectively. The sensitivity research of four distinct designs is provided in this chapter: single sphere and single disc, paired disc, and elliptical shaped paired disk antennas, as shown in Figure. 4.2

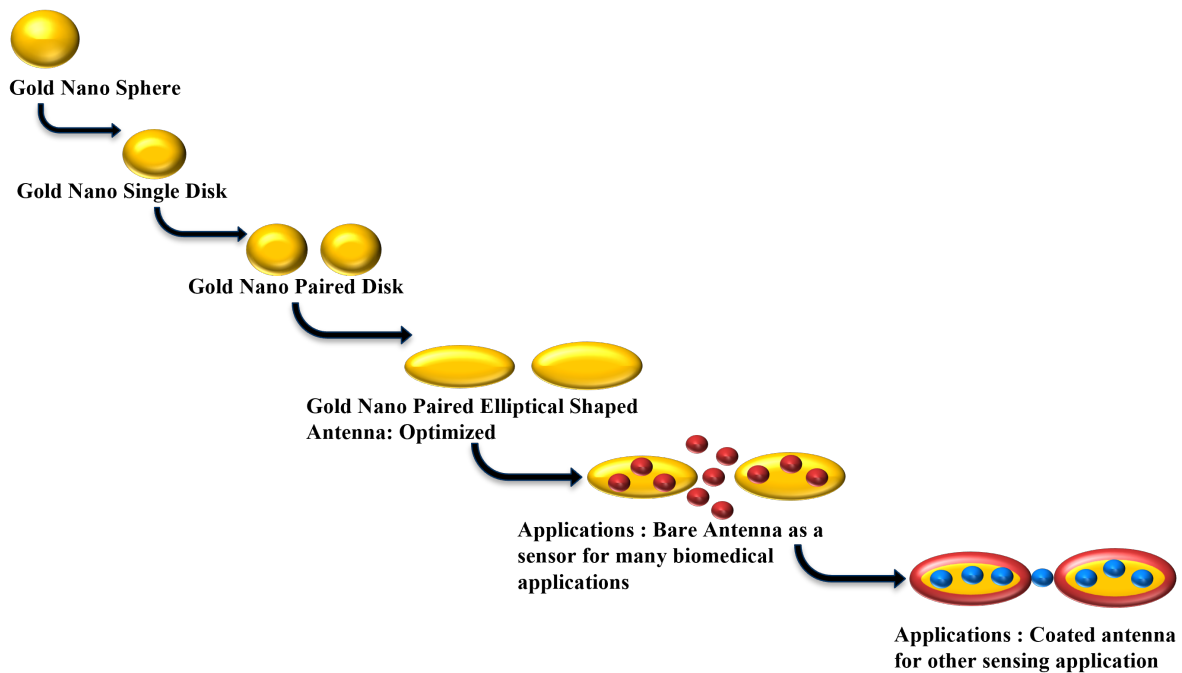


Fig. 4.2 Work approach of the designed computation model.

To examine the physical plasmonic characteristics, the *FEM* is used to solve the standard Maxwell equations while taking into account the harmonic dependency of the electric field $E(r,t) = E(r)e^{-j\omega t}$. Throughout the simulation, I employed the Helmholtz equation, that can be obtained from standard Maxwell's equations and is illustrated below.

$$\nabla^2 \mathbf{E} + k_0^2 \epsilon \mathbf{E} = 0 \quad (4.1)$$

The wave vector is represented by k_0 . Here, a harmonic propagating field is recognised with $\mathbf{E}(x, y, z) = \mathbf{E}(x, y, z)e^{j\beta z}$, where β is the propagation constant. The propagation dependency in the z directions are represented by the complex form $\gamma = \alpha + j\beta$, and when for loss-less case, $\alpha = 0$, $\gamma = j\beta$. The antenna is excited by an x -polarized wave in the z -direction incident from the upper surface, which forms the LSPR following interactions with the gold nano shapes. The proposed structure's sensitivity (nm/RIU), S , is defined as the ratio of resonant wavelength λ_{res} shift to the change in ambient index of refraction δn_s (RIU):

Figure 4.3 shows the sensitivity of a single disk and sphere. The sensitivity measurements of a solitary sphere of various diameters mounted on a quartz platform are shown by a green curve, and this value is approximately 25 nm/RIU for $d = 70$ nm - 120 nm. Due to the obvious amplitude modulation and transition in the plasmonic wavelength, these single spheres can be used to detect the target in complex media like a serum, as discussed by Chen *et al.* in 2010 [94], and the initial response of the base pairs and trimers of spheres was shown by Deep *et al.* in 2015 [95]. The sensitivity of a single disk is also displayed by a blue curve when its thickness is 80 nm to explore the influence of diameter. It can be seen that when the diameter of the disk is reduced, its responsiveness decreases, even for such a thicker disk, its sensitivity is comparable to that of a sphere of similar diameter. However, as the height is reduced further, the sensitivity increases substantially. A red curve depicts the sensitivity calculations of a single disk of 40 nm height, which is practically saturating to 125 nm/RIU when the diameter exceeds 100 nm. When the height is reduced to 10 nm, as illustrated by the black curve, the sensitivity of a circular disk increases to 225 nm/RIU as the diameter is raised to 120 nm, and then it becomes saturated. A purple dashed-dotted curve also depicts the sensitivity of a single elliptical disk. The major axis, a , is kept constant at 100 nm, while

All-Opto plasmonic controlled bulk and surface sensitivity analysis of paired nano-structured antenna with label-free detection approach

the minor axis, b , is changed. It can be seen that as b , the minor axis, is decreased, the sensitivity rapidly increases, reaching 350 nm/RIU at $b = 10$ nm.

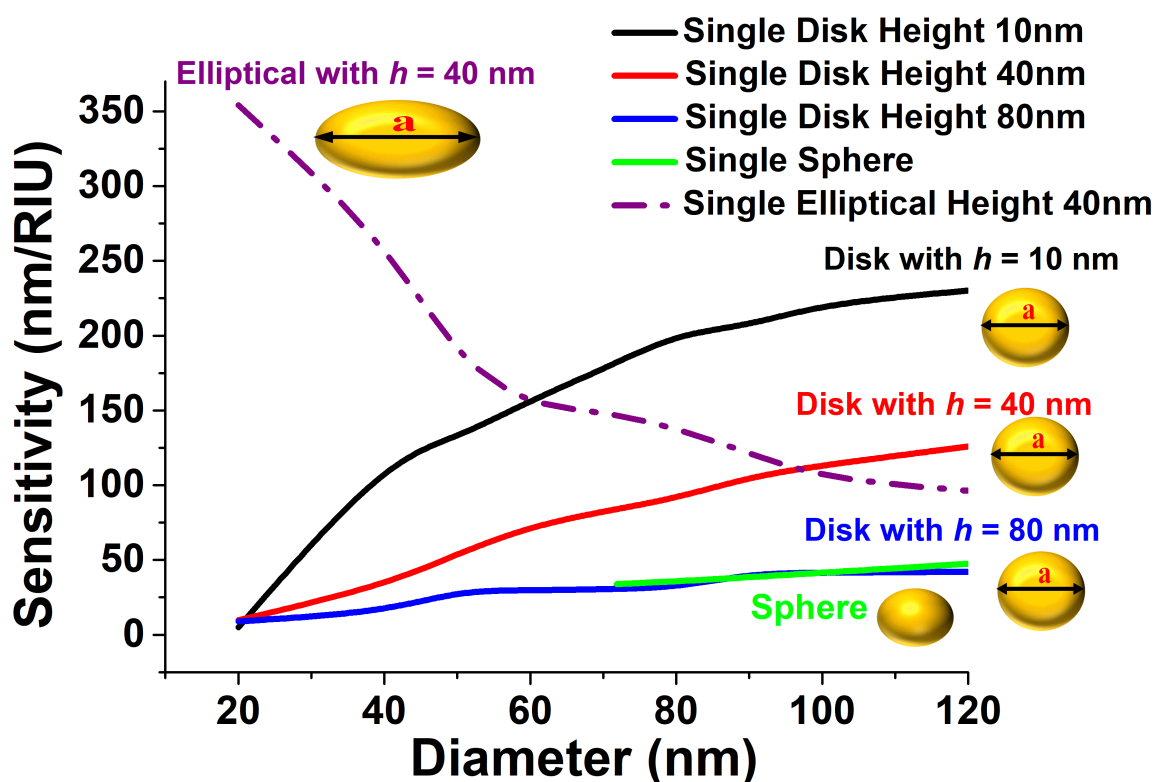


Fig. 4.3 Sensitivity variation with the diameter of single nano disk of 10 nm, 40 nm and 80 nm height, sphere and single elliptical disk when $a = 100$ nm, $b =$ varied (10 nm to 100 nm), $h = 40$ nm.

This highlights an excellent opportunity: the sensitivity of a non-circular elliptical disc may be significantly boosted even with its smaller overall size, but the sensitivity of a bigger circular disc is very much restricted. The diameter, major and minor axes, and thickness of the disks all affect sensitivity, however to produce a reasonable evaluation, a fixed height of 40 nm is considered in the next section for all the devices which can be easily manufactured.

The significant electric field entrapment at the sharp corners of the elliptical disk can be seen in Figure 4.4a. This obviously shows that the field is more confined due to the absence of circumferential symmetry. Figure 4.4b shows the variation of the electric field E_x in the x -direction through the centre of a solitary elliptical disk. At the edges of the solitary

4.2 Numerical Methods and Model Optimization

elliptical disk with $a = 100$ nm, $b = 10$ nm, and $h = 40$ nm, this figure likewise displays a significant normalised electric with field intensity up to 18000 V/m. With $a = b = 100$ nm and $h = 40$ nm, this value is approximately twice that of a circular disk. In comparison to a singular circular disk, a single elliptical disk can be regarded a viable option for sensing purpose due to its higher electric field confinement.

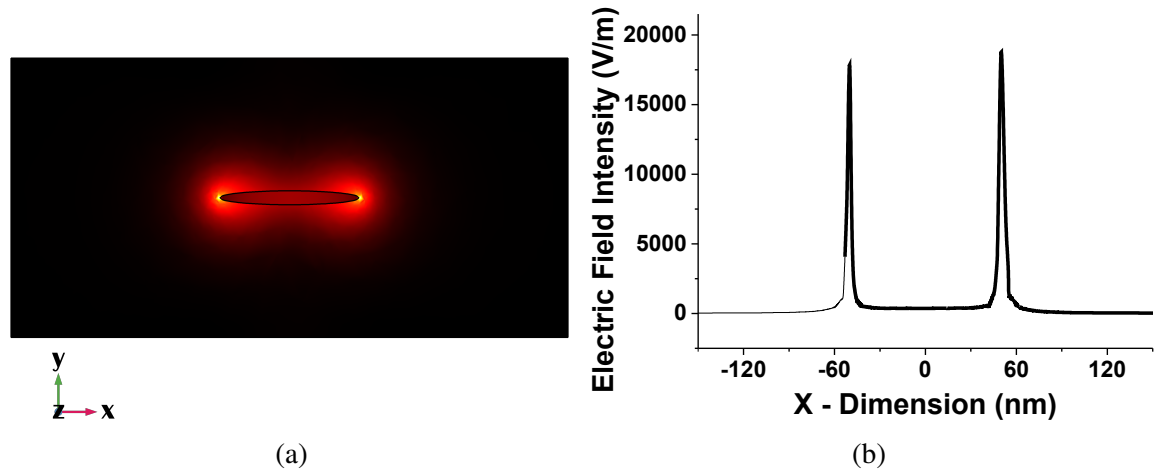


Fig. 4.4 (a) E_x , mode field profile of a single elliptical disk antenna when $a = 100$ nm, $b = 10$ nm and $h = 40$ nm (b) Electric field variation along the x -axis for a single elliptical disk when $a = 100$ nm, $b = 10$ nm and $h = 40$ nm.

4.2.1 Paired Elliptical shaped Nano Antenna

Since it is usually recognized that a paired disks, also referred as a dimer, could increase the field intensity across their gaps, so our the next step is to assess both paired circular and elliptical disks. As a result, the transmission spectra of a 100 nm gold nano disk surrounding by a material with varied refractive indices are displayed in Figure 4.5a.

All-Opto plasmonic controlled bulk and surface sensitivity analysis of paired nano-structured antenna with label-free detection approach

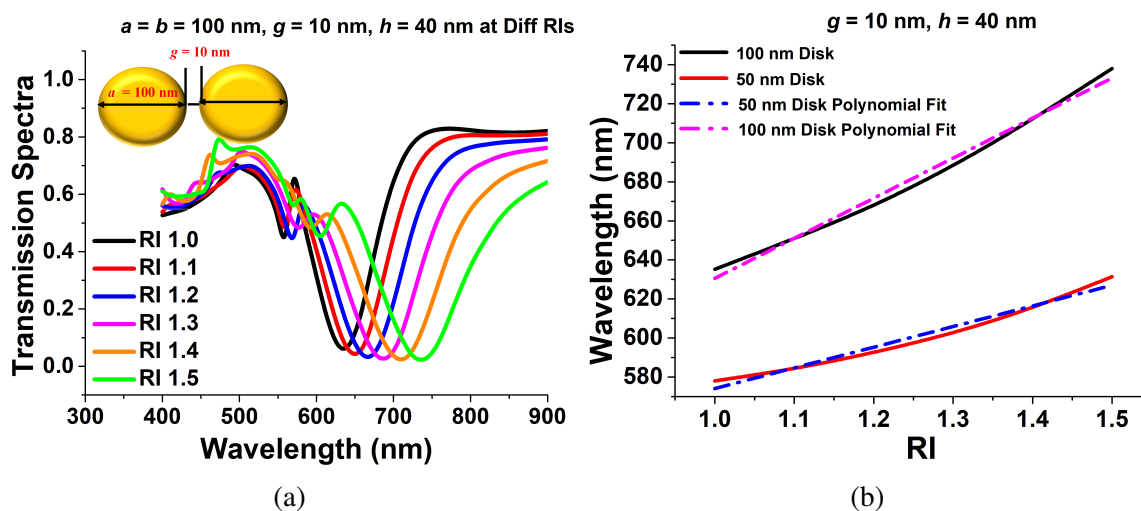


Fig. 4.5 (a) Transmission Spectra of paired 100 nm circular nano disk with 10 nm separation distance and 40 nm height (b) Sensitivity and R-Square Error calculation of 100 nm and 50 nm paired circular disk.

One can see that when the refractive index increases, the resonating wavelength shifts to a higher wavelength. The separation gap, g , and the height of the disks, h , are set to 40 nm and 10 nm, respectively. The resonating wavelength increases when the surrounding refractive index, RI is increased, as shown in Figure 4.5b. The slope of these two curves, 105.79 and 205.18 for diameter 50 nm and 100 nm, respectively, are used to compute the sensitivities of the coupled circular nano disks. A nearly linear relationship between wavelength fluctuation and RI variations has also been established. For 50 nm and 100 nm diameters, the R-square errors were estimated as 0.98915 and 0.9137, correspondingly, indicating a nearly linear correlation. The acquired sensitivity of the 100 nm coupled disk is obviously bigger than that of the 50 nm paired disk, as illustrated in Figure 4.5b.

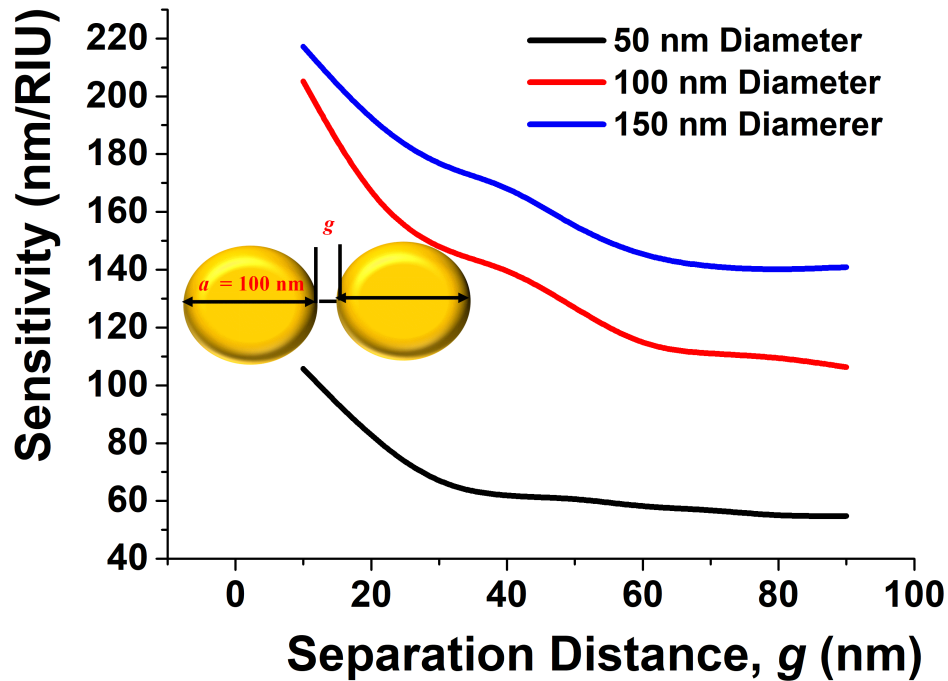


Fig. 4.6 Sensitivity analysis of paired circular nano disk of 50 nm, 100 nm and 150 nm diameter with the different separation distance.

Since sensitivity is affected by the spacing between the circular paired disks, next, its influence is investigated, and the sensitivities of disk with diameter 50 nm, 100 nm, and 150 nm are plotted against the separation distance in Figure 4.6. It should be observed that when the separation distance between the disks, g , is high, the sensitivity is equivalent to that of a single disk, however sensitivity improves when the separation distance, g , is reduced. As a result it can be seen that the sensitivity of a coupled disk is always greater than that of an individual disk. Zhao *et al.* presented an Au nanoparticle on a nano spherical shape with an separation gap, g of 0.82 nm [96]. It is also demonstrated herein that as the circular disk's diameter d increases, so does its sensitivity. The sensitivity of an elliptical-shaped paired nano disk is then investigated by changing its minor axis b from 10 nm to 100 nm while retaining the major axis a fixed at 100 nm. The antenna's height is set at 40 nm. These coupled nanostructures were stimulated with a linearly x polarised light in the z direction, with primary polarisation parallel to the major axis a . Transmission spectra at various index

All-Opto plasmonic controlled bulk and surface sensitivity analysis of paired nano-structured antenna with label-free detection approach

of refraction values were used to optimise the sensitivity. Figure 4.7a shows transmission spectra for a selected design with various surrounding medium (n). Here, 100 nm, 10 nm, 10 nm, and 40 nm are used as the major axis, a , minor axis, b , separation distance, g , and height, h , respectively. Because the design concept exhibits a greater efficient change in resonating wavelength, it could be employed as a refractive index sensor and is a good contender for RI detecting applications. The narrow band coupled nanostructures' spectral absorption may also be modified to fit the distinctive absorption spectra of selected RI in order to identify targeted media in the IR range.

4.2 Numerical Methods and Model Optimization

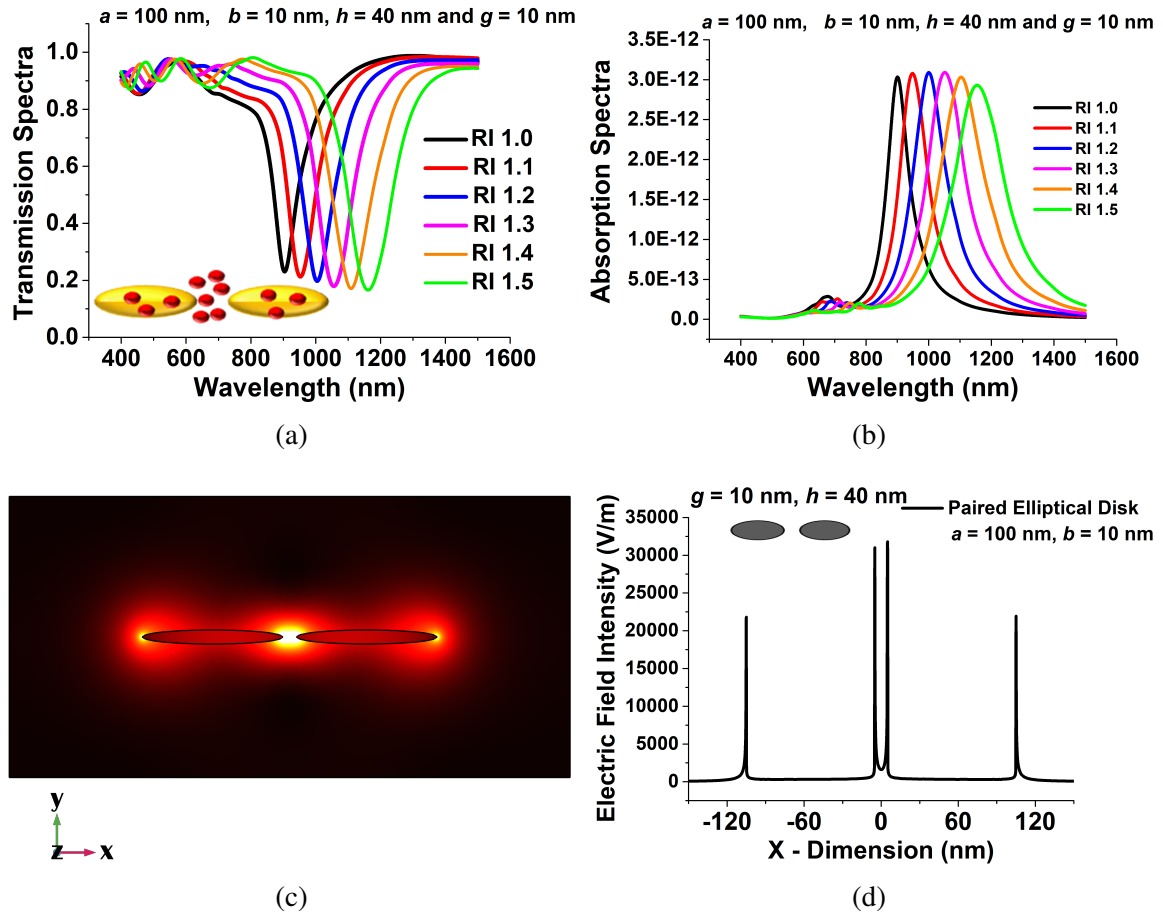


Fig. 4.7 (a) Transmission spectra of the optimized paired elliptical antenna with 100 nm, 10 nm major and minor axes, respectively with 10 nm separation distance g and 40 nm height, h (b) Absorption Spectra of the same structure (c) E_x , mode field profile of the optimized paired structure (d) Variation of Electric field along the x -direction of the optimized elliptical disk of 100 nm paired circular nano disk with 10 nm separation distance, g and 40 nm height, h .

Figure 4.7b illustrates the absorption spectra of the developed coupled nano antenna array for six RI values, which validates the observed transmission spectra and demonstrates sensing responses. Applied electric intensity in the separation region and extremely high electric field containment in the centre of the coupled antenna are shown in Figure 4.7c. The intensity of the localised electric field is critical for label-free identification. Because the highest electric field developed in the centre of the separation gap in the designed structure, such an ultra-strong electric field can be used for sensing applications.

All-Opto plasmonic controlled bulk and surface sensitivity analysis of paired nano-structured antenna with label-free detection approach

Figure 4.7d depicts the variation of the electric field E_x in the x -direction across the centre of elliptical antenna pair. Although electron conduction provides an efficient force at the surface of the paired device, the electric field in the separation gap region is significantly enhanced, as shown in Figure 4.7d. The maximum normalised electric field, shown by a black curve in Figure 4.7d, reaches up to 35000 V/m at the an inner edge of the paired elliptical disk for $a = 100$ nm, $b = 10$ nm, $g = 10$ nm, and $h = 40$ nm, indicating that the highest field level of intensity is more than 50% greater in the gap especially compare to the field at the outer edges. It can be regarded a superior choice for biosensor applications owing to its increased strength of electric field containment. The applied electric field profile shows that by reducing the minor axis, a considerable field increase may be observed at the sharp corner of a coupled structure. This coupling causes the LSPR improvement because the elliptical structures interact more strongly as they approach nearer through one another. When the separation distance was larger, the change in transmission and absorption spectra of the resonating wavelength was smaller, therefore a smaller separation distance is recommended to generate an intense electric field concentration. The maximum localised field intensity forms due to the coupling of surface waves on nanostructures, as shown in the aforementioned figures, and could be an ideal contender for RI sensing applications. This indeed very sharp behaviour can also be useful for scattering constrained EM waves, such as label-free RI identification by surface-enhanced Raman scattering and a wide range of many other Point-of-Care application domains.

4.2.2 LSPR sensing calculation of optimised structure

Enhanced sensitivities are indeed the principal designing requirement for an excellent detector, however the sharpness of the reflection and transmission curves are also essential for quick identification. I have concentrated on crucial device metrics namely Sensitivity (nm/RIU), Full-Width Half-Maximum (nm), Figure-of-Merit, and R-Square Error in this subsection.

4.2 Numerical Methods and Model Optimization

The variations of the resonating wavelength with the index of refraction for three distinct major axis, a values are shown in Figure 4.8a. The sensitivity (nm/RIU) is computed using a polynomial linear fit of the sensitivity analysis, and the slope, S , is obtained as 320 nm/RIU with 0.9974 R-Square error for $a = 60$ nm (as seen by black curve). Furthermore, at 467.69 nm/RIU with accompanying 0.9985 R - Square error, the S for 80 nm is computed somewhat better than that for $a = 60$ nm, as illustrated by a red curve. Finally, the sensitivity, S was computed at 526.12 nm/RIU for $a = 100$ nm with 0.9996 R - Square error, as shown in Figure 4.8a by a blue curve.

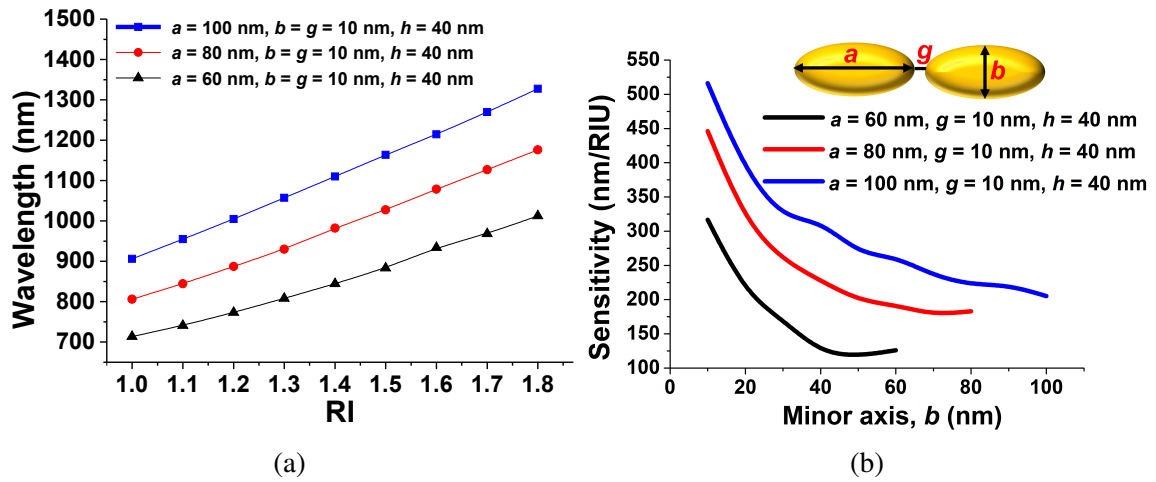


Fig. 4.8 (a) Polynomial Fit at when a axes were at 100 nm, 80 nm and 60 nm at RI from 1.0 to 1.8 (b) Sensitivity variation with the minor, b when major axis, a were fixed at either 100 nm, 80 nm or 60 nm and with fixed at 10 nm separation gap, g and height, $h = 40$ nm.

The variation of the sensitivity, S with the minor axis, b for three fix values of $a = 60$ nm, 80 nm and 100 nm with fixed $g = 10$ nm are shown in Figure 4.8b. It can be seen that as the major axes, a increases from 60 nm to 80 nm and to 100 nm, the sensitivity, S is increased as shown by blue, red and black curves, respectively, in Figure 4.8b. Figure 4.8b shows the change of sensitivity, S , with the minor axis, b , for three fixed values of $a = 60$ nm, 80 nm, and 100 nm with $g = 10$ nm. The sensitivity, S , improves as the major axes, a , increases from 60 nm to 80 nm and then to 100 nm, as illustrated by the blue, red, and black curves in Figure 4.8b. Sensitivity was evaluated as approximately 170 nm/RIU for $a = b = 80$ nm, then

All-Opto plasmonic controlled bulk and surface sensitivity analysis of paired nano-structured antenna with label-free detection approach

subsequently increased up to 450 nm/RIU for $b = 10$ nm, as indicated by a red curve. The sensitivity, S , was calculated to be 250 nm/RIU when $a = b = 100$ nm, and rapidly increases to 520 nm/RIU when the minor axis, $b = 10$ nm, as represented by a blue curve. It demonstrates that by reducing the minor axis, b , for a large major axis, a , relatively high sensitivity may be attained. The sharpness of the resonance curves affects measurement precision, which can be evaluated using the $FWHM$, which is identified as the difference between two wavelengths when the response is half of its highest value:

$$FWHM = \lambda_1 - \lambda_2 \quad (4.2)$$

Where λ_1 and λ_2 are the wavelengths, presented as an inset in Figure 4.9a, when the transmission is half of the highest amplitude.

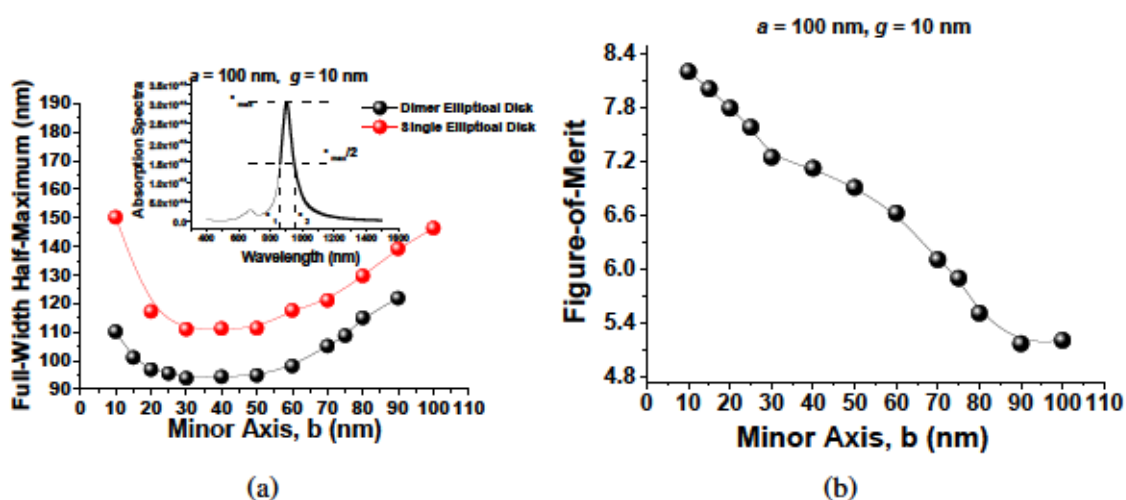


Fig. 4.9 (a) Variation of FWHM with the different minor axes, b when major and separation gap were fixed at 100 nm and 10 nm, respectively (b) Comparison of Figure-of-Merit (FOM) calculation at different minor axes when major axis and gap were fixed at 100 nm and 10 nm respectively.

The $FWHM$ of a singular elliptical disk first decreases as the minor, b axis is decreased and achieves a lowest value of 120 nm for b between 30 nm and 40 nm, and then it increases

4.2 Numerical Methods and Model Optimization

as shown by a red curve in Figure 4.9a. The similar tendency can be seen for the paired elliptical disks, where when the minor axes, b is reduced, at first $FWHM$ decreases until it reaches a minimum value of 95 nm for minor axes, b within 30 nm and 40 nm, and then it increases, when b reduces further, as shown by a black curve in Figure 4.9a. As a consequence, I can assess alternative designs based on their $FWHM$ values. I need a high sensitivity, S , as well as a sharper resonance (lower $FWHM$) in the proposed study, therefore the Figure-of-Merit (FOM) may be regarded a significant parameter for the development of a coupled nano antenna system. Here, FOM can be defined as the sensitivity to the $FWHM$ ratio:

$$FOM = \frac{S(nmRIU^{-1})}{FWHM} \quad (4.3)$$

Figure 4.9b shows the variations of FOM with the minor axis, b . The major axis, a , separation distance, g , and height, h , are kept constant at 100 nm, 10 nm, and 40 nm, respectively, in this case. Shreekanth *et al.* [86] examined a comparable FOM , but instead of $\Delta\lambda$, they have used $\Delta\omega$. When the minor axis is narrowed below 30 nm, even if the sensitivity increases exponentially (shown in Figure 4.8b), FOM has only been slightly enhanced, since its $FWHM$ was increased in this instance. The sensitivity variation for a single and paired circular and elliptical disk is shown in Figure 4.10a. It can be seen that when the antenna's height h is decreased, S increases in all circumstances. However, with a reduced antenna height, S of a paired circular disk (represented by a curve for $a = b = 100$ nm) is higher than that of a single disk (shown by a black curve for $a = b = 100$ nm). However, the sensitivity of an elliptical paired disk (represented by a blue curve, with $a = 100$ nm and $b = 10$ nm) displays the maximum values most often at shorter heights ($a = 100$ nm, $b = 10$ nm). Figure 4.10a further shows that when the antenna height, h , is more than 60 nm, sensitivity stays nearly constant. The sensitivity analysis for circular and elliptical paired discs is shown in

All-Opto plasmonic controlled bulk and surface sensitivity analysis of paired nano-structured antenna with label-free detection approach

Figure 4.10b. Their height, h , and separation gap, g , are 40 nm and 10 nm, respectively, in this case. When $a = b = 100$ nm, the sensitivity of a circular disk (with $a = b$) rises as its diameter increases, reaching roughly 220 nm/RIU.

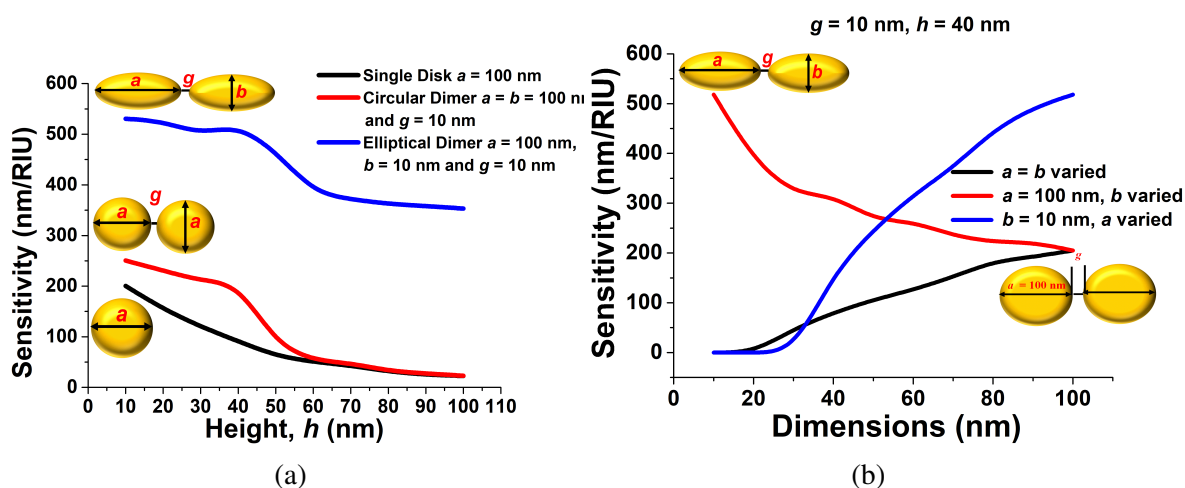


Fig. 4.10 (a) Sensitivity comparison of Single, Double disk and optimized Paired elliptical nano antenna with 10 nm separation gap and 100 nm major axes. (b) Sensitivity comparison of the variation of major axes a , minor axes b and paired disk variable.

These observations are comparable to those published by Tsai *et al.* [97] for the circular dimer, albeit it should be emphasised that they used a considerably larger disk. When the major axis, a , is set at 100 nm, the sensitivity evolution of a paired elliptical disc with the minor axes, b , is depicted by a red curve. Even though the sensitivity of a circular, especially for a paired disk, may be increased by expanding its size, it is demonstrated that whilst the sensitivity of an elliptical disk pair can indeed be improved by rather decreasing the minor axis, b , as illustrated by a red curve. The 526-530 nm/RIU was considered high sensitivity at the 10 nm minor axis, thus I have considered it for future investigations. Although the minor axis, b , is constant at 10 nm and the major axis, a , is altered, the sensitivity of a paired elliptical disk is shown by blue curve. It should be highlighted that when $a = 100$ nm, that is the identical value as the left most peak of the red graph, a higher sensitivity of 526-530 nm/RIU may be reached. As a is reduced, the sensitivity decreases, and the asymmetry also decreases. I performed Full wave mathematical modelling to evaluate the

4.3 Surface sensing Outcomes of the Paired Elliptical nano structured antenna

different analytical information, then used our findings to develop periodic coupled nano antenna designs for possible bio-sensing applications. The modelling findings reported here show that the engineering techniques can be utilised to optimise sensor sensitivity for many applications. Furthermore, I demonstrate that for a paired elliptical disk with $a = 100$ nm, $b = 10$ nm, $h = 40$ nm, and $g = 10$ nm, a paired micro antenna with sensitivity of 526-530 nm/RIU and $FWHM$, FOM of 108.86 nm, and $8.19 RIU^{-1}$ can be achieved. The sensitivity obtained can be used in biosensors and new biological imaging techniques. Tsai *et al.* also [97] showed that by employing a coupled nanoscale ring can also boost sensitivity by up to 50%, while our study indicates that for elliptical dimers, sensitivity can indeed be raised by more than 100% while utilising a considerably a much shorter size of the antenna.

4.3 Surface sensing Outcomes of the Paired Elliptical nano structured antenna

Furthermore, for label-free sensing, the surface sensitivity of the structural parameters was determined by calculating the electric field intensity adjacent to the nanoscale antenna. Surface sensitivity is affected significantly by the increased electric field strength along the edges and in the gap region. The presence of a sensing target can alter the sensing layer's refractive index, thickness, or even both. The surface sensing transmission spectra are presented in Figure 4.11a when the refraction indices (n_s) of a 4.5 nm thick sensing layer was modified for $a = 100$ nm, $b = 10$ nm, $h = 40$ nm, $g = 10$ nm. As the RI of the surface layer increased from 1.4 to 1.6, the resonating wavelength shifted towards greater resonating wavelength, Illustrated by the black, red, and blue curves. The sensitivity values at various surface thicknesses when $a = 100$ nm, $b = 10$ nm, $h = 40$ nm, and $g = 10$ nm are shown in Figure 4.11b. In all the sensitivity analyses, the RI of the surrounding medium was specified to 1.33 for water, while the refractive index of the surface layer was adjusted to n_s . Figure

All-Opto plasmonic controlled bulk and surface sensitivity analysis of paired nano-structured antenna with label-free detection approach

4.11b shows that as the thickness of the surface layer increases, so does the sensitivity, that could reaches up to 240 nm/RIU.

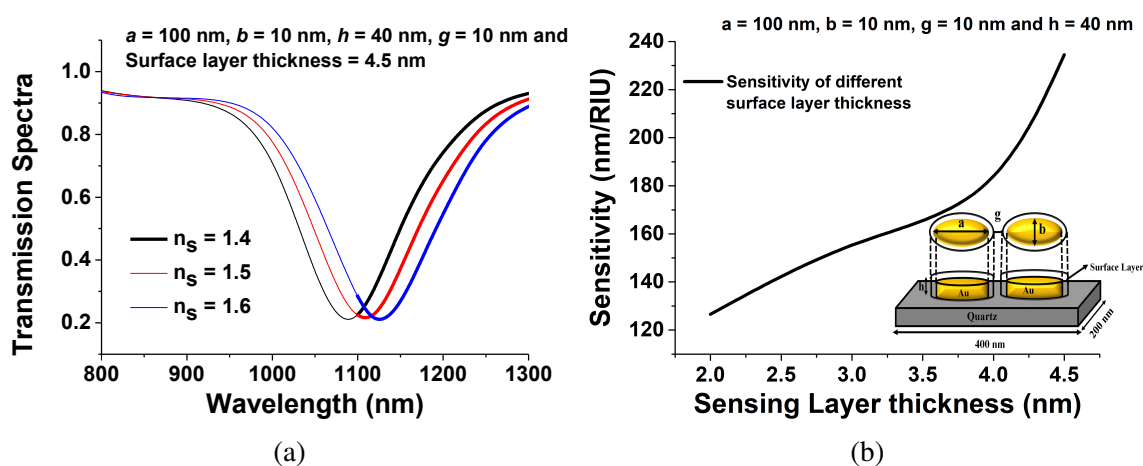


Fig. 4.11 (a) Transmission spectra for surface sensing of the optimized paired elliptical antenna disk when $a = 100$ nm, $b = 10$ nm, $h = 40$ nm, $g = 10$ nm and surface layer thickness = 4.5 nm (b) Surface sensitivity analysis of the optimized elliptical disk when $a = 100$ nm, $b = 10$ nm, $h = 40$ nm.

The sensitivity and *FWHM* of the proposed paired structure were also compared to previously published work and are given in Table 4.1. The suggested design has a higher sensitivity than previously reported publications. The comparison of published results in many aspects with our innovative technique of the developed structure, which seems to have high sensitivity and *FWHM*; thus, our conclusions are fairly encouraging when compared to the previous information. The parameters specified (Sensitivity (nm/RIU), *FWHM* (nm), and Figure-of-Merit (*FOM*)) can be used to describe sensing effectiveness and to analyse various attributes in order to expand its functionality.

4.3 Surface sensing Outcomes of the Paired Elliptical nano structured antenna

Table 4.1 Comparison of published work with the optimized paired structure.

S.No.	Designed Antenna (nm)	Full-Width Half-Maximum (nm)	Sensitivity (nm/RIU)	Ref.
1.	Square Shape (h = 30, g = 30)	125	—	[98]
2.	Disk Shape (h = 60, g = 14)	147	—	[99]
3.	Bow Tie Shape (h = 90, g = 65)	280	—	[100]
4.	Disk Shape (h = 40, g = 55)	109-113	—	[19]
6.	Nano shell (d = 50)	—	60	[101]
7.	Nano rods, cubes and bipyramids	—	195-288	[102] [103]
8.	Silver nano particles (h = 50)	—	200	[104]
9.	Gold Nano Square (h = 100)	—	167-327	[105]
10.	Nanodisk (h = 1)	—	200-350	[106]
11.	Nanotubes (h = 100, g = 55)	—	250	[107]
12.	Elliptical Antenna	95-100	510-530	Proposed

4.3.1 Model Investigation and Its Applications

In this chapter, optimized design have been used to show the efficient performances in terms of sensitivity and FWHM and next this design has been tested for detection of 2-propanol (IPA) concentration through its corresponding refractive indices, which are adopted form [108], and shown in Table 4.2.

All-Opto plasmonic controlled bulk and surface sensitivity analysis of paired nano-structured antenna with label-free detection approach

Table 4.2 Comparison of published work with the optimized paired structure.

C	0%	10%	20%	40%	60%	80%	100%
RI	1.3330	1.3420	1.3514	1.3642	1.3717	1.3742	1.3776

Figure 4.12a shows the transmission spectra of aqueous solution of 2-propanol (IPA) at different concentrations where the black, pick, blue and orange curves show the 0%, 20%, 60%, and 100% IPA concentration, respectively. Figure 4.12b shows the calculated FWHM with the IPA concentration having different refractive indices. From this figure it can be observed that at different IPA concentration (shown by pink dots) the FWHM was calculated as ~ 135 nm; however, it increases for higher refractive index values as shown by a black curve. On the other hand, Figure 4.12c shows the resonating wavelength with the refractive indices by a black curve with its highest value nearly 1320 nm at 1.8. In this figure, the variations of resonating wavelength for IPA solution are also shown by pink dots at around 1100 nm. Figure 4.12d shows the plasmonic wavelength shift of antenna placed in IPA solution compared to its placement in the vacuum. In order to calculate the value of the shifted plasmonic wavelength, the plasmonic resonating wavelength (when antenna was presented in inert environment) was substrated from the wavelength (when antenna was presented in different concentration of IPA as shown in Figure 4.12d). In this way, the potential application in detection of IPA aqueous solution at different concentrations from 0% to 100% has been shown by a black curve in Figure 4.12d. Pink dashed lines show the corresponding refractive index of aqueous solution of IPA at different concentrations from 0% to 100% with respect to resonating wavelength. A strong argument can be made here that the optimized design can be a useful candidate for many homogeneous RI sensing applications.

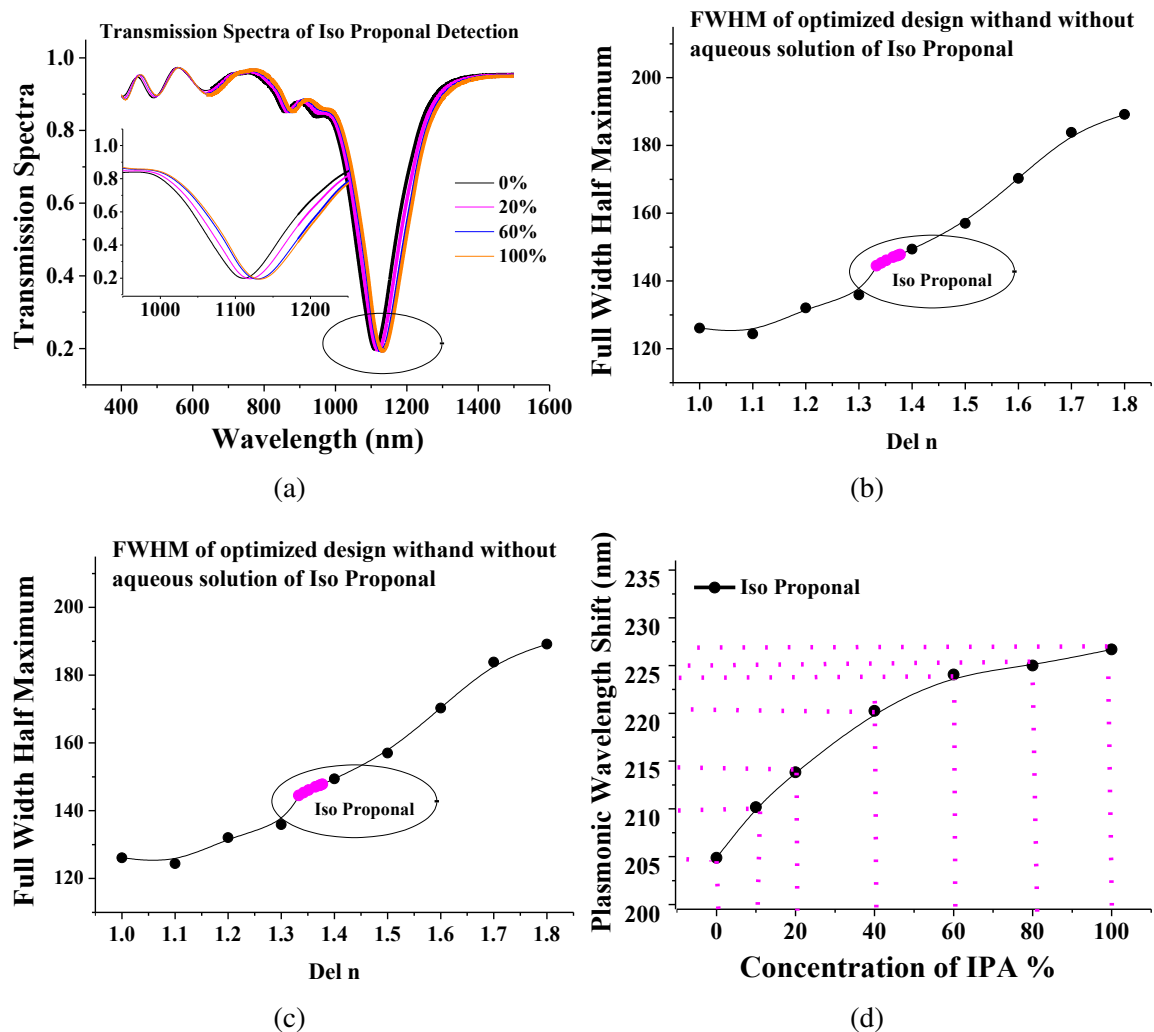


Fig. 4.12 (a) Shows the transmission spectra of different IPA concentrations (b) Demonstrate the FWHM variation of 2-propanol (IPA) with different RIs (c) Shows the resonating plasmonic wavelength with refractive index values (d) Shows the shift in resonating wavelength with the 2-propanol (IPA) concentration.

4.4 Summary

Finally, owing to their very attractive optical functionality which are shape and size dependent, gold nano antennas have been considered in a wide range of biological sensing applications. The surface and bulk sensitivity capability of these kind of periodic coupled gold nano structures is examined in this research leveraging the FEM for LSPR sensor design. It can be

All-Opto plasmonic controlled bulk and surface sensitivity analysis of paired nano-structured antenna with label-free detection approach

seen from this investigation that sensitivity increases as the height of the couple and distance between them decreases. When the diameter of a circular coupled disk is increased, its sensitivity increases. However, for an elliptical dimer when its asymmetry is increased, the sensitivity of a coupled elliptical disk increases. Thus, with a smaller elliptical disk, I can attain a significantly higher sensitivity. As a result, a significantly smaller elliptical antenna pair can attain substantially better sensitivity than the much larger circular disc [97]. For optimum design, the highest transmission dip and absorption peak were attained at almost 850 nm, whereas plasmonic degradation migrated towards greater wavelengths for different RIs. The sensitivity is computed as roughly 518-530 nm/RIU, with 109 nm *FWHM* and 8.35654 Figure-of-Merit (*FOM*) for a coupled elliptical disk with *a*, *b*, *h*, and *g* values as 100 nm, 10 nm, 40 nm, and 10 nm, respectively. When the sensing layer is 4.5 nm thick with a refractive indices ranging from 1.4 to 1.6 while the refractive index of the outside region is 1.33, the surface sensitivity was estimated as 240 nm/RIU. Furthermore, the adopted design show a high electric field distribution in the gap region. After successfully optimizing the nano antenna as a sensor, an aqueous solution at various IPA concentrations was used to observe the sensitivity of the engineered sensor, demonstrating its significant contribution to the advancement of potential innovative technologies for Point-of-Care, therapeutic, and water quality assessments, as well as a tool for regulating seawater salinity..

4.5 Novelties and Highlights

- The fundamental originality of this research is the revelation that by avoiding circular symmetry, as illustrated in this above chapter by employing an elliptical shaped disk, the electric field can be concentrated even more and the sensitivity of a solitary elliptical disk can indeed be improved.

- Furthermore, improved field patterns are shown, which closely correspond with almost twice the field strength particularly when compared to a circular disk, culminating in three times higher sensitivity.
- Additionally, the enhancement of field in the gap of an elliptical dimer, as well as the consequent increase in sensitivity is highlighted.
- It would be as easy to manufacture an elliptical dimer as it might be to construct a circular dimer, and even simpler than a ring-shaped dimer [83, 97]. However, a valuable feature will be that a much smaller elliptical-shaped dimer with its reduced area could achieve a similar high sensitivity as in a circular or ring-shaped dimer with a substantially greater dimensions.

Chapter 5

Artificial Neural Network Modelling for Optimizing the Optical Parameters of Plasmonic Paired Nanostructures

5.1 Introduction

Nanostructures have lately attracted a great deal of recognition from research groups due to their wide range of application fields, and the worldwide demand for nanotechnology is expected to reach USD 90 billion by 2021 [1] as manufacturing and service provider applications of nanostructures are expected to expand [2]. Likewise, Artificial Intelligence (*AI*) has grown and developed rapidly in the last ten years [37], with computer scientists and specialists, as well as many other investigators in other disciplines, embracing it. It has gained widespread acceptance in the field of science and technology for dealing with complex data-driven problems [38]. These models have unrivalled capacity to discover and foresee patterns in data, as well as uncover unanticipated tendencies that a normal observer could overlook [39]. It specializes in identifying hidden database systems and categorizing non-linear data information, allowing it a perfect fit for a variety of empirical methodologies. All

Artificial Neural Network Modelling for Optimizing the Optical Parameters of Plasmonic Paired Nanostructures

researchers focusing on light-matter coupling have advanced to a different level, supported by nanomaterials engineering, chemistry, and optoelectronic advancements, by exploiting Machine Learning (*ML*). This is facilitated by two contemporary events: The primary is the development of sophisticated optoelectronic devices; the second is the full integration of machine learning (*ML*) with physical/chemical disciplines for in-depth acquiring information which produced many novel discoveries [40].

Photonic technology has recently enhanced its capability by exploiting machine learning approaches, and the outperforming classical photonics, which is still inefficient in regards to effort and expense and provides restricted efficiency. As a result, numerous investigators had already changed their attention to ML and included it in a wide range of application fields, including comprehensible optoelectronic networks [41], plasmonics [42, 43], multimode fibres [109, 44], sensing [45–49], photonic crystal fibre [50], and nanotechnology [51, 110, 53–55]. Nanophotonics is an outstanding example of optical plasmon and strong localised fields that may be tuned for diverse purposes by modifying the shape and material choices of nanoparticle. In this work, paired nanostructures were investigated and the corresponding sensitivity, FWHM, FOM, and plasmonic wavelength were also estimated. The finite element methodology (*FEM*) was used to create and visualise these coupled nanostructures. It is commonly established that comprehensive complete vector illustration models of 3D photonic systems require days or weeks to solve a complicated system [111]. To address this problem, we developed a deep neural model based on the *Python (version 3.8.3)* framework, that revealed to be extremely fast at predicting their performances. Feedforward convolutional neurological systems have a lot of promise for solving difficult challenges in nano-optics, including adjusting the optical properties of single or paired nanostructures [112].

The neural network was developed and trained in the second stage using the acquired data-set from the FEM. The labelled entry variables, like the Major axis, a , Minor axis, b , separation gap, g , and height, h , are used to train to predict the corresponding output

values: sensitivities, *FWHM*, *FOM*, and plasmonic wavelengths. The learning process provides an approximated functionality that anticipates outcome quantities to initiate training of the constructed neural network. After adequate training, this developed model can produce output values for any new data variables. This training technique may evaluate its forecasted output to the actual output values and determine the mean squared errors (*MSE*) to demonstrate the performance of the models. Various prevalent *ML* paradigms can be used in the development and training of this deep learning model, including *pandas* [113] for data cleaning, *Scikit-learn* [114], which is a higher-end library chosen for regression analysis, *NumPy* [115] used for multi-dimensional arrays and matrices, and *pickle* [116]. Additionally, the *Pytorch*, which is an *ML* package premised on *Torch* tensors, has indeed been implemented [117–119]. *Pytorch* is an immensely renowned fully accessible, developed in 2016 by Facebook’s *AI* Research lab (*FAIR*) [120] based on the scripting language *Lua* [121], that it is equivalent to *NumPy* matrices, including the significant incentive of *GPU* support. It is indeed a powerful method since it assists in the acceleration of quantitative calculations, which may increase the performance of the neural network by up to 50 times. It has an easy-to-use *API*, making it straightforward to interact with *Python*. The usage of such excellent framework is justified since it enables the creation of dynamically computational chart that can also be updated in real-time, which is necessary throughout neural network training and testing. Even though *PyTorch* supports multiple rear ends rather than a solitary back end for *CPU*, *GPU*, as well as other fully functioning properties, we have used *FEM* simulation models in the rear end for data gathering, that is utilised for neural network training, and *Pytorch* and *Scikit-learn* at the front end due to its exceptional indispensable architectural style, which provides immediate and fast strategies. This study enables the calculation of photonic properties for coupled nano-structured devices using artificial neural network optimization algorithms.

5.2 The Convergence of Machine Learning with Nanostructural Devices

Commercial software (Comsol Multiphysics 5.5) was used to execute finite element method simulations of coupled gold nanoparticles on a quartz substrate. In reality, a couple tens of micrometres thick quartz layer was introduced to establish the antenna. However, only a 600 nm quartz base segment was investigated as field did not extend beyond that. The usage of *PML* borders defragments the mathematical prototype. Due to the existence of free electrons in the metal, the dielectric properties of the metallic surface has been computed using the Drude free electron model. In this model, the dielectric properties is derived using the relaxation period $\tau = 9.3 \pm 0.9 \times 10^{-15}$, and for metal at near-infrared frequencies when $\omega \gg 1\tau$, [65]:

$$\varepsilon(\omega) = 1 - \frac{\omega_p^2}{\omega^2} + j \frac{\omega_p^2}{\omega^3 \tau} = \varepsilon_{real}^f + j \varepsilon_{imag}^f \quad (5.1)$$

Here, ω_p is the plasma angular frequency equal to $\sqrt{\frac{4\pi N e^2}{m_0}} = 9$ eV, and N and $m_0 = 0.99 \pm 0.04$ are the conduction electron density and effective optical mass, respectively [65]. Figure 4.1 depicts an explanatory and simulation model interpretation of the paired nanostructures and their applications. In comparison to distributed nanoparticles in a liquid environment, this arrangement makes the entire system more resilient and easier to handle. A quartz substrate is both transparent and chemically inert over a wide range of frequencies. The quartz substrate has a computational thickness of 600 nm, and the height, h of the nanostructures is with respect to substrates. With wave excitement ON, a coupled metal antenna was stimulated by x -polarized light propagating in the z -direction from the top, and scattering boundary conditions (*SBC*) were established at the bottom and top of the computational

5.2 The Convergence of Machine Learning with Nanostructural Devices

region. The unit cell dimension of the quartz substrate kept consistent at $400 \times 200 \text{ nm}^2$, which is bordered by a perfect electric conductor (*PEC*) and a perfect magnetic conductor (*PMC*) along x and y walls, respectively, to impose the periodicity of the nanostructures. Throughout the numerical experiment, the height of the metal antenna was fixed to 40 nm [122]. Figure 5.1b depicts the variation of the electric field E_x in the x -direction through the core of the couple of nanoantenna computed using Comsol Multiphysics, and it illustrates an extremely enhanced electric field confinement in the separation area and the edges of the ellipsoidal and round antenna. Since electron propagation provides an appropriate electron confinement at the top of the paired device, the electric field in the separation gap area is significantly enhanced, as shown in Figure 5.1c. Figure 5.1c shows the maximum electric field intensities for $a = 100 \text{ nm}$, $b = 10 \text{ nm}$, $g = 10 \text{ nm}$, and $h = 40 \text{ nm}$, reaches up to 35,000 V/m at the interior edge of the coupled elliptical antenna, and the highest field intensity here is 97.14 % greater than the case of a circular antenna shown in Figure 5.1c. The electric field profile shows that for a coupled dimer, reducing the minor axis, b , results in a considerable field enhancement at the corners and edges. The *LSPR* is enhanced as a consequence of this interaction because the elliptical nanostructures interact intensely as they get nearer to one another. The change in the optical transmission/reflection and absorption spectra of the resonating wavelengths were smaller when the separation distance was greater, hence a narrower separation distance is recommended to obtain significant electric field enhancement [122].

Artificial Neural Network Modelling for Optimizing the Optical Parameters of Plasmonic Paired Nanostructures

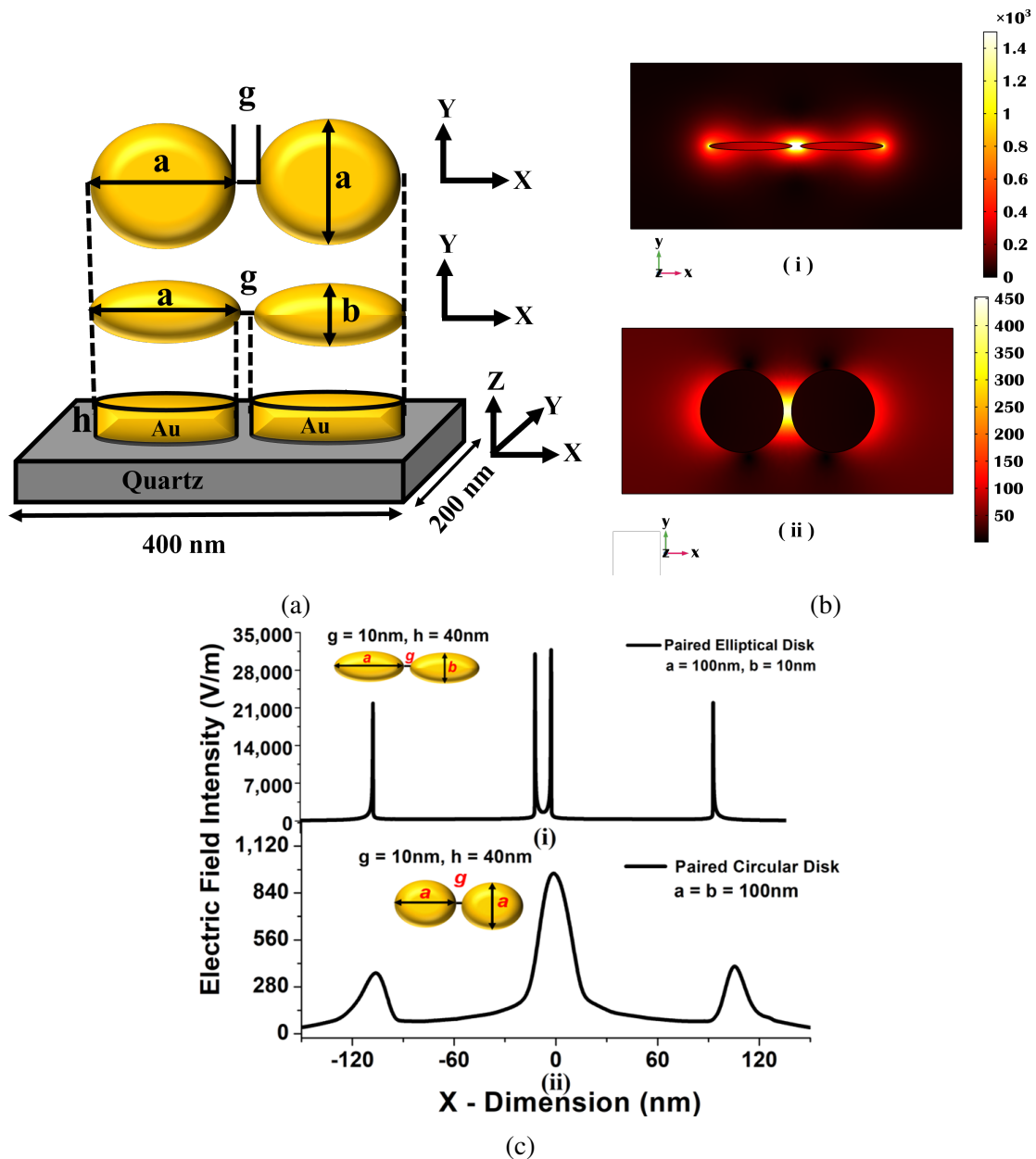


Fig. 5.1 (a) Schematic of circular and elliptical nanostructures placed on a quartz substrate (b) Mode profile E_x of paired gold (i) elliptical and (ii) circular nanoantennas (c) The line plot of the electric field confinement in the separation gap and at the corners of the nanoantennas.

Following the effective development of the mathematical simulations, this strategy has been used to vary the major axis a , minor axis b , and separation distance g of the nanostructures and quantify their commensurate sensitivity S , which is described as the rate of resonant

5.2 The Convergence of Machine Learning with Nanostructural Devices

wavelength (λ_{res}) variation with the change in the surrounding refractive index $\delta n_s(RIU)$, where $S = \delta\lambda_{res}(\text{nm})/\delta n_s(RIU)$. The sensitivity of a sensing element is the primary focus in its development, but the sharpness of the reflection and transmission patterns is also significant for their easy identification. The sharpness of the resonance curves is also affected by quantification precision, that can be directly measured by the *FWHM*, which itself is identified as the difference between the two wavelength values, i.e., $FWHM = \lambda_1 - \lambda_2$, where λ_1 and λ_2 are the wavelengths, when the response is half of its peak value. Furthermore, *FOM* has been regarded as the third crucial output variable, which was calculated as the ratio of the sensitivity to the *FWHM*, i.e., $FOM = S/FWHM(RIU^{-1})$, and the surface plasmon resonance wavelength has been recognised as the fourth output parameter because it indicates the highest comparative response amplitude at specific wavelengths [83, 122] to gather the range of dataset for neural network training. The nano-structured calculations were time-consuming and complicated. To address this limitation of conventional numerical simulations, the time-efficient *ML* method has been devised. We concentrated on the collection of input variables that can aid in neural network training. A large number of simulations have been carried out in order to obtain the sufficient dataset for neural network training. The input variables have been the major axis a , minor axis b , and separation distance g , while the outgoing variables were the sensitivity, *FWHM*, *FOM*, and plasmonic wavelength. Moreover, a neural network was created with the aid of a supervised learning algorithm to produce accurate predictions after learning from a training datasets. Here, Multi-layered perceptron (*MLP*) designs employed the back-propagation (*BP*) algorithm and multiple activation functions to construct multiple layers in feed-forward and back-propagation neural networks. In this work, we established an algorithm which can be employed for multi-input/output platforms and involves just a one-time training process that takes a few minutes to yield corresponding output values. As a result, this approach may be useful for a comparable nanoantenna development. Ultimately, this research exhibits forward modelling enabled by

Artificial Neural Network Modelling for Optimizing the Optical Parameters of Plasmonic Paired Nanostructures

neural networks, which has proved the *AI* algorithm's capacity to understand sophisticated correlations between nanophotonic structures and their associated optical outputs.

5.2.1 Artificial Neural Networks for Prediction of Output Parameters of Nanophotonic Structures

We live in a fascinating technological era in which ML has a substantial influence on a wide range of applications, from large data processing to producing precise predictions. Nevertheless, in the realm of ML, data gathering/collection might become a key issue. Data preprocessing, which includes data collecting, scrubbing, analysing, visualising, and extraction of features, consumes the preponderance of the time spent executing the ML algorithm from beginning to final moment. As a result, developing this *ML* algorithm becomes a critical endeavour. In addition, the outputs are depending on the improvements done by the proposed algorithm. Following the collection of the dataset, the created programme employs a number of data processing approaches. The generated task of the neural network training data is automated, with minimal or no user engagement. As a result, the significance of COMSOL Multiphysics data gathering cannot be overstated. *ML* plays an important role in facilitating the rapid analysis of vast amounts of data produced by nanostructures in order to identify meaningful insights for data scientists. Table 5.1 displays the variability of a data set or a sequence of integer data received from COMSOL multiphysics. As a result, the work of categorising data into multiple subcategories is completely automated. Table 5.1 shows the percentile, mean, standard deviation, lowest, and highest values for the generated data frame.

5.2 The Convergence of Machine Learning with Nanostructural Devices

Table 5.1 Dataset variation used for neural network training.

	Major Axis (nm)	Minor Axis (nm)	Gap (nm)	Sensitivity (nm/RIU)	FWHM (nm)	Plasmonic Wavelength (nm)
<i>count</i>	530	530	530	530	530	530
<i>mean</i>	89.69	49.54	39.5471	191.22	78.54	653.64
<i>Standard Deviation</i>	24.74	29.22	22.35	109.43	37.16	86.97
<i>Minima</i>	30.00	10.00	10.00	26.52	2.90	557.35
<i>Maxima</i>	130.00	130.00	80.00	595.04	202.40	1068.24

In Table 5.1, the dataset variation, and the relationships of the dataset along with its trends and patterns can be seen.

5.2.2 The Architecture of the Multilayer Artificial Neural Network

ANNs have indeed been presented as a powerful tool for assessing the relationship between the architecture and compositions of customizable nanophotonics structures and their operational qualities. It focuses on the development of computer algorithms that aid in the extraction of trends and the optimization of complicated data with a large number of factors. Forward ANNs are unique in that several layers and neurons may be employed to enhance performance. This artificial neural network was created using a computer with 8 GB of RAM, 128 GB of SSD storage, and the MacOS Big Sur (version 11.2.1 (20D74)) operating system. Throughout the calculation, the digital environment Jupyter Notebook (version 6.0.3) is employed, which is a web-based interactive computing notebook environment with Python (version 3.8.3) installed in an anaconda (version 1.7.2) environment. Even without special thumb rule, this

Artificial Neural Network Modelling for Optimizing the Optical Parameters of Plasmonic Paired Nanostructures

method can manage the complicated data hyperparameters derived from the basic input data. This was structured in three levels, as shown in Figure 5.2, including an input layer, an output layer, and hidden layers.

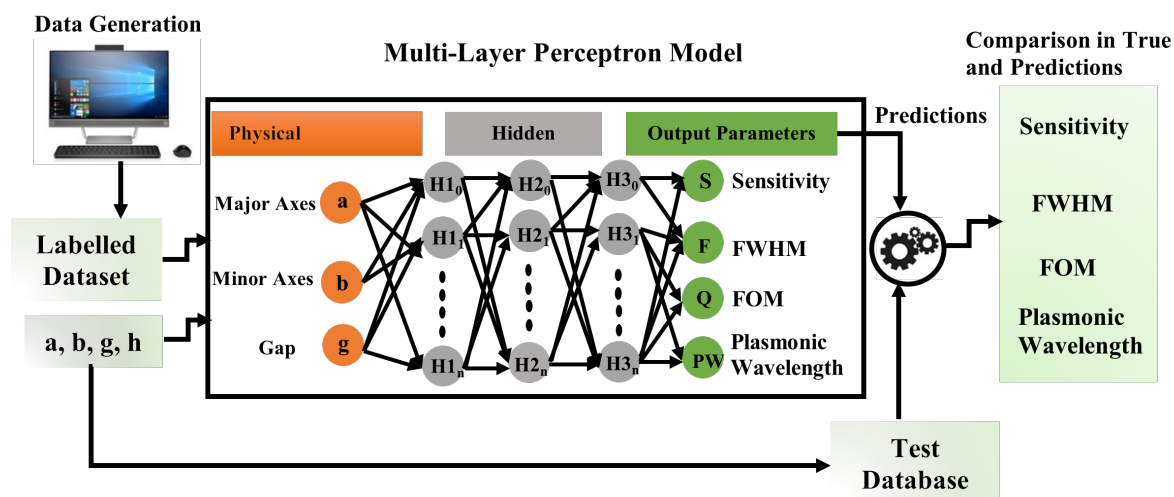


Fig. 5.2 Outlayer of Artificial Neural Network.

The input parameters to be processed are delivered to the completely integrated input layers. The output layer does the necessary tasks, such as prediction and classification. A neural network is made up of neurons which are arranged in layers (or nodes). Every neuron in one layer is linked to the neuron in the next layer by a weighted connection. The weight w_{ij} represents the frequency of the connection between the i_{th} neuron in one layer and the j_{th} neurons in the next layer. To produce the neurons' output, a functional weight is assigned to each neuron as an entry that is linearly aggregated (or summarised) and transmitted through an activation function. Finally, the anticipated output may be compared to the random test sets. The network may be represented as a black box that accepts m inputs and produces n outputs, as seen in Figure 5.2. An optimized ANN model with 5 hidden layers and 50 nodes/neurons within every layer was implemented all through this research, as shown in Figure. 5.2. These hidden layers were completely interlinked, which means that each node/neuron inside one layer is connected to the node/neuron in the next layer. To facilitate unbiased assessment while tuning the ANN model parameters, 10% of the datapoints were

5.2 The Convergence of Machine Learning with Nanostructural Devices

randomly chosen from the training dataset and assigned as the validation dataset (weights and biases). The Rectified linear unit *ReLU* activation function [123] and the Adam optimizer [124] were employed throughout the training method to depict the nonlinear function and improve the weights, respectively. The *ANN* model predicts certain outcomes after each iteration/epoch. The Mean Squared Errors (*MSE*) between both the predicted and actual outputs was calculated, and the back-propagation phenomena was employed to adjust the hidden layer weights for each epoch. The *MLP* computational system can have an infinite number of hidden layers between both the input and output layers; nevertheless, in this research, only a finite number of hidden layers were included, and data kept flowing forward from the input node to the destination node layer, similar to a feed-forward network in an *MLP*; however, the sensitivity, *FWHM*, *FOM*, and Plasmonic wavelength were considered outputs from the output layers. With the input variables of the artificial neural network are the major axis *a*, the minor axis *b*, and the separation gaps *g* have been mapped as the physical variables that are utilised for input layers, Figure 5.2 shows the flow of the entire procedure of the artificial neural network, where the first phase is to gather up the labelled dataset from the Comsol Multiphysics. Between the input and output layers, there are customisable hidden layers and neurons (or nodes) that anticipate output parameters that are similar to the real (or simulated) output. Neurons in the hidden layers plays a critical role in determining the neural network's overall performance. Despite the fact that these layers have no visible interface with the outside world, they have a substantial impact on the overall outcome.

The number of hidden layers and the number of neurons in each hidden layer are thoroughly researched based on mean squared errors (*MSE*) that can be calculated by using Equation 6.2:

$$MSE = \frac{1}{n} \sum_{i=1}^n (Y_i - Y_i^p)^2 \quad (5.2)$$

Artificial Neural Network Modelling for Optimizing the Optical Parameters of Plasmonic Paired Nanostructures

where n is the total number of data points used in the procedure. Y_i denotes the real value obtained by Comsol Multiphysics, whereas Y_{ip} denotes the expected quantities (e.g., from a linear regression fit). For each data point and the predicted regression model, the MSE can be calculated. The model is shown to be capable of making accurate predictions with the lowest MSE . The validation and training dataset's actual and projected data points are detailed in a subsequent section. These hidden layers can be used to break down a neural network's function into meaningful data computations. Each hidden layer is programmed to produce a certain result. The randomized weights are fine-tuned by altering the hidden layers (from 1 to 10) using 50 neurons and calculating the appropriate MSE , as illustrated in Figure 5.3a. The $MSE = 0.14$ at the initial epoch for 1 hidden layer is shown in red, and it drops steeply until 1500 epochs, when it stabilises for the subsequent epochs. The green curve, on the other hand, shows $MSE = 0.10$ for three hidden layers at the first epoch and stabilized after 700 epochs.

Consequently, the MSE s for 5 and 10 hidden layers are roughly 0.07 and 0.06 at the first epoch, respectively, and after 2000 epochs, it stabilized, as shown by the black and purple curves in Figure 5.3a. The MSE does not improve significantly when the hidden layers are larger than five; hence, five hidden layers were selected for additional investigations. Following that, the number of neurons in each of the five hidden layers was adjusted from 1 to 100, as illustrated in Figure 5.3b. When only one node is employed, the MSE is 0.25, as illustrated by the red curve. However, $MSE = 0.21$ was estimated for 5 nodes at the very first epoch, and the green curve shows that it stabilises after 1200 epochs. The $MSE = 0.15$ for 10 nodes at the first epoch is shown in black, and it remains stable after 800 epochs. The technique for 50 and 100 epochs was also investigated in order to lower MSE further, as demonstrated by purple and pink curves, respectively. Only a small variation in MSE was observed in these circumstances, and it became relatively steady after 600 epochs.

5.2 The Convergence of Machine Learning with Nanostructural Devices

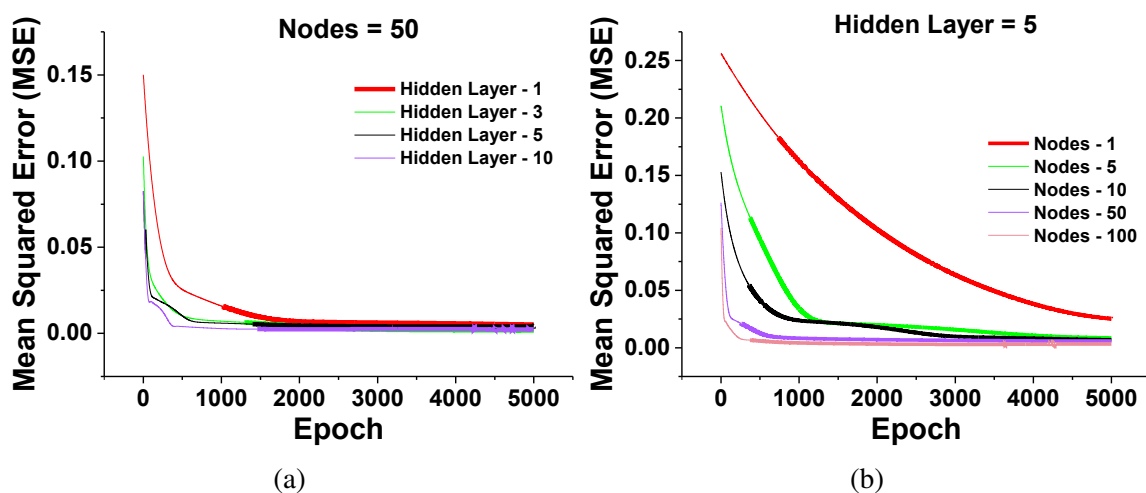


Fig. 5.3 Mean squared error calculation for the above shown dataset in Table. 5.1: (a) The mean squared error at different hidden layers with 50 nodes (neurons) (b) Neuron variation in hidden layers.

Lower the MSE , closer are the predicted regression values to the actual values, therefore the models with 5 hidden layers and 50 neurons appeared to be effectively trained, as illustrated in Figure 5.3b. This procedure was run for 5000 epochs to ensure that the MSE values dropped to their lowest level. Following this experiment, all subsequent calculations will use 5 hidden layers with 50 neurons to reduce the computational load. After this improvement, the neural network was designed using the rectified linear activation function (or $ReLU$), since it is convenient, straightforward to use, and effective in getting over the restrictions of other common activation functions like $Sigmoid$ and $Tanh$. It is less vulnerable and susceptible to vanishing gradient difficulties, that can render deep learning models exceedingly difficult to train. The Adam optimizer was preferred over $LBFSG$ and Stochastic Gradient Descent (SGD) optimizer to facilitate the weight values during the ML training phase since it maintains effectively for a decently large dataset. When MSE converges to an adequate threshold, the user selects the number of epochs to be collected. After modifying the model to obtain a steady MSE value, the necessary outcomes were presented as additional input data that was not provided during the training operation. The term "rectified network" refers to an artificial neural network with hidden layers that employs the rectifier function.

Artificial Neural Network Modelling for Optimizing the Optical Parameters of Plasmonic Paired Nanostructures

As the approaches that currently mandate the methodical creation of neural networks, *ReLU* implementation is without a doubt one of the main milestones in the deep learning revolution.

The quantity of data, the number of hidden layers, the number of neurons in each hidden layer, and the number of epochs all influence how long it requires to train an artificial neural network. When we utilised 5 hidden layers with 50 neurons in each layer and ran for 5000 epochs, it took roughly 10 seconds to train the proposed model with the *COMSOL* dataset. After the training was performed, the model weights and parameters were saved in the machine. The next stage was to use previously saved weights to estimate the output for unknown inputs, which took just 71 seconds for 5 hidden layers. Direct numerical simulation using *COMSOL* multiphysics, on the other hand, can take about 165 minutes, 235 minutes, and 636 minutes, for normal, fine and extremely fine meshes, respectively, and a day or two and can take much longer if a manual mesh (smaller to extremely fine mesh size) is being used to calculate the sensitivity, *FWHM*, *FOM*, and Plasmonic wavelength for only one design,

5.3 Neural Network Analysis with Empirical Evidences

The trained artificial neural network is assessed in this section by comparing predicted and real outputs for coupled nanoparticle having randomized design characterizations. Then after, for any of the major axis a , minor axis b , and separation gap g values, the anticipated sensitivities, *FWHM*, *FOM*, and Plasmonic wavelength are compared to their corresponding calculated values.

5.3.1 Sensitivity (nm/RIU)

The sensitivity [125] predictions has indeed been investigated in this subsection using *MSE* calculations for training and validation sets at various epochs. For the training and validation

5.3 Neural Network Analysis with Empirical Evidences

sets, the MSE was determined as almost 0.130 and 0.128, respectively which indicates that training has been sufficiently completed. Numerous additional and randomized datasets were used to see if the model made appropriate predictions when applied to real-world data. The data point location of the training, validation, and test sets are shown in Figure 5.4a. The red circle in Figure 5.4a denotes the training dataset that was utilized to train the neural network and forecasts the sensitivity parameters for arbitrary inputs. Furthermore, black circles indicate the validation dataset, that describes the prediction accuracy over real values, and green dots reflect the test dataset, which is completely different from the train and validation sets and is intended to assess prediction accuracy after training. The neural network is validated using this test dataset. Every circle defines a specific piece of information, and the numbers should indeed be oriented nearer to the solid black line in a well-trained model.

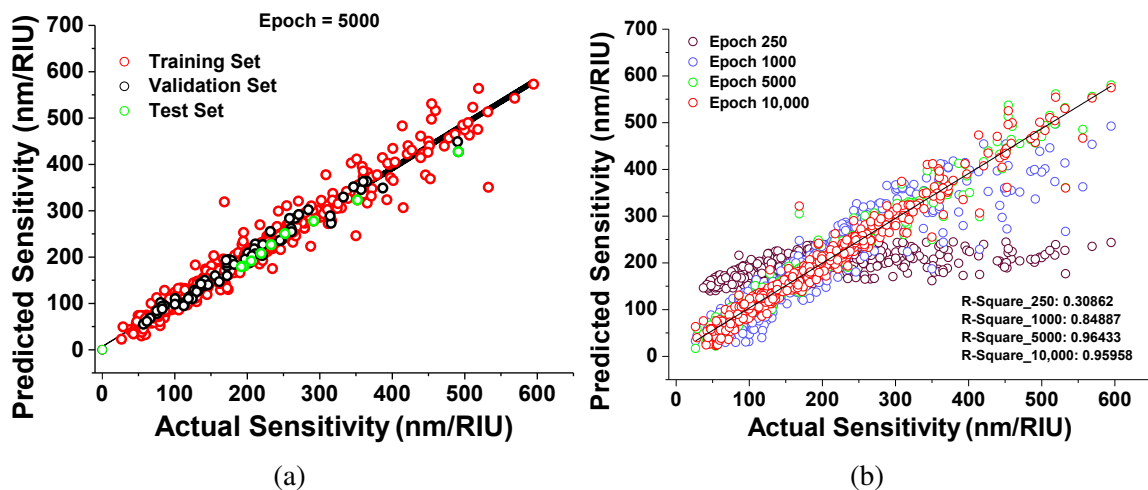


Fig. 5.4 The scatter plot of a data point location: (a) The comparison of the training, validation, and test data set (b) The efficiency of the developed neural network with epoch variance, with the comparison of actual sensitivity (nm/RIU) values (from the simulation) with respect to predicted values (calculated from the neural network).

The enhanced ML model with iteration (Epoch) is demonstrated in Figure 5.4b; this graph indicates the improvements in the planned neural network from 250 epochs to 10,000 epochs. The R-Squared values have also been determined to prevent overfitting. The projected sensitivity levels (shown by purple circles) at epoch 250 are not near to the true values (given

Artificial Neural Network Modelling for Optimizing the Optical Parameters of Plasmonic Paired Nanostructures

by the solid black curve). R-Squared scores for a mathematical fit were obtained, and the variation in predicted values was 0.31 for 250 epochs, demonstrating that the model had not been correctly trained. 1000 epochs were used to refine this established model, and the predictions were somewhat close the ideal curve, as illustrated by the blue circles. The 0.85 R-Squared value was calculated for 1000 epochs, demonstrating the improvements in neural network training predictions.

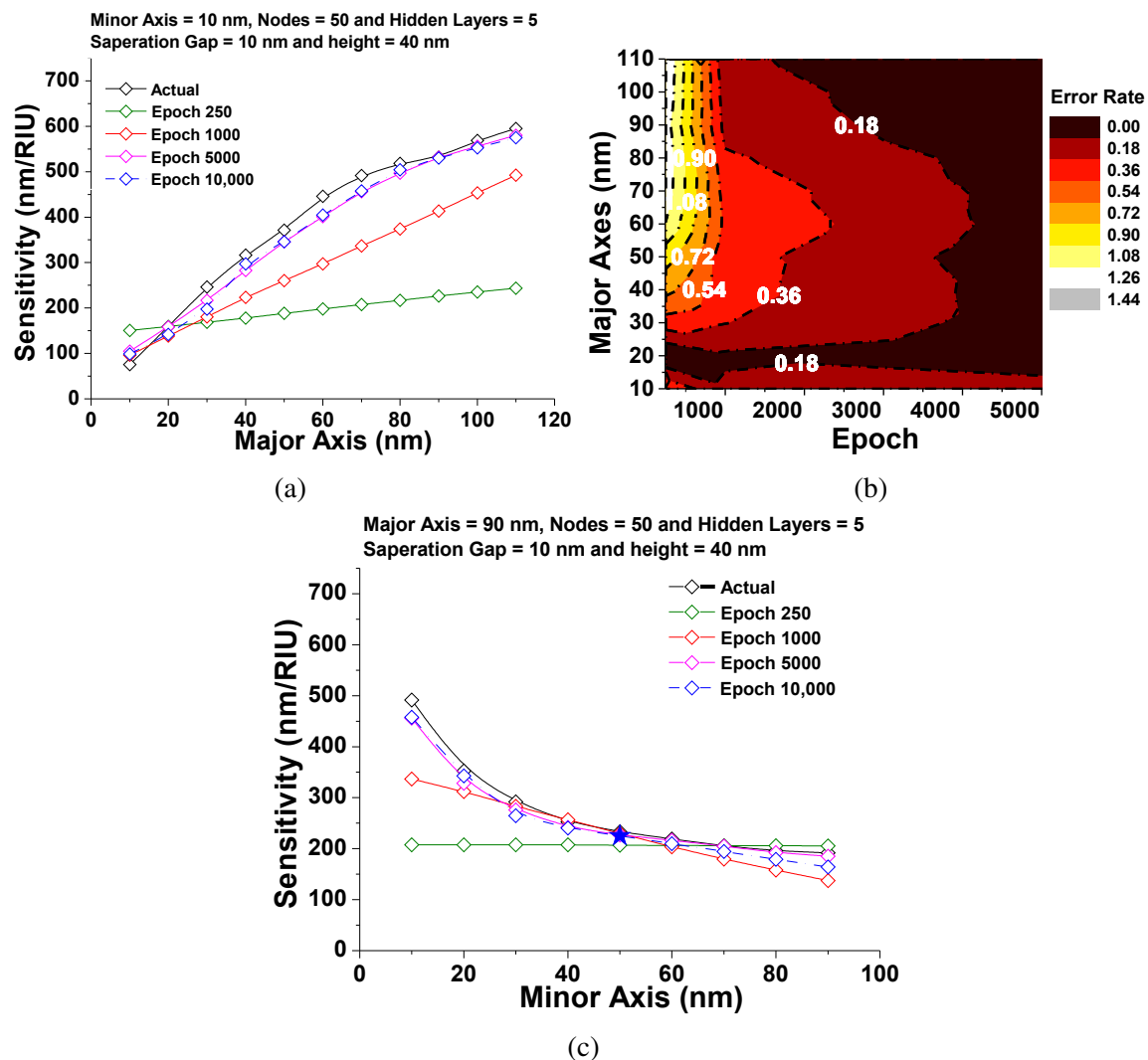


Fig. 5.5 Sensitivity visualization: (a) the predicted sensitivity over the major axes (nm) at different epochs (b) a contour plot of the absolute error values for sensitivity predictions over the major axes (nm) (c) the sensitivity response against the minor axes (nm) with epoch variation.

5.3 Neural Network Analysis with Empirical Evidences

We kept increasing the epochs until we got nearer to actual values, and the R-Squared values for epochs 5000 and 10,000 were determined as 0.964 and 0.959, respectively, as represented by green and red circles. The R-Squared value declined significantly at 5000, indicating that the model was being overfit, as seen in Figure. 5.4b. As a result, 5000 epochs have been considered for further analyses.

The modification in sensitivity with the major axis for various epoch values is shown in Figure 5.5a. The real dataset produced via COMSOL modelling is shown in black, and this dataset has been utilized as a reference dataset. We train the neural network in such a fashion that it can generate accurate predictions with regard to the reference data points by adjusting the period. The gap between the actual sensitivity (shown by black curve) and projected sensitivity (shown by green curve) is somewhat large at 250 epochs, as illustrated in Figure 5.5a. The disparity between both the expected sensitivity (represented by a red curve) and the actual sensitivity is minimised when the neural network is trained at 1000 epochs. The neural network was solved for 5000 and 10,000 epochs, respectively, to produce better projections over real sensitivities, as demonstrated by the pink and dashed blue curves. With a higher amount of epochs, the projected sensitivity is nearer to the actual sensitivity with no over-fitting in the model, as can be seen in these comparisons. Figure 5.5b illustrates a contoured graph of the projected sensitivity's error rate on a changeable major axis to optimise absolute error levels with varying epoch values. The error rate is steadily decreasing in this graph, with values of 1.90, 1.08, 0.72, 0.54, 0.36, and 0.18 for 500, 700, 1100, 1500, 2500, 3000, and 4500 epochs, respectively. The error decreases close to zero at 4500 epochs, which could be considered positive observations as shown in Figure 5.5b, so the trained model weights may then be retained for subsequent assessment at 5000 epoch. The sensitivity prediction across the minor axis from 10 nm to 120 nm is shown in Figure 5.5c. A black curve has been created in this image to represent the standard data points. The error rate between both the actual and anticipated sensitivity is steadily reducing as the epoch value

Artificial Neural Network Modelling for Optimizing the Optical Parameters of Plasmonic Paired Nanostructures

increases, as illustrated by the green, red, pink, and dashed blue curves with respect to the black curve. From 250 to 5000 epochs, the absolute error rate of sensitivity prediction is plotted along the minor axis. The error rate declines steadily from smaller to bigger epochs, with a value of 0.68 for 250 epochs; but, it drops to 0.51, 0.34, and 0.17 for 1000, 2000, and 4000 epochs, respectively, before reaching its minimum number for 5000. Because the absolute error rate is lowest at 5000 epochs, 5000 epochs have been optimised for further observations.

5.3.2 Plasmonic Wavelength

The wavelength of plasmonic resonance is critical to comprehending the efficiency of a nanostructured antenna. As a result, the reaction of the anticipated plasmonic wavelength (nm) (from the previously created neural network) to the actual plasmonic wavelength (derived from COMSOL multiphysics) has been investigated in this section. The *MSE* values of the neural network for the training and validation sets were estimated as 0.15 and 0.10, correspondingly. The *MSE* value of the neural network declines significantly from the first epoch to the 1000 epochs, reaching its minimum number for larger epoch values.

The improvements in the projected plasmonic wavelength with regard to the real plasmonic wavelength at epochs from 250 to 10,000 are shown in Figure 5.6. The linear regression fit is shown in black, and the plasmonic wavelength at 250 epochs is shown in purple hollow circles, that is not particularly close to the linear regression fit, indicating that the neural network is not correctly trained. As a result, the planned neural network was trained for 1000, 5000, and 10,000 epochs, as indicated by the blue, green, and red hollow circles, respectively. It is evident from this that as the epoch values increase, the projected values go closer to the linear regression fit. The R-Squared value has also been estimated as 0.188, 0.78, 0.99, and 0.98 for 250, 1000, 5000, and 10,000 epoch values, correspondingly, to prevent over-fitting in the neural network. It can be observed that R-Squared values slightly

5.3 Neural Network Analysis with Empirical Evidences

reduced with 10,000 epochs, indicating that projected quantities are approaching over-fitting, hence 5000 epochs are used for subsequent analyses.

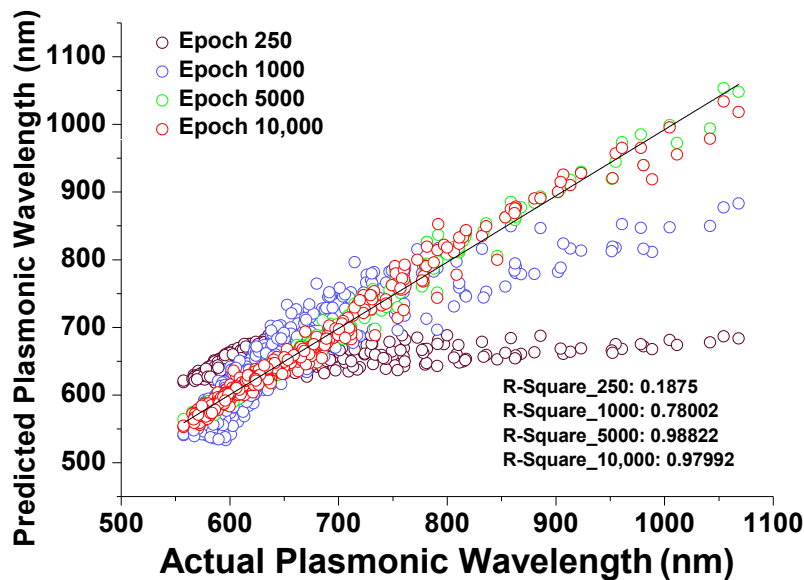


Fig. 5.6 The scatter plot of a data point location shows improvement on a developed neural network with different epochs.

The R-Squared value has also been estimated as 0.188, 0.78, 0.99, and 0.98 for 250, 1000, 5000, and 10,000 epoch values, correspondingly, to prevent over-fitting in the neural network. It can be observed that R-Squared values decline for 10,000 epochs, indicating that projected quantities are approaching over-fitting, hence 5000 epochs are used for subsequent analyses.

The enhancement in plasmonic wavelength predictions with regard to the major axis a is illustrated in Figure 5.7a, which would be analysed to the real (simulated by the finite element approach) plasmonic wavelength represented by a black curve. The predicted plasmonic wavelength for 250 epochs (presented by a green curve) is significantly a field from the validation curve (shown by a black line) in this figure, indicating that the neural network was not correctly trained. The predicted values then increased somewhat (indicated by the red curve) after 1000 epochs, approaching the validation curve. The neural network has been trained for higher epochs of 5000 and 10,000, as illustrated by pink and dashed blue curves, correspondingly, in order to produce accurate predictions, which have shown good

Artificial Neural Network Modelling for Optimizing the Optical Parameters of Plasmonic Paired Nanostructures

accuracy with regard to the validation curve. It is evident that as the number of epochs rises, the accuracy of the forecast improves. However, the absolute error values with respect to the major axis, a are 0.40, 0.34, 0.27, 0.20, 0.14, and 0.069 for 300, 570, 690, 1000, 2000, and 3000 epochs, correspondingly, from 250 to 5000 epochs. Following that, it is decreased to its smallest value at 5000 epochs; as a result, 5000 epochs have been used for all subsequent computations.

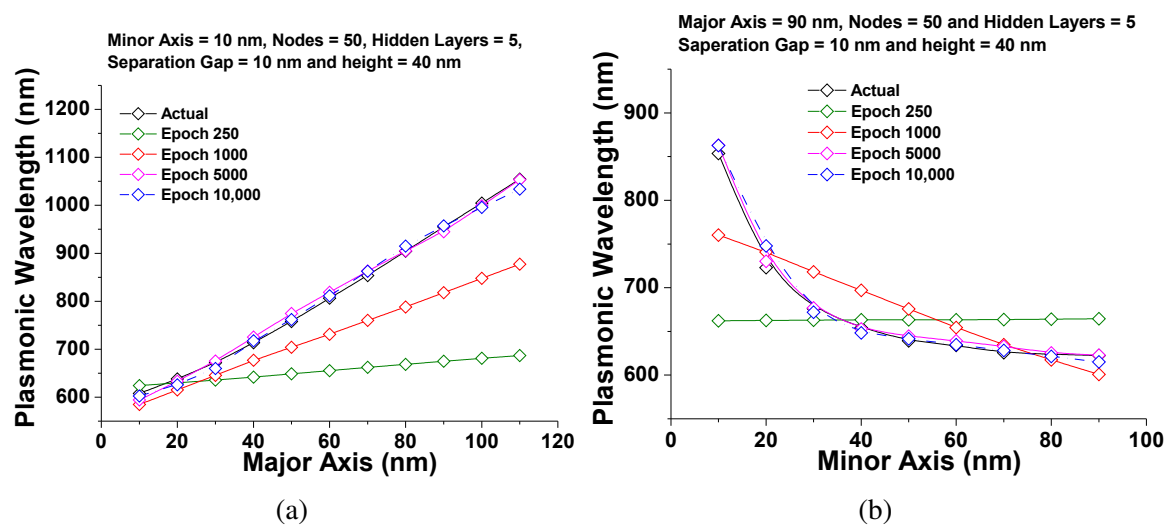


Fig. 5.7 Plasmonic wavelength (nm) visualization: (a) the predicted plasmonic wavelength (nm) with major axes (nm) variation at different epoch; (b) the plasmonic wavelength (nm) response against the minor axes (nm) with epoch variation.

The accuracy of the plasmonics wavelength predictions with regard to the minor axis b is shown in Figure 5.7b. The difference between both the actual (shown by a black curve) and predicted values was large for lower epoch values, and as the epoch increased, the accuracy of the predicted values continued to increase as well, as shown by green, red, pink, and dashed blue curves at 250, 1000, 5000, and 10,000 epochs, respectively. The absolute error values with various minor axes and epochs ranging from 250 to 5000 were also obtained to assess the neural network's efficiency. For the 900, 3000, 4000, and 4300 epochs, these values are 0.11, 0.073, 0.045, and 0.045, respectively. Finally, at the 5000th epoch, it dropped to its minimum value, which was utilised for all subsequent projections.

5.3 Neural Network Analysis with Empirical Evidences

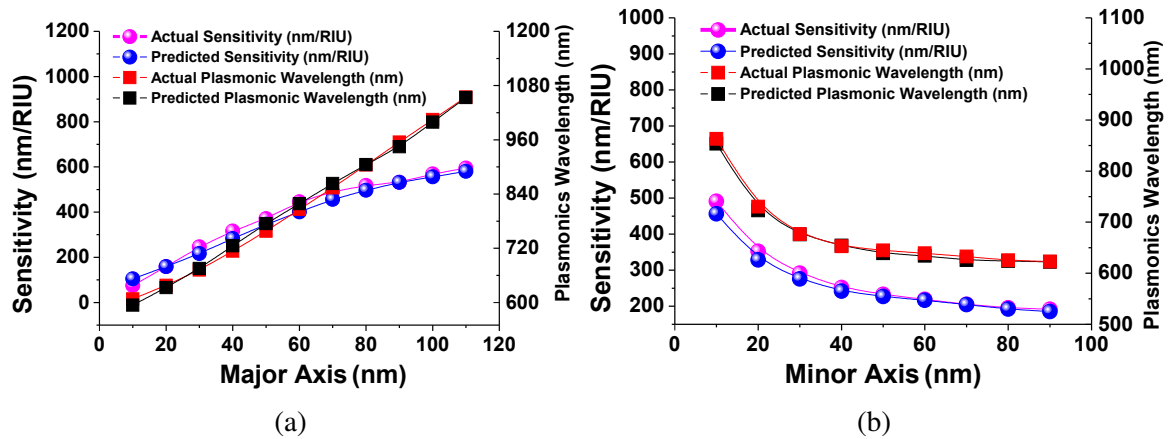


Fig. 5.8 Sensitivity (nm/RIU) and Plasmonic wavelength (nm) visualization: (a) show actual sensitivity (nm/RIU) and plasmonic wavelength (nm) response with predicted sensitivity (nm/RIU) and plasmonic wavelength (nm) over the major axis (nm) (b) the difference between actual predicted sensitivity (nm/RIU) and plasmonic wavelength (nm) and predicted sensitivity and (nm/RIU) plasmonic wavelength (nm) over the minor axis (nm).

Figure 5.8a depicts the variation of anticipated sensitivity (Left y-axis) and plasmonic wavelength (Right y-axis) with major axis, a (x -axis) after 5000 epochs. Using the Left y-axis, this figure depicts the fluctuation of sensitivity with the major axis represented by pink and blue curves for real values (acquired from COMSOL multiphysics) and anticipated values (predicted from the generated neural network). On the other end, using the Right y-axis, the variation of plasmonic wavelength with the major axis for the actual and expected values is represented by red and black curves, respectively, for 5000 epochs. The expected sensitivity (Left y-axis) and the plasmonics wavelength (Right y-axis) with regard to the minor axis at 5000 epochs are shown in Figure 5.8b. From this figure, it can be seen that the discrepancy between the actual and predicted values was quite small, implying that the constructed artificial neural network performs well within 65 seconds, whereas COMSOL takes between 5 to 6 hours. This implies that this network accurately and consistently predicts the value of sensitivity and plasmonics wavelengths with less processing time/load than conventional computational techniques.

5.3.3 Full-Width Half Maximum (FWHM)

The *FWHM* provides a significant part in observing the sharpness of the transmission spectra of the paired nanostructured sensors, thus the measurements of the *FWHM* predictions were also shown in this section from the above designed neural network. For the computation of *FWHM*(nm), the *MSE* values for the train and validation sets were 0.19 and 0.11, correspondingly, with a large reduction after 1000 epochs. Then, in order to boost the effectiveness of the constructed neural network, the accuracy of *FWHM* prediction was increased from 250 to 10,000 epochs. For 250, 1000, 5000, and 10,000 epochs, further computations were carried out, yielding R-Squared values of 0.72, 0.77, 0.846, and 0.845, correspondingly. Due to the reduction in R-Squared values for 10,000 epochs, 5000 epochs were instead utilised to optimise the full *FWHM* predictions.

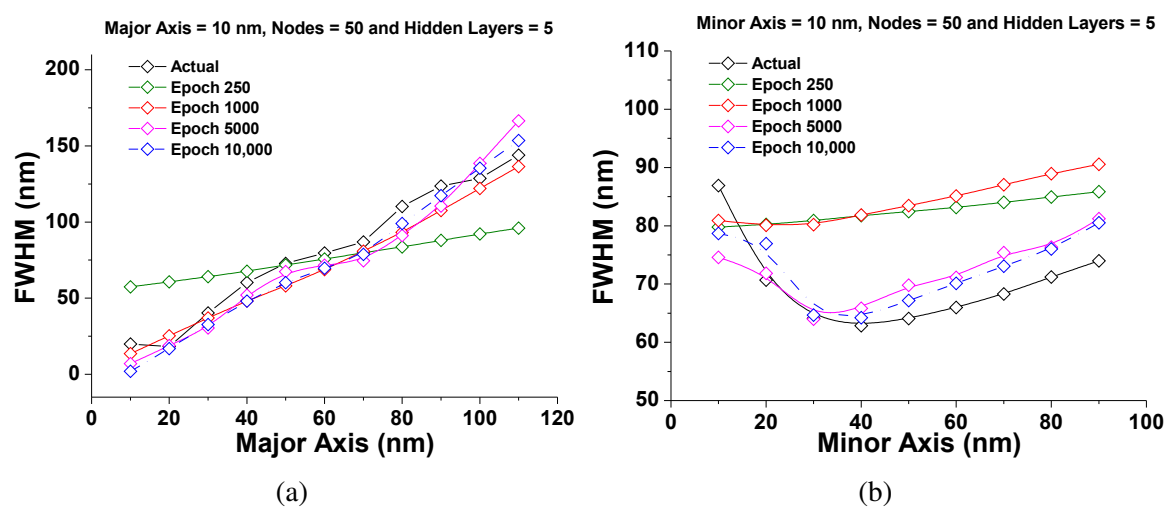


Fig. 5.9 FWHM (nm) visualization: (a) the predicted FWHM (nm) with major axes (nm) variation at different epochs (b) shows the FWHM (nm) response against the minor axes (nm) with epoch variation.

In addition, Figure 5.9a shows the variation of *FWHM* performance with the major axis. The reference data point acquired from COMSOL multiphysics is shown by a black curve. The green, red, pink, and dashed blue curves represent *FWHM* projections for 250, 1000, 5000, and 10,000 epochs, respectively; conversely, the actual *FWHM* is portrayed by a black

5.4 Comparison of Computational and Numerical Simulations Performance

curve. These graphs show that as the number of epochs is increased to the quality of the forecast improves until it reaches the over-fitting point, which in this case is 5000 epochs.

The error rate of the *FWHM* with the major axis in relation to epoch number decreases steadily as the epoch number increases. The relative error rates for the 530, 1000, 2100, 4000, 4900, and 5900 epochs were 0.61, 0.53, 0.35, 0.27, 0.18, and 0.091, respectively. The goal of calculating these values is to offer a numerical figure for the reduction in error rates. The projected *FWHM* for various epochs with regard to the minor axis is presented in Figure 5.9b, which is compared to the actual *FWHM* (shown by a black curve). The projected values converge with the true *FWHM* as the period increases, as seen by the green, red, pink, and dashed blue curves for epoch values 250, 1000, 5000, and 10,000, respectively. As the epoch number is raised, the error rate for the *FWHM* with the minor axes is similarly seen to be continuously reducing as shown in Figure 5.9b. As the epoch number is raised, the error rate decreases, with values of 0.2, 0.1, 0.06, and 0.03 for 3000, 3800, 5000, and 8000 epochs, respectively.

5.4 Comparison of Computational and Numerical Simulations Performance

COMSOL Multiphysics software based on the finite element methodology (*FEM*) has been utilized to generate the optical transmission/reflection spectra and field distributions for the coupled nano-structured antennas. The neural network, which has been mentioned in the previous part, was created in Python to make predictions. This created neural network model produced predictions on the related outputs in a few seconds using randomized input variables. Nevertheless, to study a particular variable by directly using COMSOL Multiphysics might require a long and tedious time. Finally, we estimated the sensitivity, *FWHM*, and Plasmonic wavelength for randomized major axis, minor axis, and separation

Artificial Neural Network Modelling for Optimizing the Optical Parameters of Plasmonic Paired Nanostructures

gap, as well as their corresponding sensitivity, *FWHM*, and Plasmonic wavelength, within the range (provided dataset), as shown in Table. 5.2. The absolute error rate in % between both the predicted and simulated sensitivities for the randomized dataset is also provided. The estimated relative error parameters were obtained to be between 3.39% and 0.02%, demonstrating that it is an excellent response for an algorithm built in-house for generating relatively accurate predictions.

Table 5.2 Comparison between actual and predicted values within the range.

Input Parameters		Simulated Data from COMSOL Multiphysics					Predicted Data from Artificial Neural Network				Abs Error
Major Axis (nm)	Minor Axis (nm)	Gap (nm)	Sensitivity (nm/RIU)	FWHM (nm)	FOM	Plasmonic Wavelength (nm)	Sensitivity (nm)	FWHM (nm)	FOM	Plasmonic Wavelength (nm)	Sensitivity (nm/RIU)
											%
60	20	40	147.2138	47.5796	12.9362	615.5012	146.9226	48.2208	12.7551	614.5826	0.19
80	30	80	163.8554	70.5513	8.8533	624.6127	163.6056	73.3072	8.5141	624.1441	0.15
85	45	25	171.4485	40.5550	17.8535	724.0533	170.1578	45.2992	16.0795	728.3898	0.75
90	50	90	135.1549	72.3698	8.4007	607.9604	135.6321	76.1116	7.9741	606.9173	0.35
100	40	60	197.3106	67.2607	9.5097	639.6299	196.4355	66.1773	9.6454	638.3086	0.44
100	40	50	208.2831	69.2660	9.2666	641.8674	208.2168	70.5940	9.0697	640.2649	0.03
100	50	90	170.0086	79.0452	7.8709	622.1600	171.1509	82.6979	7.5360	623.2143	0.67
110	50	110	193.4595	90.4005	7.1131	643.0292	194.6961	92.8461	6.9959	649.5304	0.64
115	25	25	307.8743	100.8810	7.7953	786.4027	307.7973	100.0813	7.8181	782.4466	0.02
120	60	90	202.0654	125.9891	5.1380	647.3321	202.4991	118.7540	5.4480	646.9770	0.21
120	50	110	231.9397	105.6556	6.3215	667.9105	224.0618	105.1861	6.3483	667.7588	3.39
120	60	120	208.3476	105.9363	6.1832	655.0344	208.6262	104.3657	6.2874	656.1949	0.13

In addition, as shown in Table 5.3, we have shown the performance of the proposed neural network outside of the training dataset. Here the trained code was checked within the range, a comparison of actual and predicted values is performed. Comparing the actual data values and the predicted data points, the absolute error rate was determined. The ANN has the particular advantage of being able to calculate optical parameters in a very short period of time with

very reduced computer resources. Another benefit of the created ANN is that it involves minimal sophisticated statistical training and can detect complex non-linear connections between dependent and independent variables with no explicit training. This investigation, in contrast to conventional regression analysis [126], demonstrates the ability to identify all potential interactions between predictor variables and provides multiple input training. Conventional regression analysis requires substantial statistical expertise and knowledge of a variety of statistical concepts, including backward and forward stepwise regression, p values, odds ratios, multi - collinearity, correlations, and input - output parameters.

Table 5.3 Comparison between actual and predicted values outside the range.

Input Parameters		Simulated Data from COMSOL Multiphysics					Predicted Data from Artificial Neural Network				Abs Error
<i>Major Axis</i> (nm)	<i>Minor Axis</i> (nm)	<i>Gap</i> (nm)	<i>Sensitivity</i> (nm/RIU)	<i>FWHM</i> (nm)	<i>FOM</i>	<i>Plasmonic Wavelength</i> (nm)	<i>Sensitivity</i> (nm)	<i>FWHM</i> (nm)	<i>FOM</i>	<i>Plasmonic Wavelength</i> (nm)	<i>Sensitivity</i> (nm/RIU) %
135	35	65	293.7393	137.3619	5.5150	757.5516	298.9795	161.6434	4.6454	750.9131	1.78
145	25	30	368.6747	214.8370	3.8776	833.0679	361.9376	187.1250	4.5343	848.4839	1.82
155	55	35	302.0654	194.7975	3.8421	748.4509	285.3999	195.8552	3.7381	732.1369	5.51
165	65	45	328.0120	208.4629	3.6274	756.1962	298.4219	210.7488	3.7008	779.9491	9.02
165	85	55	296.2564	225.6050	3.2763	739.1566	271.6019	216.4422	3.5380	765.7940	8.32

5.5 Summary

Finally, machine learning method was developed and utilised to predict the key features of a coupled gold nanoantenna for a combination of input/output parameters. This study illustrates how to evaluate an artificial neural network rigorously and how to make excellent predictions using a trained network. Five hidden layers of 50 neurons were employed all through the neural network to accomplish rapid resolution and good precision in estimating outputs for unpredictable input geometric parameters of the nanoantenna. The *MSE* has also been tested against the number of epochs when predicting sensitivity, *FWHM*, *FOM*, and

Artificial Neural Network Modelling for Optimizing the Optical Parameters of Plasmonic Paired Nanostructures

plasmonic wavelength about any random input variables of various major axis, minor axis, and separation gap for any arbitrary input variables of distinctive major axis, minor axis, and separation gap. This research also offers a comparison between COMSOL Multiphysics and in-house created neural networks in terms of computing time, which is nearly five times faster than conventional simulations. Finally, the created model's performance was proven for the randomized input parameter and the associated output parameters were predicted. As a result, we predict that the coming together of artificial intelligence and nanotechnology will pave the way for a plethora of new technical breakthroughs in the field of knowledge sciences.

Chapter 6

Deep learning for spectral prediction and prospective validation of nanostructured dimers

6.1 Introduction

In recent years, many advances in optics have resulted in remarkable capabilities beyond the diffraction limit with various applications in the field of biomedicine, point-of-care applications, and nanotechnology. Nanophotonics has transformed traditional optics by allowing subwavelength structures to influence light-matter interactions [127–129]. Nanophotonics strives to use optical resonances and strong surface plasmon localized fields produced by either nanoparticle shape or selection of materials [130–133]. Complex nanostructures, on the other hand, whose shapes may be characterized by several geometrical factors, usually necessitate the use of advanced numerical techniques to deal with multidimensional matrix organizations deodorised from integral or differential versions of the Maxwell's equations. There are different numerical techniques are available to solve such complex structures based on the finite element methods [134] named COMSOL Multiphysics numerical packages

Deep learning for spectral prediction and prospective validation of nanostructured dimers

[135], the generalized method of moments (*GMM*) [136], and finite difference time domain method [137, 138], as well as the discontinuous Galerkin method [139–141]. Regrettably, simulations employing these tools are often quite time-taking and computationally costly, nonetheless, in scenarios requiring a real-time application, such as biosensors [142, 143], particle physics [144], condensed matter [145], chemical physics [146], ultra-cold science [147], conventional microscopy [148, 149] iterative inverse designs of complex optical devices [150, 151] and investigation of optical functionalization [152], efficient modelling of optical performance at the nano/micro region is greatly sought. To overcome this shortcoming, deep learning (DL) techniques [153] such as multilayer perceptron neural networks (*MLPs*) [154], convolutional neural networks (*CNNs*) [155], recurrent neural networks (*RNNs*) [156], and generative adversarial networks (*GANs*) [157], the predictive modelling play a vital role based on physics has advanced dramatically in the realm of cognitive science [38]. As a result, several researchers have increasingly turned their attention to DL and have applied in synchronous transceivers that are one example of these kind of applications [41], plasmonics [42, 43], multimode fibres [44], sensing [45, 47–49], nanotechnology [51, 110, 53–55] and photonic crystal fibre [50]. Nanophotonics is an outstanding example of surface plasmon resonance and intensely confined electromagnetic fields that may be tuned for diverse purposes by modifying the nanoparticle shape and material choices. The overall tendency of this study findings so far is that a neural network must be developed for a fast computational process and less computing load that involves hyper-parameter tuning, training data production, training, and rigorous testing for each unique problem adopting a specific geometric model.

6.2 Deep Learning (DL) paradigm and its synchronizations with nanotechnology

This work has been organised in two phases where in first, we have developed a FEM-based frequency domain approach [19, 20, 12, 21, 22, 9] which was utilized to obtain the surface plasmon resonance confinement around the gold nanostructures. Figure 6.1. shows an overview of the model description, where gold elliptical and circular dimmers have been designed. The dielectric constant of the gold have been adopted from [65].

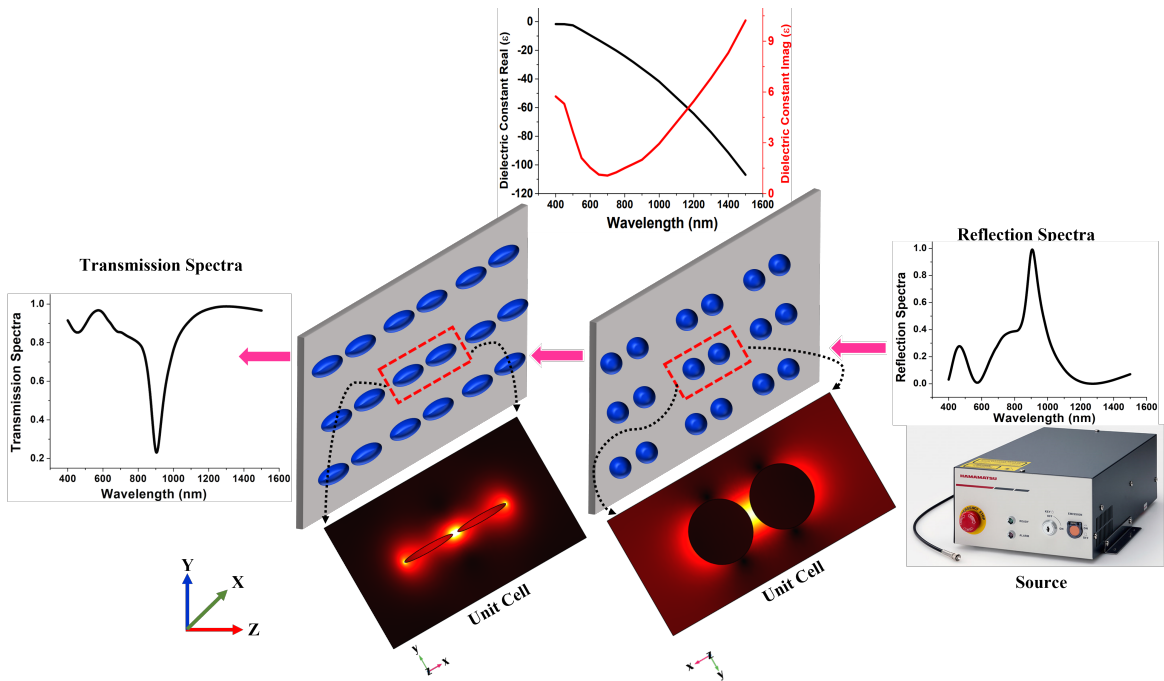


Fig. 6.1 Schematic of the extended unit cell elliptical and circular nano antenna and its optical response in terms of transmitted and reflection spectra.

The classical Maxwell equations were solved by employing the *FEM*, taking into account the harmonic dependency of the electric field $\mathbf{E}(r,t) = \mathbf{E}(r)e^{-j\omega t}$ in order to examine the physical plasmonic characteristics of nanostructures. Throughout the simulation, the Helmholtz equation has been employed, which can be obtained from the usual Maxwell

Deep learning for spectral prediction and prospective validation of nanostructured dimers

equations, as shown below.

$$\nabla^2 E + k_0^2 \epsilon E = 0 \quad (6.1)$$

Here, k_0 is wave vector. Temporal periodic disseminating field was used as $E(x, y, z) = E(x, y, z)e^{j\beta z}$, and β is defined as a propagation constant. In complex form, $\gamma = \alpha + j\beta$, and if $\alpha = 0$, then $\gamma = j\beta$, which represents the propagation dependency in the z -direction. To excite the nanostructures, the x -polarised wave is launched from the top layer in the z -direction which generated the *LSPR* upon interaction with the designed nanostructures. The strongly localized LSPRs and its optical responses (for elliptical and circular dimers) has also been shown the in inset of Figure 6.1. For more details please see Chapter 4. From that it is clearly identified that the frequency response is sensitive to geometrical parameters of any nanostructure, materials characteristics, and changes in the local environment, LSPRs have huge potential for molecular sensing, which could help with clinical diagnosis, environmental monitoring, and detection of biological agents [158–160]. The analyte molecules are typically attached to the exterior face of the nanostructures, either along with or without tethering particles. It generates a minor perturbation of the dielectric surrounding refractive index (*RI*), resulting in a measurable shift in the resonance frequencies or amplitude, which may be evaluated instantaneously using the transmission, reflectance and absorption spectra which can be predicted with the help of designed DL neural network configuration as shown in Figure 6.2.

6.2 Deep Learning (DL) paradigm and its synchronizations with nanotechnology

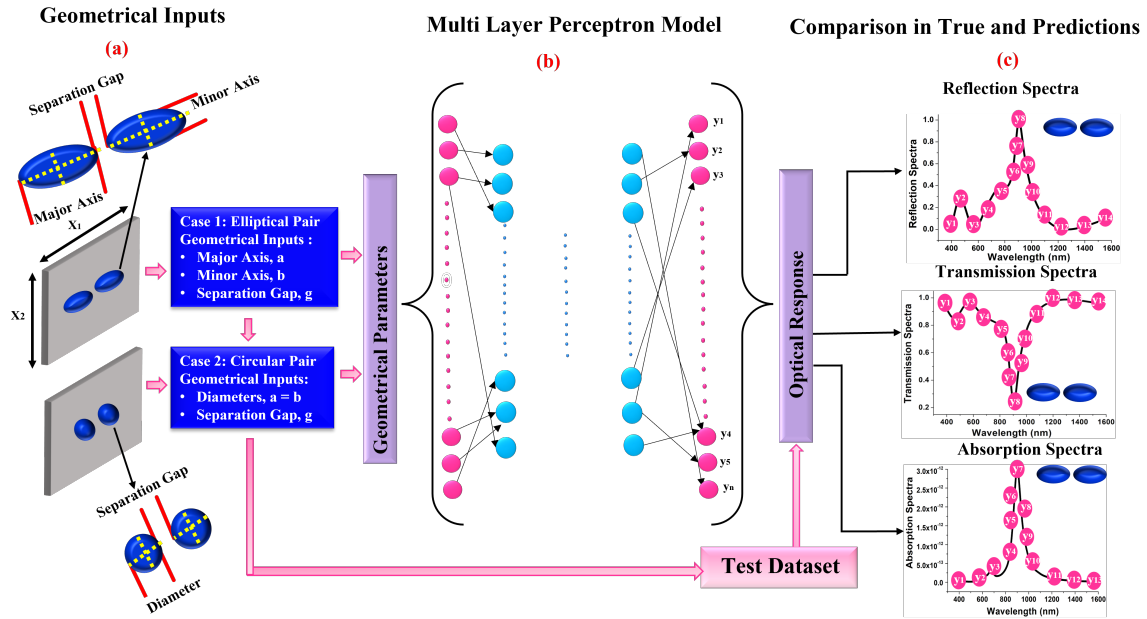


Fig. 6.2 Schematic of the structure of two elliptical and circular nanostructures on SiO_2 substrate (The top and front views of a single unit cell with the geometrical parameters are represented in the insets). (b) A DL neural network model that predicts the optical response over a wavelength range for the given geometrical parameters (c) Shows the predicted optical response for a given geometrical structure.

Here, Figure 6.2a shows the given geometrical inputs (paired elliptical and circular dimers) to the DL neural network. Surface lattice resonances (SLRs) are made up of gold nanostructures organised in a regular pattern. It can sustain resonances that are formed via LSPRs coupling and have much finer spectral characteristics [161]. A gold nanostructure supports plasmonic resonances on a SiO_2 substrate in each unit of the structure. The geometric properties of the nanoparticles [162], which may be mapped to the major (a) and minor (b) axes, diameter (d) of circular dimer, separation distance (g) and height (h) of the nanostructures, influence the wavelengths at which SLRs are triggered. Variation in these factors can change the optical spectral values. Thus, the major (a) and minor (b) axes, diameter (d), height (h) are adopted as input parameters, and the corresponding outputs are discrete spectral datapoints. Figure 6.2b shows the brief architecture of the developed neural network when the input parameters are remitted for predicting the spectral response

Deep learning for spectral prediction and prospective validation of nanostructured dimers

of the corresponding nano structures. To begin training the developed DL neural network, the learning algorithm develops an estimated function that expects output values. After adequate training, this built model is expected to produce output spectral responses utilising any new geometrical dimensional values. This process of learning will determine the mean squared errors (*MSE*) to demonstrate the efficacy of the proposed *DL* neural network by comparing its anticipated spectral output with the actual spectral values. Many widely used machine learning packages were exploited to develop and train this DL neural network, including *pandas* [113] for data preprocessing and *Scikit-learn* [114] for intensive training. *NumPy* [115] for matrices and multidimensional arrays, and *pickle* [116] for compiling and deserializing a *Python* object hierarchy are all elevated libraries used for developing regression model. Subsequently, *Pytorch* [117], a *DL* framework centred on Torch tensors, was employed. It's a commercial and free licence project created in AI Research lab organized by Facebook (*FAIR*) [120] in 2016 and entrenched on the scripting language *Lua* [121], that is identical to *NumPy* with *GPU* integration. This is a crucial method since it assists in the acceleration of numerical computations, which may strengthen the performance of the *DL* neural network up to 60 times. It has a concise *API*, making it simple to integrate with *Python*. The usage of this excellent platform is attributable to the fact that it provides for the creation of rapid computational features that can be updated in real-time, which is necessary throughout DL neural network training process. Designers used *FEM* solvers in the tail end for dataset collection, which is useful to train the *DL* neural network, and *Pytorch* and *Scikit-learn* in the front end due to their remarkable compelling architectural style, which facilitates rapid and lanky approaches, even though *PyTorch* employs several backend instead of a single backend for *GPUs* and *CPUs* as well as other operational aspects. While designing this algorithm, *Adam Optimizer* has been used which is one of the most widely used in *DL* neural network training algorithms nowadays. Following Adam's approach, it was widely assumed that Adam converges faster than vanilla Stochastic Gradient Descent (*SGD*) and

6.3 Architectural framework of *DL* neural network with Empirical attestation

Stochastic Gradient Descent (*SGD*) with momentum, but that it generalises poorly. The relative insensitivity to hyper-parameters and short time frame performance in training are therefore considered to be Adam's strengths over *SGD*. Researchers have created a metric of "tunability" and confirmed that *Adam Optimizer* is the most adjustable for most of the challenges they have investigated. Hence, by using this designed *DL* neural network, this identification gives researchers the encouragement to discern optical spectral response for paired nanostructural devices.

6.3 Architectural framework of *DL* neural network with Empirical attestation

DL neural network have indeed been established as a powerful tool for deciphering the correlation in between the architecture and re-configurable nanophotonic structure composition and its functionality. It involves the construction of computer algorithms that aid in the extraction of motifs and the optimization of complicated information with a large number of variables. Forward *ANNs* are remarkable in that they may leverage numerous layers and *neurons* to efficiently operate. This neural network is formed using a cognitive computer with 8 GB RAM, 500 GB Harddrive, with the windows operating system (version 20H2 Semi-Annual Channel) installed. Throughout the calculation, the virtual environment Spyder python (version 5.1.5) is installed in anaconda (version 1.7.2). This *DL* neural network was arranged in three levels, as shown in Figure 6.2b, including an input, output and *hidden layers*. The input parameters that must be interpreted are delivered to the fully linked input layers. Prediction and categorization are among the tasks that the output layer does. A layer-by-layer assembling of *neurons* makes up a neural network. Every *neuron* in single layer is interconnected to the *neurons* in the following layers via a weighted connection. The frequency of the relation between the j_{th} *neuron* in one layer and i_{th} *neuron* is represented by

Deep learning for spectral prediction and prospective validation of nanostructured dimers

the weight w_{ij} . Each *neuron* is given a function weight, which is then linearly aggregated (or summed) and transmitted with the help of an activation function to produce the output from *neurons*. Finally, the anticipated output data may be compared to the random test data points. The designed *DL* neural network can be visualised as a locked box that accepts x input and generates y outputs [163] (see Figure 6.2b). As shown in Figure 6.2, an optimal *DL* neural network with optimized *hidden layers* = 5, *neurons* = 50 in each layer was implemented throughout this investigation. Every *neuron* inside each layer was interconnected to the *neurons* in the subsequent layer, implying that these concealed levels were totally integrated. 20% of datapoints were randomly selected from the training datapoints and supplied as the evaluation datapoints to provide impartial evaluation while tweaking the *DL* neural network hyperparameters (weights and biases).

6.4 Results and Discussion

In this work, the geometrical range (a , b , d and g) of the nanostructure were varied from 10 nm to 130 nm; however, h was fixed at 40 nm. The granularity of gathered dataset is chosen to minimise computing costs while yet allowing the *DL* neural network to be trained properly. The complete datasets throughout this investigation comprise 10,500 parameter combinations and their accompanying spectra. We exclusively selected structural factors that have a considerable influence on the spectral properties and cover all conceivable spectrum variants. Indeed, with this subsequent quantity of training data, *DL* neural network can be trained to accurately model and forecast millions of spectral properties of the plasmonic structures in the parametric range. Datasets are divided into three groups throughout the training process of training dataset, validation dataset, and test dataset shown in Figure. 6.3

Training dataset are provided to the *DL* neural network to optimise the algorithm by revising weights whereas validation dataset are used to evaluate the *DL* neural network, acting as a verification of the training response and supporting to determine if the network

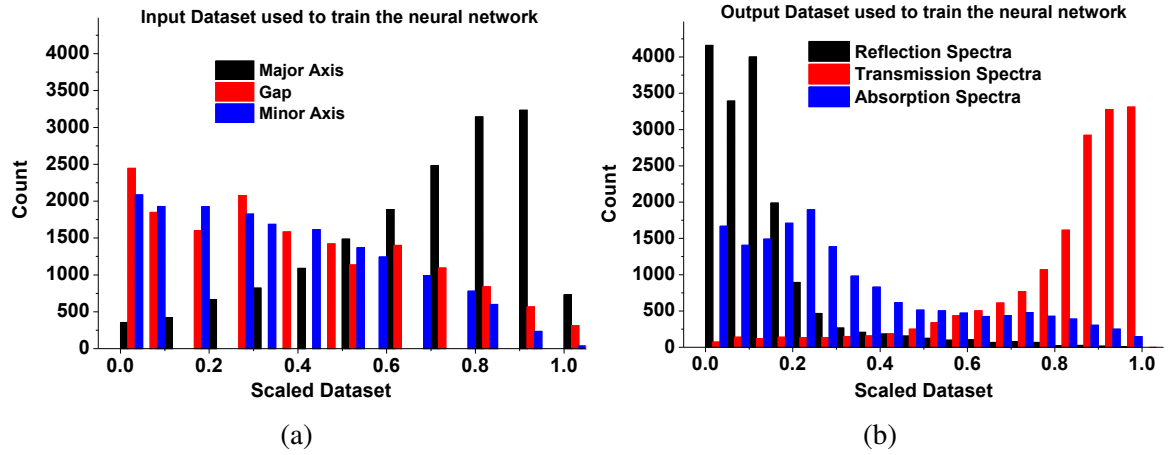


Fig. 6.3 Histogram of the Input and Output datasets for elliptical and Circular paired nano structure. (a) Shows the scaled input (Major, Minor Axis and Separation Distance) dataset used to train the neural network. (b) Shows the trend of the Output (Reflection, Transmission and Absorption Spectra) dataset used to train the developed neural network

is overfitting; and test dataset are used to assess the predictive performance. Every time, the ideal *DL* neural network is determined by selecting suitable hyperparameters depending on the training performance. The performance improvement of the *DL* neural network are thoroughly investigated in terms of *MSEs* that have been calculated for each *hidden layers* when the *epoch* = 5000 and *neurons* = 50. For *MSEs* calculation following Eq. 6.2 has been used.

$$MSEs = \frac{1}{n} \sum_{i=1}^n (Z_i^a - Z_i^p)^2 \quad (6.2)$$

Where, n is the total number of datasets utilised throughout the training process. Z_i^a is the original data points calculated from Comsol Multiphysics, Z_i^p is the predictions over the actual dataset. The calculated *MSEs* of the predicted datapoints from the developed network compared to the targeted datapoints are quantified by *MSEs*, which itself is regarded the most effective assessment criterion. It is also used as the validation criteria of the *DL* neural

Deep learning for spectral prediction and prospective validation of nanostructured dimers

network. Hence, the comparison of the $MSEs$ calculation at each *hidden layers* are shown in Figure 6.4 when $neurons = 50$ and $epoch = 5000$.

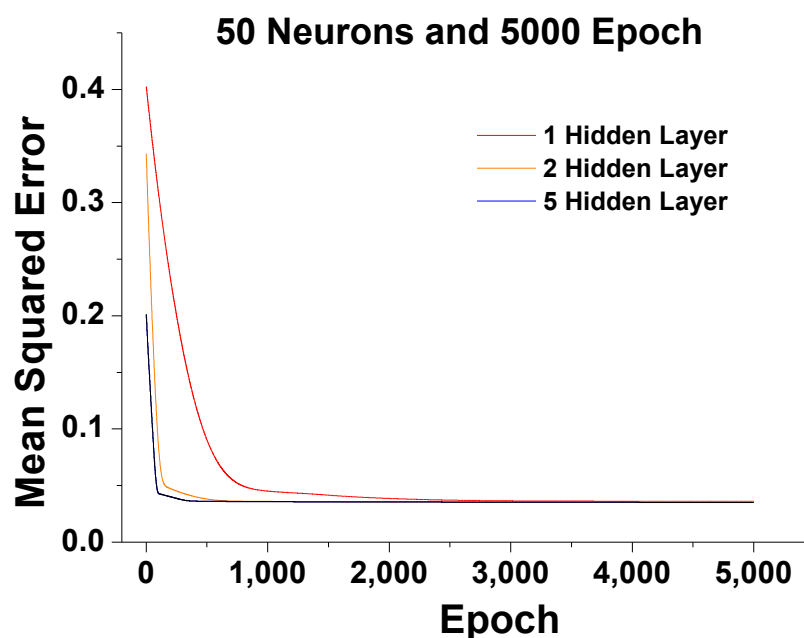


Fig. 6.4 Shows the $MSEs$ values for 1, 3 and 5 *hidden layers* when $neurons = 50$ and $epoch = 5000$.

Figure 6.4. shows that the values of $MSEs$ for *hidden layers* = 1, 3 and 5 when $neurons = 50$ and $epoch = 5000$. Here, the red curve shows the $MSEs$ values = 0.4 at $epoch = 1$ for *hidden layers* = 1, and $neurons = 50$ which rapidly decreases until $epoch = 2000$, and then almost constant for $epoch \geq 2000$. However, the orange curve shows the $MSEs$ values = 0.35 at $epoch = 1$ for *hidden layers* = 2, $neurons = 50$, and it quickly stabilized after $epoch \geq 500$. On the other hand, for $epoch = 1$, $MSEs$ values = 0.2 has been shown by a blue curve when the *hidden layers* = 5, $neurons = 50$. The $MSEs$ values fall significantly at *hidden layers* = 5, and in this context, it can be stated that the constructed neural network produces the appropriate approximation when the hyper-parameters are adequately configured.

For selecting the best hyper-parameters in terms of performance of the DL neural network, the *hidden layers* are optimized in first stage when the number of $epoch$ and $neurons$ were fixed at 5000 and 50. The initial prediction have been made for the given input geometrical

6.4 Results and Discussion

dimensions as $a = 70$ nm, $b = 10$ nm, and $g = 10$ nm and the corresponding predicted transmission, reflection and absorption spectra shown in Figure 6.5 for $hidden\ layers = 1$.

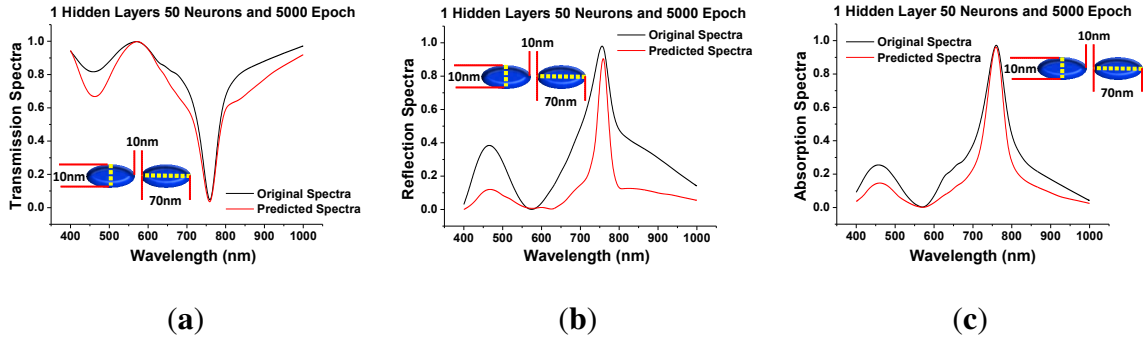


Fig. 6.5 $Hidden\ layer = 1$, $Neurons = 50$ and $Epoch = 5000$ (a) Shows the comparison between the predicted transmission spectra with respect to the original transmission spectra. (b) Shows the anticipated reflection spectra are compared to the original reflection spectra. (c) Shows the predicted absorption spectra against the original absorption spectra.

In Figure 6.5a a black curve shows the original transmission spectra (calculated by COMSOL Multiphysics) with respect to the predicted transmission spectra when the $a = 70$ nm, $b = 10$ nm, $g = 10$ nm, and $h = 40$ nm. Similarly, the reflection and absorption spectra are predicted in Figure 6.5b and 6.5c. Where the original spectral values are shown by the black curves, while the predicted values are represented by the red curves. Where it can be observed that when $hidden\ layers = 1$ and $neurons = 50$, the $MSEs$ was calculated as 0.4 for $epoch = 1$ and rapidly reduces till $epoch = 900$; however, it got stabilised after $epoch = 1000$. Hence, $epoch = 5000$ is used to make initial predictions. Indeed, it is true that the lower $MSEs$, the more predicted spectral values are more closer with respect to actual values. Due to this reason, the remaining hyper-parameters have been tweaked for producing more accurate predictions over the actual spectral responses.

From Figure 6.4. it can be seen, as the number of hidden layers is increased, the predicted results became better. Finally, the appropriate DL neural framework is designed using suitable hyper-parameter selection based on the $MSEs$ determined at every dataset training. In the Final algorithm the $hidden\ layers = 5$, $epoch = 5000$ and $neurons = 50$ were adopted. The

Deep learning for spectral prediction and prospective validation of nanostructured dimers

$MSEs$ was also gets its minimum values 0.20 at $epoch = 1$ and reaches upto 0.05 on $epoch = 200$; however, it stabilises and reaches approximately 0 at $epoch = 5000$.

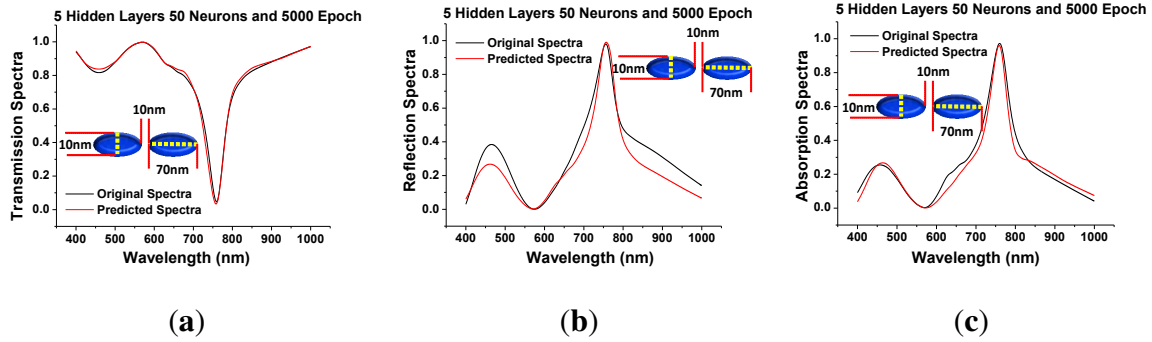


Fig. 6.6 *Hidden layer = 5, Neurons = 50 and Epoch = 5000* (a) Shows the comparison between the predicted transmission spectra with respect to the original transmission spectra. (b) Shows the anticipated reflection spectra are compared to the original reflection spectra. (c) Shows the predicted absorption spectra against the original absorption spectra.

Figure 6.6 illustrates the outcomes from the improved DL neural network where it can be clearly seen that as the $MSEs$ reduces the predicted transmission, reflection and absorption responses reaches more closer to the original spectral values shown by red and black curves, respectively for the specified geometrical dimensions where $a = 70\text{ nm}$, $b = 10\text{ nm}$, $g = 10\text{ nm}$ and $h = 40\text{ nm}$. Altogether, these findings suggest that DL neural network can accurately predict spectra for billions of distinct nanostructures in the a , b , g and h ranges using adequate amount of simulation dataset. They all preserve the same accurate resonance properties as by FEM simulations (using COMSOL Multiphysics), demonstrating that the DL neural network can be well trained for electromagnetic modelling. As a result, it is reasonable to conclude that expanding the training dataset will improve the performance and accuracy of the DL neural network. In this way, it can be stated that the constructed DL neural network outperforms traditional FEM simulation.

The performance of the designed neural network has also been evaluated in terms on the computational cost. Generating large training data sets for DL neural network demands a significant investment of computational effort. This emphasises the critical difficulty of

automatically generating extra data points, particularly for regions that are devalued in the present data collection. Aside from reducing numerical efforts, this would also aid to cut physical labour by reducing the involvement of the researchers in the data curation chain. However, the high computational cost of producing such data sets typically hinders database expansion; as a result, the resulting *DL* neural network are unreliable owing to overfitting and other difficulties.

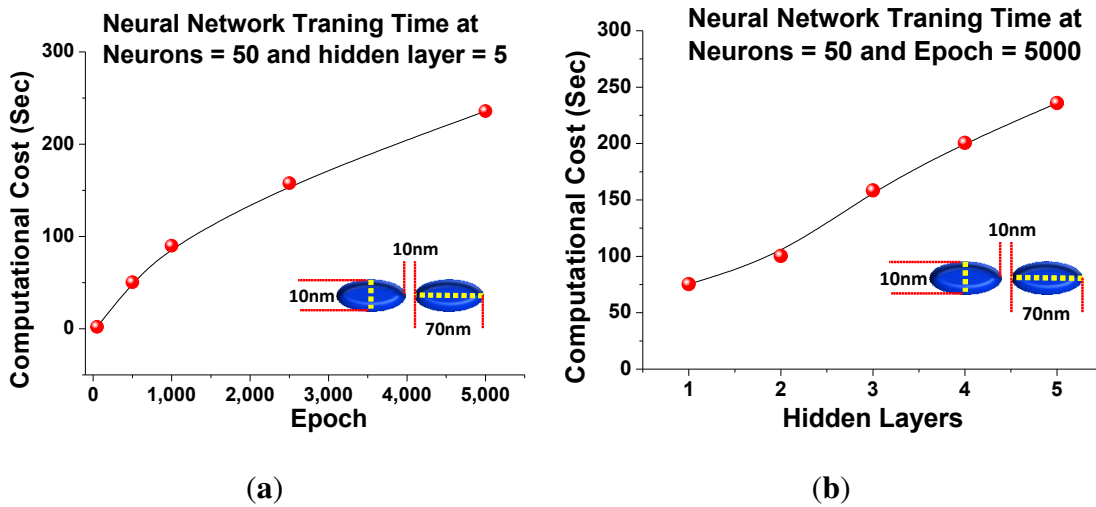


Fig. 6.7 (a) Shows the computational Cost (Sec) for the *DL* neural network training with respect to different *epoch* (b) Represents the comparison in computational cost at different *hidden layers*.

Hence, Figure 6.7a depicts the comparison of training execution time times for different *epoch* when *neurons* = 50 and *hidden layers* = 5. Here, it can be seen that at 10,500 data points the computational cost have been calculated while *DL* neural network training. It is evident that the developed *DL* neural network have shown approximately 1 sec at *epoch* = 1. However, it reaches up to 50 sec for *epoch* = 500. But it is observed that at lower *epoch* the *MSEs* values were high and the predictions were not closer of the actual results. Hence, computational cost has been compared at different *epoch*. As from Figure 6.7a it can be stated that at every *epoch* weights and parameters were stored in the computing machine after the *DL* neural network training was finished and the predictions were made for unseen inputs

Deep learning for spectral prediction and prospective validation of nanostructured dimers

with the aid of previously saved weights at $epoch = 5000$ is also represented in Figure 6.6. As a consequence, it can be inferred that at $epoch = 5000$, the computational cost is 250 seconds, which is rather expensive when compared to the smaller $epochs$, but the performance of the DL neural network has improved. This performance is also far superior to typical FEM solvers, which may take up to 10,200 seconds, 14,100 seconds, 38,160 seconds, and even a day or two to compute the optical spectrum responses for normal, fine, finer, and extremely fine meshes. Next, Figure 6.7b also represents the performance of the DL neural network based on the computational cost with respect to the $hidden$ layers varies from 1-5. Where, it can be seen that at $hidden$ layers = 1 the computational load was comparatively small, approximately 75 sec but in Figure 6.5 it can be seen that the spectral performances was not acceptable hence the DL neural network training has been continued for higher $hidden$ layers. Where it can be seen that at $hidden$ layers = 2, 3, 4 and 5 the computational cost increases from 100 sec, 170 sec, 220 sec and 250 sec. Additionally, the corresponding improvement in $MSEs$ values are also represented in Figure 6.4 from where it is clear that as the $hidden$ layers increases the $MSEs$ values decreased which means that the prediction are getting more closer to the actual spectral values. Hence, the $epochs = 5000$ is selected by the user once $MSEs$ has converged to a suitable threshold. After modifying the model to obtain a stable MSE value, the necessary outputs datapoints were provided as additional input datapoints that was not supplied during the training operation. The term "rectified network" refers to an DL neural network with $hidden$ layers that employs the rectifier function. As the approaches that increasingly facilitate the methodical evolution of DL neural networks, $ReLU$ implementation is most significant breakthroughs milestones in the deep learning rebellion.

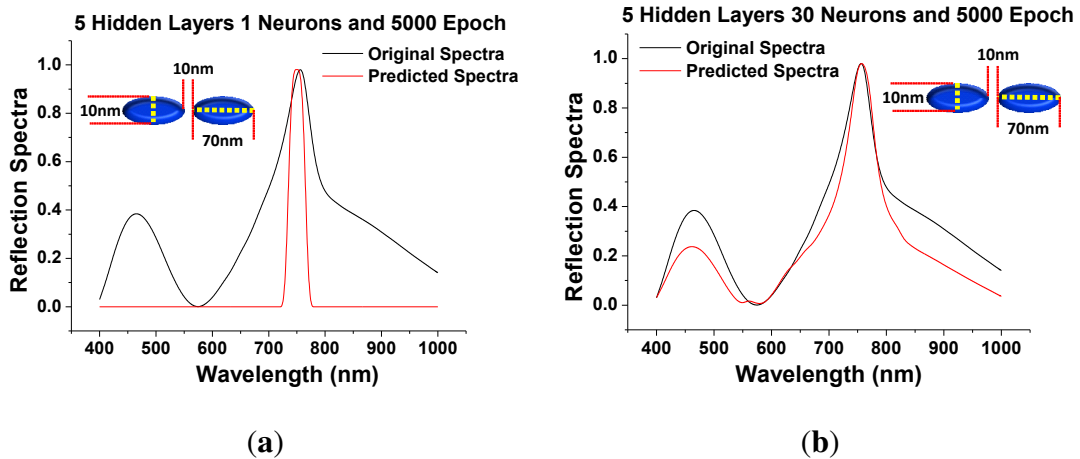


Fig. 6.8 *Hidden layers*= 5 and *Epoch* = 5000 (a) Shows the comparison of predicted reflection spectra with respect to the original reflection spectra at *neuron* = 1 (b) Represents the resemblance of predicted reflection spectra with respect to the original reflection spectra at *neuron* = 30

Next, the performance on the *neurons* at each *hidden layers* has been optimized in Figure 6.8. Since, the *neuron* assesses a set of weighted inputs, implements an activation function, and outputs. An input from *neuron* might be either features from a training set or outputs from *neurons* in a previous layer. Weights are assigned to inputs as they travel through synapses on their route to the neuron. The *neuron* then applies an activation function (*ReLU* in this case) to the "aggregate of synaptic weights" from each arriving synapse and sends the result to *neurons* of following layer. Hence, it plays a crucial role for optimizing any DL neural network. This can be better followed from Figure 6.8a which shows the performance of the predicted spectra when the *hidden layer* = 5, *epoch* = 5000 and *neurons* = 1. From this it can be seen that as the *hidden layer* = 5 and *epoch* = 5000 were optimised still the numbers of *neurons* also plays an important role for stabilizing the DL neural network. Hence, the predicted spectral values at *neuron* = 1 also plotted where red curve shows the predicted spectral values and black curve represents the actual optical spectral values for $a = 70$ nm, $b = 10$ nm, $g = 10$ nm and $h = 40$ nm. Figure 6.8b shows the response of the higher *neurons* used in each *hidden layers* = 5 and *epoch* = 5000. From this it can be inferred that as the

Deep learning for spectral prediction and prospective validation of nanostructured dimers

neurons increases the performance of the predicted spectral values increases where the red curve shows the predicted spectral response with respect to original spectral values shown by a black curve. The entire procedure of the algorithm convergence is shown when *neuron* = 1 and 30. Hence, it can be said that as the number of *neurons* increases the algorithm converges and reaches at its saturation point so the outcomes of the final optimized hyper-parameters when *hidden layers* = 5, *neurons* = 50 and *epoch* = 5000 are shown in Figure 6.6b. To show convergence in the predicted spectral values more clearly, the *MSEs* has been plotted at different number of *neurons* when the *epoch* varies from 0 - 5000 and *hidden layer* = 5. As, it has been already discussed that at the lower *MSEs* the prediction will be more accurate towards the original spectral values.

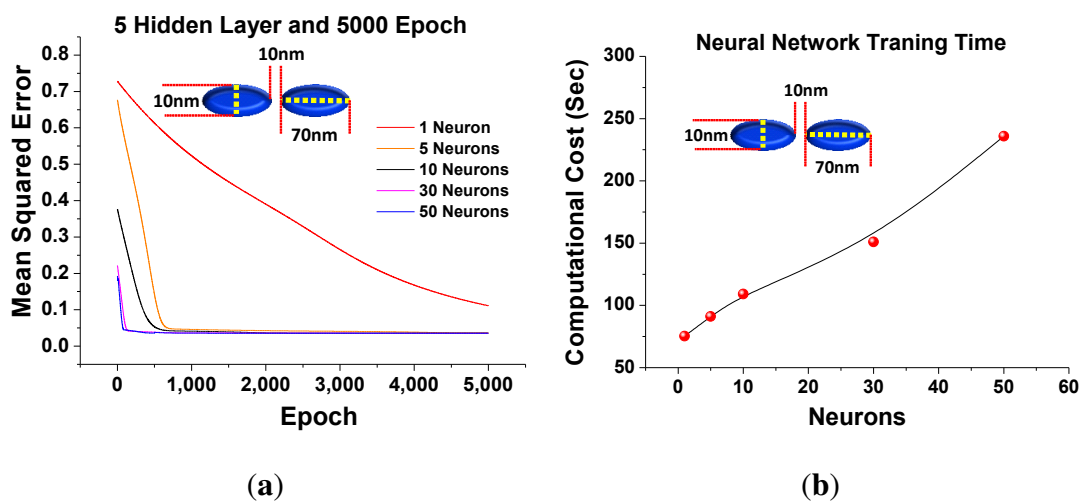


Fig. 6.9 *Hidden layer* = 5 and *Epoch* = 5000 (a) Shows the comparison of *MSEs* at different *neurons* (b) Represents the trend of the computational cost with respect to the variations in *neurons*

Figure 6.9a depicts the improvement in *MSEs* from *neurons* = 1 to 50. Where red curve shows the highest *MSEs* values = 0.75 at *epoch* = 1 and gradually reduces till 0.1 at *epoch* = 5000. Hence, this means the prediction when *neuron* = 1 is not acceptable to make an efficient DL neural network as seen in Figure 6.8a. Hence, to improve the performance even better *neuron* = 5 has been used and the corresponding *MSEs* are shown by the orange curve. This

6.5 Substantiation of in-house developed *DL* neural network for concealed nanostructures

shows that *MSEs* values = 0.68 at *epoch* = 1 and sharply reduces till *epoch* = 1000. Finally, it stabilised till *epoch* = 5000 when *neuron* = 10 are used, as show in Figure 6.8a. Black curve shows the expeditious reduction in *MSEs* values = 0.38 at *epoch* = 1 and decreases till *epoch* = 700 until stabilised. Pink curve shows the further decrements in *MSEs* values = 0.22 at *neurons* = 30 and steadies after *epoch* = 200. The corresponding spectral response is also shown in Figure 6.8b. Finally, *neurons* = 50 have been adopted to see further improvement in the *MSEs* values as shown by blue curve, when the *MSEs* values = 0.18 at *epoch* = 1 and quickly equilibrated after *epoch* = 50. Hence, *neurons* = 50 was considered for further observations as it is showing less *MSEs* values and converges faster. The corresponding predicted spectral values are also shown in Figure 6.6. Figure 6.9b shows the effect of computational cost at different *neurons* when *hidden layer* = 5 and *epoch* = 5000. Here, it is clear that when number of *neurons* = 1 the computation cost were achieved as 50 sec; however, it increased more and reaches up to 250 sec but the *DL* neural network stabilised. This computational cost also depends on the specifications on the computing machine. In this research, cognitive computer with 8 GB RAM, 500 GB harddrive, with the windows operating system (version 20H2 Semi-Annual Channel) have been used but it can be said that by using high end computers the computational time cost can be reduced even more.

6.5 Substantiation of in-house developed *DL* neural network for concealed nanostructures

Finally, after stabilizing the developed *DL* neural network with the help of the all possible hyper-parameters, we demonstrated how deep learning and dynamic challenges are interconnected in this paper, providing the groundwork for future research at the intersection of problems and data science. In particular, we suggest novel topologies for *DL* neural network that increase forward propagation stability. We additionally increase the well-posedness

Deep learning for spectral prediction and prospective validation of nanostructured dimers

of the learning activity by using derivative-based regularisation. We additionally present a multi-level technique for establishing hyper-parameters, which makes *DL* neural network training easier.

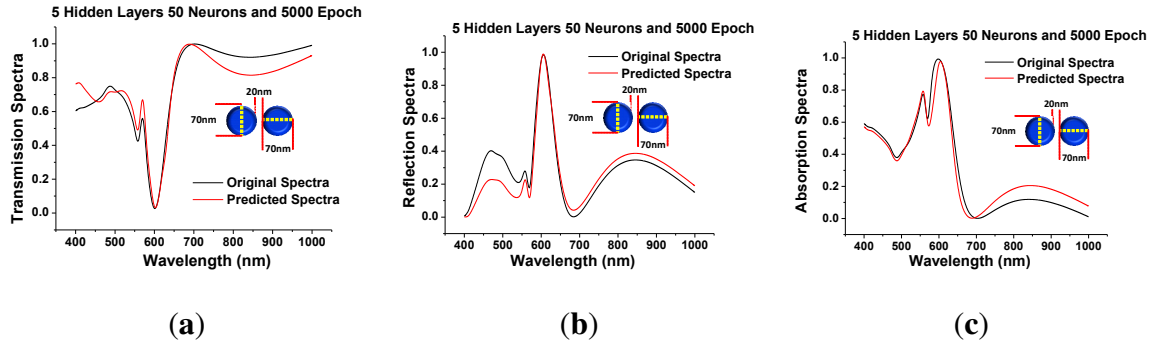


Fig. 6.10 *Hidden layer = 5, Neurons = 50 and Epoch = 5000* (a) Shows the comparison between the predicted transmission spectra with respect to the original transmission spectra when $d = 70\text{ nm}$, $g = 20\text{ nm}$ and $h = 40\text{ nm}$. (b) Shows the anticipated reflection spectra are compared to the original reflection spectra $d = 70\text{ nm}$, $g = 20\text{ nm}$ and $h = 40\text{ nm}$. (c) Shows the predicted absorption spectra against the original absorption spectra $d = 70\text{ nm}$, $g = 20\text{ nm}$ and $h = 40\text{ nm}$.

We additionally present new regularisation techniques that rely on our continuous conceptualization of the challenge to increase generalisation accuracy, consistency, and streamline *DL* neural network training. After designing a stable *DL* neural network, we have used this algorithm for predicting the spectral response for the paired circular nano structure where $d = 70\text{ nm}$, $g = 20\text{ nm}$ and $h = 40\text{ nm}$. Figure 6.10a shows the spectral response of the circular paired nano disk where a red curve shows the predicted spectral values and their actual spectral values calculated by *FEM* are shown by a black curve. Similarly, Figure 6.10b and c show the predicted reflection and absorption spectra (shown by red curves) and actual reflection and absorption values are shown by in black curve.

6.5 Substantiation of in-house developed *DL* neural network for concealed nanostructures

6.5.1 Evaluation of in-house developed *DL* neural network for imperceptible geometric dimensions (beyond the training dataset)

In this section, we have discussed the performance of the designed *DL* neural network when it predicts the spectral values outside the range of the training dataset. The geometric parameters are selected at random from the test sets outside of the training dataset and manually verified from the commercial software for the plasmonic nanostructures to examine the performance optimization of the transmission and reflection values for an arbitrary wavelength and visualize the outcomes. In this entire training, we have used the dataset of major axis (a) from 10 nm to 130 nm with 10 nm interval.

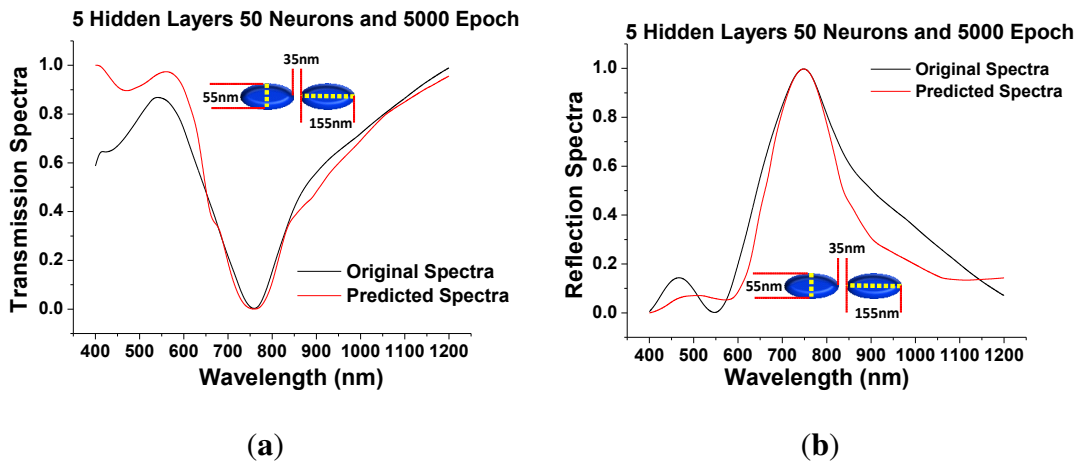


Fig. 6.11 *Hidden layer* = 5, *Neurons* = 50 and *Epoch* = 5000 (a) Shows the comparison between the predicted transmission spectra against the original transmission spectra when $a = 155$ nm, $b = 55$ nm, $g = 35$ nm and $h = 40$ nm. (b) Shows the anticipated reflection spectra are compared to the original reflection spectra $a = 155$ nm, $b = 55$ nm, $g = 35$ nm and $h = 40$ nm.

Hence, in this section the spectra has been predicted when major axis (a) = 155 nm, minor axis (b) = 35 nm and separation gap (g) = 55 nm. It is worth to note that Figure 6.11 shows spectral response of the optimised *DL* neural network with prediction accuracy and reliability more than 90% when the training data-points was approximately 50,000 to show the impact of the test set, which was outside from the training set range. Where black curve shows the

Deep learning for spectral prediction and prospective validation of nanostructured dimers

original spectral values computed from the Comsol Multiphysics and the red curves shows the spectral values predicted from the in-house developed neural network.

6.5.2 Evaluation of in-house developed neural network on the experimental spectra

In this section, we have tested the predicted spectra from the in-house developed neural network on the experimental spectra. The pattern of the experimental spectra has been adopted from the Liu et. al [20]. In this work, they have experimentally developed the gold plasmonic nano antenna having dimensions $a = 110$ nm, $g = 17$ nm, $b = 35$ nm and $h = 40$ nm.

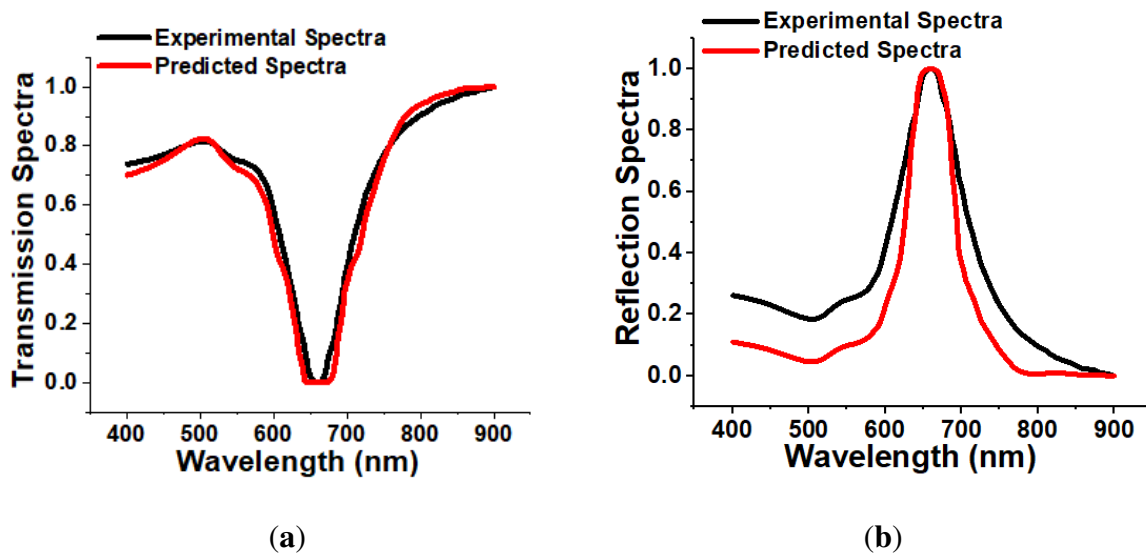


Fig. 6.12 *Hidden layer = 5, Neurons = 50 and Epoch = 5000* (a) Shows the comparison between the predicted transmission spectra with respect to the experimental transmission spectra when $a = 110$ nm, $b = 35$ nm, $g = 17$ nm and $h = 40$ nm. (b) Shows the anticipated reflection spectra are compared to the experimental reflection spectra $a = 110$ nm, $b = 35$ nm, $g = 17$ nm and $h = 40$ nm.

Figure 6.12 shown the comparison of the experimental and predicted spectra where red curve shows the predicted spectra and black curve shows the experimental spectra. In can be seen in these curves that the peak and dip of the predicted spectra is perfectly

matching with the experimental spectra. Hence, from the developed algorithm the resonating wavelength and the spectral information can be predicted. Hence, this work can be significant facilitator of cutting-edge nanotechnology research is the capacity to swiftly extract the desired optical response from an artificial neural network from the geometrical parameters of a plasmonic nanostructures. One can envision a variety of scenarios in which such data is essential to the design of investigations. The highlights this *DL* neural network is that it has a capacity to address multiple targeted resonance spectra for various paired geometrical dimensions, and it emphasises that this technique may be applied to other molecules for sensing in biology, chemistry, and material science. Hence, it can be said that the spectrum prediction from the nanostructures have a high degree of employability, indicating that this techniques might indeed be useful in wide range of spectral and non-spectral aspects. This deep learning protocol has the potential to revolutionize real-time field applications in a variety of spectroscopic disciplines.

6.6 Summary

In summary, this work demonstrates the use deep learning to correlate spectroscopic knowledge of a paired nanostructure and in local environments. The presented *DL* neural network algorithms can estimate spectral values of designed paired nano structures at a three-order of-magnitude lower computing cost than the traditional *FEM* solver while sustaining the same degree of precision. This study illustrates *DL* neural network has been tested rigorously and shown its excellent predictions using one time trained process. *Hidden layers = 5*, *neurons = 50* and *epoch = 5000* were employed all across the neural network to provide swift convergence and good precision in estimating spectral values for randomized input geometrical dimensions of the paired nanostructures. In this work, we have also shown the performance of the associated hyper-parameters of the designed *DL* neural network and explained in terms of *MSEs* which is plotted with respect to *hidden layers*, *epoch* and *neurons*.

Deep learning for spectral prediction and prospective validation of nanostructured dimers

This research also offers a contrast between traditional *FEM* solver and in-house developed *DL* neural networks in terms of computing time, which is nearly 40 times faster than direct *FEM* simulations (when normal mesh size is used). Finally, the performance of the proposed *DL* neural network model was proven for the random input parameter for inside and outside the training dataset such as paired circular when $d = 70$ nm and $g = 20$ nm and paired elliptical dimers when $a = 155$ nm, $b = 55$ nm and $g = 35$ nm respectively, and corresponding spectral values were predicted. The detection of structural variations/fluctuations in chemical reactions, automatic identification of interstellar molecules, and real-time recognition of particles in biomedical diagnosis are just a few of the significant functions of precise spectrum prognostication and insightful framework recognition. As a result, we conclude the consolidation of nanotechnology and artificial intelligence will open the direction for several other new technological advancements in the profession of comprehension scientific disciplines.

Chapter 7

Advanced refractive index sensor using 3-dimensional metamaterial based nanoantenna array

7.1 Introduction

Researchers have become more interested in surface plasmon polaritons (SPPs), since they provided a fresh, remarkable opportunities for the future era of nanotechnologies. The progress of optics includes the integration and miniaturization of optoelectronic circuitry and subsystems. To construct effective nano photonic devices [164] with ultra-fast operational speed and the capability to concentrate the electromagnetic field into a region significantly narrower than the operating wavelength [165], using SPPs ensures that the objectives of the nanophotonic branch [166] are addressed. SPPs have extensively been used in several technologies, including waveguides [167], modulators [168], nano-lasers [169], and nano-antennas [170]. Initial studies with nanosized antenna focused primarily on controlling the localized incident electromagnetic pattern while responding with an incident electromagnetic radiation from the free space. A wide range of devices are needed in systems involving

Advanced refractive index sensor using 3-dimensional metamaterial based nanoantenna array

detectors and spectroscopy instruments. However, when equipment is being developed for optics, the antenna would need to transmit electromagnetic signal in-plane, broadcast it to space, and, via reciprocity, would need to be able to receive the data from space and guide it in-plane. Due to advancement of semiconductor fabrication techniques and electron beam lithography, researchers have lately delved into the manufacture of nano-antenna [170], which range in size from a few hundreds of nanometers to over several microns. These may be advantageous because of their rapid transient response, compactness, and efficiency parameters adjustability. However, since metals become dispersive in the visible spectrum, so it must be simulated with accurate dielectric permittivity function. While the dielectric resonator was used to create the antenna described in [171], most nanoantenna working in the optical regime rely on the plasmonic resonance principle [172, 173], and [174]. In addition to these methods, hybrid plasmonic structures have been used to build nano-antennas [175, 176]. Yousafi *et al.* [175] have suggested a rectangular patch nanostructure to radiate the localized electromagnetic wave power of a hybrid plasmonic waveguide [177–179] in which the electromagnetic waves were contained in thin material having very low refractive index in between plasmonic metallic layers. Unfortunately, the applicability of surface plasmons polaritons (SPPs) for many real-world applications is considerably restricted by their substantial signal attenuation. To attain long propagation length by fusing the dielectric and plasmonic antenna, the hybrid plasmonic mechanism has been employed for nano-antenna design. Due to significant ohmic losses, earlier nano-antenna performances have mostly been plasmonic in nature, which have a very low efficiency [180–182]. Their performance can be increased by reducing losses by exploiting Hybrid Plasmonic Waveguide (HPW) nano structures and thus for proposed antenna, performance of earlier reported HPW microstructures can be further enhanced [175, 183–185]. To increase the localized electric field of plasmonic nanostructures, several attempts have been considered. Adjusting an antenna's structures, particularly its separation distance

[186, 80, 187], is an effective technique to increase its applied electric field enhancement for plasmonic nanostructures [188, 189]. However, as the separation distance enters the subnanometer zone, quantum interactions become apparent and prevent additional field augmentation [190–194]. Additionally, certain separation distances and widths for the antennas are needed for various metal or dielectric photonic nanostructures, to greatly enhance the localized field of the nano structures [195–198]. The conventional approach in these connected systems is to augment the effective electromagnetic field excitation by the nanostructures. The linked structure is significantly bigger than the operating wavelength and is often achieved by utilizing a periodic pattern (photonic crystal) or film. Due to extremely confined electric and magnetic resonance responses and minimal material losses, dielectric nanostructure with large refractive index have presently received a significant attention among the researchers [199–202]. Many nanoscale applications, including meta-surfaces [202, 203], meta-materials [204], architectural colour combinations [205], and optical nano antenna [206–209], have been reported due to their excellent properties. It should be noted that these low-order electromagnetic resonance dielectric structures [199–201] have substantially smaller diameters than the previously reported series of dielectric structure [197, 198]. Dielectric and plasmonic nanostructure combinations have been demonstrated to be able to alter the linear and non-linear far field behaviours of paired structures [210–215] as well as they emit radio frequencies to work as antenna [215, 216]. Robust electromagnetic near field enhancements and large far field scatterings are frequently present in conjunction with the significant optical response of dielectric nanostructures. The magnetic and electric near fields are commonly dispersed across the volume of conventional dielectric nanostructures. For instance, the electric field around a magnetic dipole mode typically rotates [201]. Contrary to its plasmonic equivalents, dielectric nanostructures' spatially large dispersion of the electromagnetic field makes it difficult to achieve reasonably robust field enhancement. On the other hand, such a distribution suggests that if I place the antenna near the dielectric structure's electric field, the

Advanced refractive index sensor using 3-dimensional metamaterial based nanoantenna array

electromagnetic field intensity of a tiny plasmonic nano structures can be increased. Despite a few earlier examples, this form of combination has not received significant consideration [217]. In this chapter, I have proposed a novel hybrid with Lithium Tantalate ($LiTaO_3$) or Aluminium Oxide (Al_2O_3) multilayer stacked elliptical shape paired nanoantenna as they can strongly confine and maintain surface plasmon polaritons (SPPs) operating at spectrum ranging from 400 nm–2000 nm. Recently published multilayered hybrid plasmonic antenna, which surpasses prior plasmonic waveguides in terms of confinement and propagation losses [183, 184], served as the inspiration for the proposed hybrid nanostructures. Unlike the usually presented local field antenna, our proposed nano structure enables an efficient performance even while retaining a very high intensity in the local field. This chapter is divided into four sections where Section 7.1.1 describes the computational design and optimization methods. Section 7.2.1 evaluates the parametric studies of the multi-layer structure. Finally, in Section IV a conclusion and future possibilities are drawn.

7.1.1 Approaches for computational design and optimization

In this chapter, the Comsol Multiphysics software enabled with Finite Element Method (FEM) has been used to calculate the plasmonic response and to design the coupled hybrid nano structured antenna as shown in Figure 7.1. Figure 7.1a shows a 3D view of the schematic of designed computational domain of hybrid nanostructured antenna. The dielectric properties of gold have been calculated using the Drude-Lorentz model as it is based on the movement of the unbounded electrons in the metal that causes the surface plasmon resonance. The material properties of $LiTaO_3$ and Al_2O_3 have been taken from the Moutzouris *et al.* [218] and Boidin *et al.* [218], respectively. To reduce the computational time, I have designed the unit cell enforcing the periodicity in the x and y directions. In the computational domain the Perfect Magnetic Conductor (PMC) has been used along the x -axis and Perfect Electric Conductor (PEC) has been employed along the y -axis. To reduce the back reflection, the

Perfect Matched Layer (PML) has been used along the z -direction. The quartz substrate has been optimized [122] at $400 \times 200 \text{ nm}^2$ length and width, respectively. A hybrid nano antenna has been excited by x -polarized light in the z -direction from the top of the antenna as shown in Figure 7.1a. The final design of the 10 layered hybrid sensor system placed on the $400 \times 200 \text{ nm}^2$ quartz is shown in Figure 7.1b. In this section I have calculated the sensitivity of the paired hybrid nanoantenna and compared them with a single metallic nano antenna.

Next, I explore the sensitivity performance of the 10 total layered, with 5 layers of LiTaO_3 (or Al_2O_3) and gold each, stacked elliptical-shaped paired nano structure, with its minor axis, $b = 10 \text{ nm}$ and major axis, $a = 100 \text{ nm}$. Linearly x -polarized electromagnetic waves propagating in the z -direction were used to illuminate these paired nano structures. Through analysis of transmittance at various refractive index levels, its sensitivity has been optimized. Figure 7.1c displays the transmission spectra for a design specification using various surrounding medium (n). Here, the major axis $a = 100 \text{ nm}$, minor axis, $b = 10 \text{ nm}$, separation distance, $g = 10 \text{ nm}$ and $h_1 = 10 \text{ nm}$ and $h_2 = 10 \text{ nm}$ are selected, as the LiTaO_3 (or Al_2O_3) and gold (Au) thickness, respectively of the stacked nano structure. Since Figure 7.1c demonstrates a more effective change in resonating wavelength, it can be employed as a refractive index sensor and is a good contender for biosensing applications. The spectral absorption of the narrow band paired structures can also be modified to match the distinctive absorption spectra of a certain targeted RI in order to identify targeted medium inside the infrared range.

Advanced refractive index sensor using 3-dimensional metamaterial based nanoantenna array

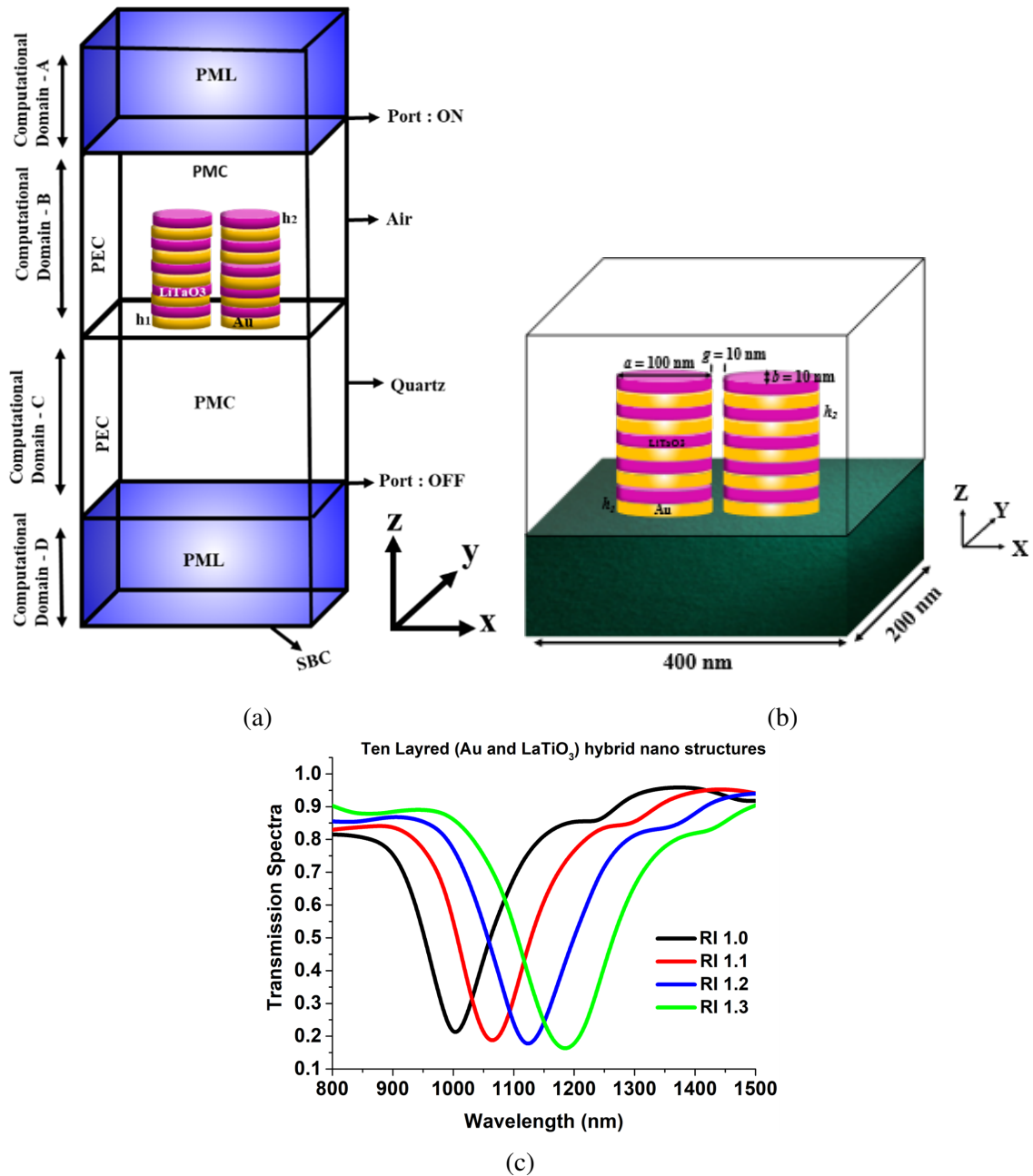


Fig. 7.1 (a) Schematic of the computational domain designed on the FEM method enabled commercial software (b) Graphical representation of the designed hybrid refractive index sensor (c) Transmission spectra of the optimized paired elliptical nano structure with major axis, $a = 100$ nm and minor axis, $b = 10$ nm.

To calculate the sensitivity, the following equation has been used.

$$S = \frac{-\delta\lambda_{res}nm}{\delta\lambda_{ns}RIU} \quad (7.1)$$

Where, λ_{res} is the shift in the plasmonic wavelength and n_s is the surrounding refractive index.

7.2 The parameterized investigation of the multi layered structure

In this section, I have analysed the performance of a hybrid nano structure and compared with a single metal nano structure. Figure 7.2a shows the comparative analysis of sensitivity of the single, paired circular and paired elliptical metallic nano structures. Here, black curve shows when $h = 100$ nm the sensitivity value was nearly 5 nm/RIU and increases as h is reduced and reaches nearly 200 nm/RIU when $h = 10$ nm for a single nano disk. The response of the paired circular nano antenna when $a = b = 100$ nm and $g = 10$ nm is shown by a red curve and the highest sensitivity of 250 nm/RIU was achieved when $h = 10$ nm, which sharply increases for lower h values. The sensitivity response of the paired elliptical shaped antenna is shown by a blue curve when $a = 100$ nm, $b = 10$ nm, and $g = 10$ nm. The blue curve shows the highest sensitivity value of nearly 525 nm/RIU at $h = 10$ nm and gradually decreases for higher h values. In all cases, it can be observed that the highest sensitivity of single metal dimer can be achieved nearly 525 nm/RIU when its height is reduced to 10 nm. Verma *et al.* [122] and results presented in Chapter 4 show that the separation distance, g decreases, the value of the sensitivity increase and at the $g = 10$ nm, the highest sensitivity values has been achieved. Additionally, the performance of the symmetry has also been discussed with respect of the separation distance, g . In this work I will show that the performance can be

Advanced refractive index sensor using 3-dimensional metamaterial based nanoantenna array

further improved by placing layer of $LiTaO_3$ or Al_2O_3 on top of the metallic paired nano antenna.

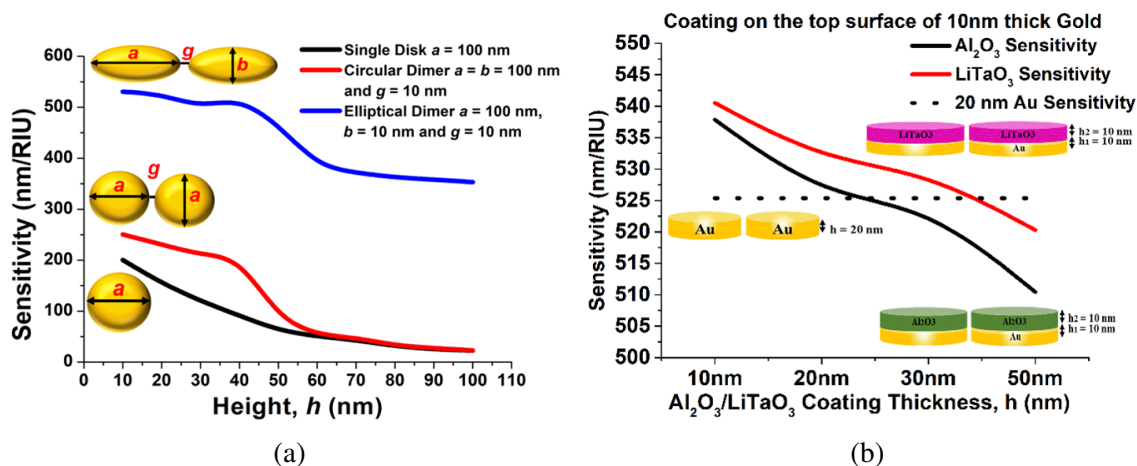


Fig. 7.2 (a) Shows the performance of the single, coupled circular and coupled elliptical shaped gold nano antenna (b) Shows the sensitivity performance of the two-layer hybrid nanoantenna.

Figure 7.2b shows the sensitivity comparison of the paired gold elliptical shaped antenna where the $LiTaO_3$ or Al_2O_3 has been stacked on earlier optimized [122] elliptical dimer with $a = 100$ nm, $b = 10$ nm, $g = 10$ nm, and metal thickness $h_1 = 10$ nm. Black dashed curve shows nearly 525 nm/RIU sensitivity of single layer gold elliptical dimer antenna when h was kept constant at 20 nm. On the other hand, when Al_2O_3 was placed on the top of paired elliptical shaped antenna the sensitivity increases and reaches up to 532 nm/RIU (shown by the black curve). The values increase even more and reaches up to 543 nm/RIU (shown by a red curve) for $LiTaO_3$, for $h_2 = 10$ nm. From this it can also be stated that as the height h_2 , of the $LiTaO_3$ and Al_2O_3 layer decreases the sensitivity is increasing. Although, it is true that sensitivity increases as metal or dielectric layer thickness is reduced, but getting very thin layer may bring fabrication uncertainty and for a fair comparison, the minimum height, h_2 of the $LiTaO_3$ and Al_2O_3 layer is fixed at 10 nm for further observations.

7.2.1 Performance of multi-layered elliptical shaped antenna stacked with Al_2O_3 and $LiTaO_3$

Sensitivity of the stacked antenna is next evaluated in this section, where I have shown the sensitivity performance of multiple layered paired elliptical shaped antennae designed when $a = 100$ nm, $b = 10$ nm, $g = 10$ nm, and $h = 100$ nm. Red curve in Figure 7.3a shows the sensitivity values when height, h varied from 10 nm to 100 nm for single metal elliptical dimer. From this figure it can be observed that at a large value of height, $h = 100$ nm the sensitivity of the single metal antenna its lowest with a value of nearly 360 nm/RIU was achieved. However, as the height, h is reducing to 10 nm, the sensitivity increases and reaches its highest values nearly 525 nm/RIU. On the other hand, the blue curve shows that as number of the layers in the stacked antenna (with Al_2O_3) with $a = 100$ nm, $b = 10$ nm, $g = 10$ nm, $h_1 = 10$ nm, and $h_2 = 10$ nm is increasing the sensitivity rather increases when the height of stacked layer is increasing and reaches up to its saturation point of nearly 660 nm/RIU. In other words, it can be concluded that by using Al_2O_3 stacked antenna the sensitivity can be enhanced by 1.5 times as compared to a single metallic antenna keeping h_1 fixed at 10 nm.

Advanced refractive index sensor using 3-dimensional metamaterial based nanoantenna array

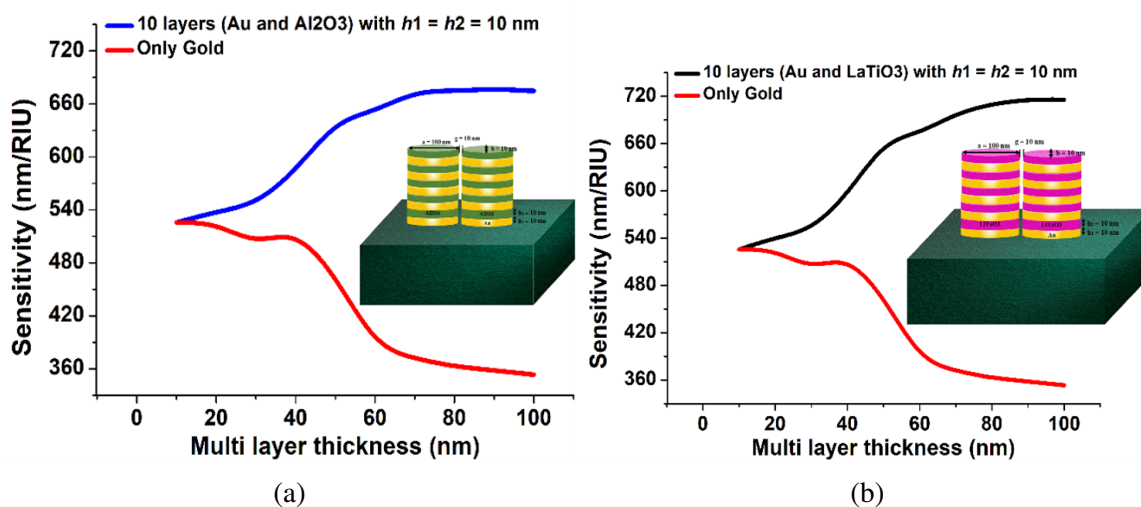


Fig. 7.3 (a) Shows the sensitivity performance single metallic (Au) and Al_2O_3 stacked antenna when total height, $h = 100 \text{ nm}$ with or without stacked (b) Shows the sensitivity performance single metallic (Au) and $LiTaO_3$ stacked antenna when total height, $h = 100 \text{ nm}$ with or without stacked.

Similarly, Figure 7.3b demonstrates that by using 10 layered $LiTaO_3$ stacked antenna with $a = 100 \text{ nm}$, $b = 10 \text{ nm}$, $g = 10 \text{ nm}$, $h_1 = 10 \text{ nm}$, and $h_2 = 10$, sensitivity can be further enhanced by more than two folds (nearly 730 nm/RIU) as compared to the single gold elliptical paired antenna. It is worth noting a remarkable more than two-fold increase of the sensitivity and the highest electromagnetic field confinement that has been observed by using the stacked antenna approach. Hence, such $LiTaO_3$ and Al_2O_3 stacked plasmonic sensor can detect the small change in the surrounding medium with a sensitivity of about 730 nm/RIU and 660 nm/RIU , respectively and its sensitivity is expected to increase further by decreasing the height of the individual layers and also corresponding separation distance.

7.2.2 Study of field distribution around the single metal and ten layered (5 Pairs of gold and $LiTaO_3$ stacked elliptical shaped antenna

In this section, the performance of electric field distribution along the single metal and stacked antenna is discussed. The normalized electric field intensity of the single gold circular and

7.2 The parameterized investigation of the multi layered structure

elliptical pair was calculated (from COMSOL Multiphysics) nearly 8.6×10^2 V/m and 2.9×10^4 V/m reached at the inner edge as shown in Figure 7.4a (i) and (ii). Variation of the electric field, E_x along the x direction through the centre of the single metallic (gold) elliptical nano structure is shown in Figure 4b by a red curve which is compared with the Al_2O_3 and $LiTaO_3$ stacked nanostructured field distribution shown by the black curve (shown in Figure 7.4b(i) and 7.4b(ii)). In the case of the Al_2O_3 stacked nano structure the electric field intensity was calculated nearly 5.4×10^4 V/m which is nearly 9 times higher (shown by a black curve in Figure Figure 7.4b(i)) than that of the single metallic elliptical shaped nano structure shown by a black curve. How-ever, the electric field intensity even increases further up to 6.5×10^4 V/m at the inner edges of the $LiTaO_3$ stacked elliptical nano structure with $a = 100$ nm, $b = 10$ nm, and $h = 100$ nm shown by a black curve in Figure 7.4b(ii). This value is nearly 10.5 times of a single gold elliptical nano structure, with $a = 100$ nm, $b = 10$ nm, and $h = 100$ nm. The higher sensitivity shown in Figure 7.3 was due to its strong electric field confinement and thus, a $LiTaO_3$ stacked elliptical nano structure can be considered as a very promising choice for many bio sensing applications as compared to the Al_2O_3 and single metallic nano structure. For single elliptical dimer but height, $h = 100$ nm, Figure 7.4c shows mode profile along the centre of the $x - z$ plane and demonstrating that where most of the electric field confinement occurs at the sharp corners and in the separation gap between the two elliptical nano structure. As I have considered elliptical dimer, higher electric field exists close to narrower corners and variation of E_y along the $x - z$ plane for a single elliptical dimer with $h = 100$ nm is shown in Figure 7.4c.

Advanced refractive index sensor using 3-dimensional metamaterial based nanoantenna array

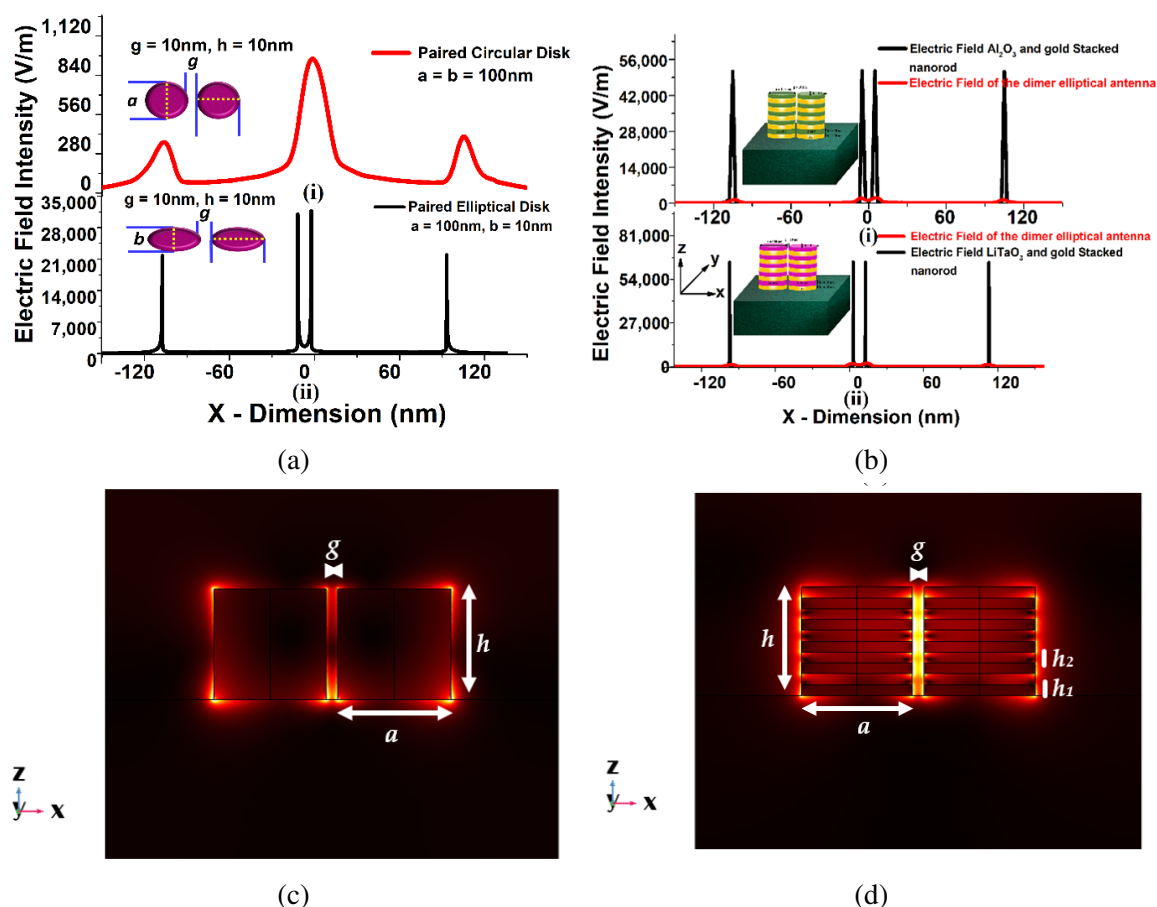


Fig. 7.4 (a) Electric field distribution along the x plane in the gold elliptical and circular paired structure when $a = 100\text{ nm}$, $b = 10$, $g = 10\text{ nm}$ and $h = 10$ (b) Electric field distribution along the x plane in the single gold and stacked 10 layers (with LiTaO_3 or Al_2O_3) elliptical paired structure when $a = 100\text{ nm}$, $b = 10$, $g = 10\text{ nm}$ and $h_1 = h_2 = 10\text{ nm}$. (c) E_y , mode field profile of a single metallic elliptical nano structure when $a = 100\text{ nm}$, $b = 10\text{ nm}$, and $h = 100\text{ nm}$ along the $x-z$ plane (d) Electric field variation along the $x-z$ plane for a 10 layered LiTaO_3 stacked nano structure when $a = 100\text{ nm}$, $b = 10\text{ nm}$, and $h_1 = h_2 = 10\text{ nm}$.

This demonstrates that, due to the absence of a circular symmetry, the electric field intensity was more localized near to sharper corners and at 4 single metal/ dielectric interfaces, at the upper, lower and two sides. The electric field distribution along the centre of the $x-y$ plane of stacked nanostructure is also shown in the Figure 7.4d where most of the electric field occurs. From there it can be clearly observed that the electric field intensity is higher and localized at all metal/dielectric interfaces including the 8 inner metal/dielectric interfaces in the stacked nano structure as compared to the single metallic nano structure.

7.3 Effect of the separation distance on the $LiTaO_3$ and Al_2O_3 stacked nano structure.

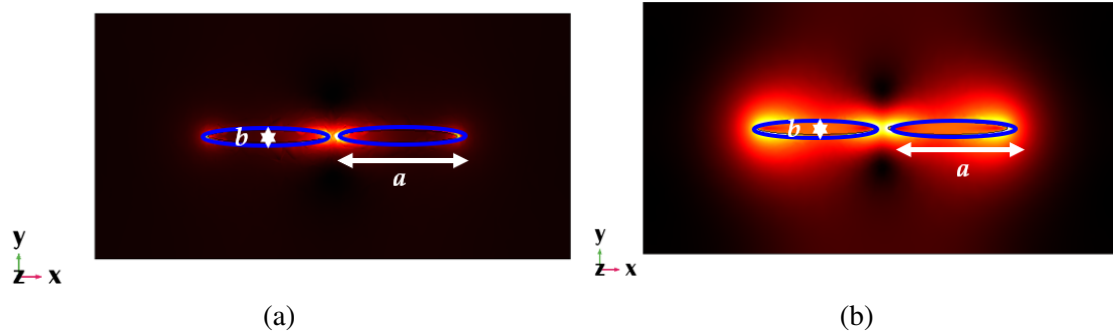


Fig. 7.5 (a) E_x , mode field profile in the $x - y$ plane of a single metallic elliptical nanostructure when $a = 100$ nm, $b = 10$ nm, and $h = 100$ nm (d) Electric field profile in the $x - y$ plane for a 10 layered $LiTaO_3$ stacked nano structure when $a = 100$ nm, $b = 10$ nm, and $h_1 = h_2 = 10$ nm.

Figure 7.5a displays the E_x , mode field pattern along the $x - y$ plane for an elliptical dimer with height, $h = 100$ nm. It can be observed that the sharp corners and separation gap of the elliptical nanostructure are where most of the electric field confinement occurs. The E_x field profile has been shown along the $x - y$ plane when $z = 0$ for the $LiTaO_3$ stacked antenna as shown in Figure 7.5b. This indicates that the field was more concentrated at corners and at four single metal/dielectric contacts, because of the absence of circular symmetry as shown in Figure 7.5b. Hence, from here it can be stated that the stacked antenna is more efficient candidate for the sensing application compared to single metal antenna even with the same other structural dimensions.

7.3 Effect of the separation distance on the $LiTaO_3$ and Al_2O_3 stacked nano structure.

It is well known that the structural dimensions of the nano structures can enhance the field intensity in the separation gaps and due to this field enhancement the sensitivity can be affected, so next the performance of the 10 layered $LaTiO_3$ and Al_2O_3 stacked nano structure is studied. Hence, a 10 layers paired elliptical dimers on the quartz crystal is studied and

Advanced refractive index sensor using 3-dimensional metamaterial based nanoantenna array

calculated the sensitivity when the surrounded medium was covered by the different refractive indices from 1.0 to 1.5. Here, it can be noted that as shown in earlier Figure 7.1c for a single case, as the refractive index was increasing, the resonating wavelength was shifting towards the higher range.

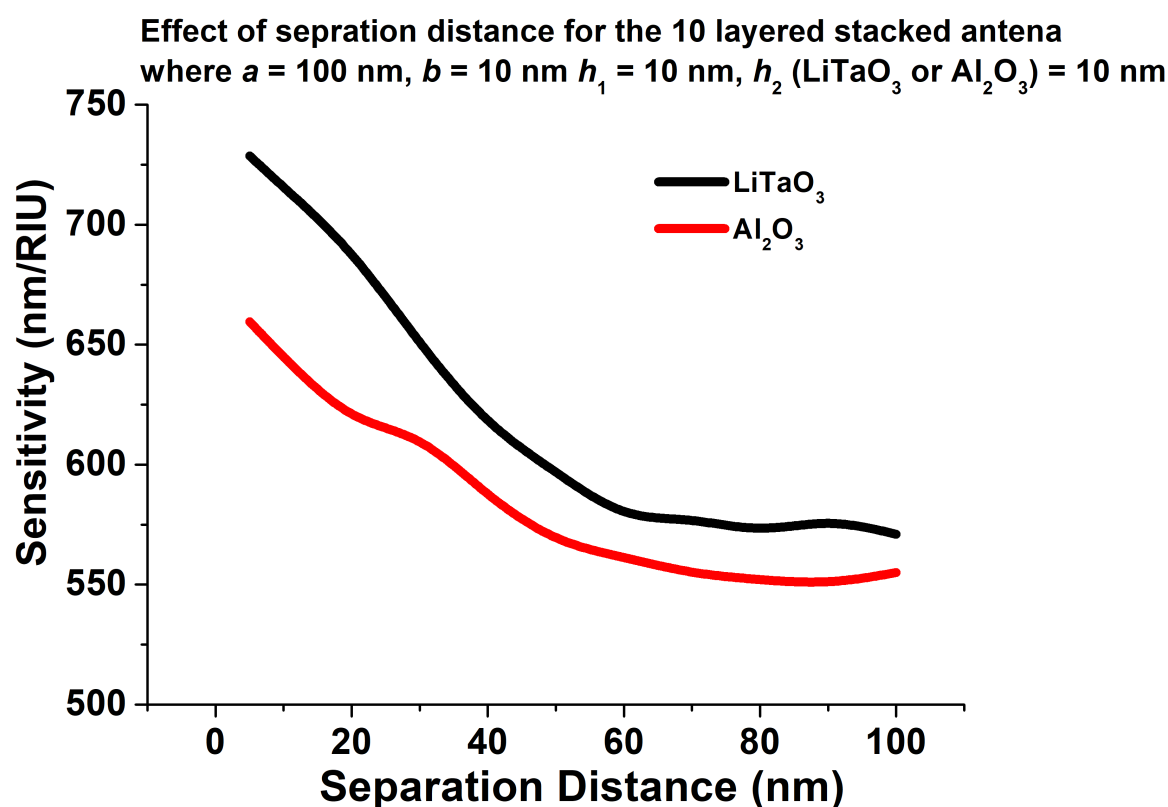


Fig. 7.6 Sensitivity comparison of 10 layered stacked antenna (5 gold layers with $h_1 = 10$ nm gold and 5 $\text{LiTaO}_3/\text{Al}_2\text{O}_3$ layers with $h_2 = 10$ nm) with respect to separation distance.

Figure 7.6 shows the sensitivity of the LiTaO_3 and Al_2O_3 stacked nano structure when the separation distance, g varying from 10 nm to 100 nm. The sensitivity of the 10 layered LiTaO_3 stacked paired nanostructure is calculated from the slopes of the shift in the transmission spectra from where I observed the linear relationship between the RI values and the plasmonic wavelengths. The R-square error value was calculated as 0.9991 and 0.9817 for 10 layered LiTaO_3 and Al_2O_3 stacked paired nanostructure, respectively suggesting al-most linear response. Figure 7.6 clearly shows that as the separation distance, $g = 100$ nm the sensitivity

7.3 Effect of the separation distance on the $LiTaO_3$ and Al_2O_3 stacked nano structure.

reaches 545 nm/RIU, which is effectively the sensitivity of single isolated layered elliptical dimer. But when the separation distance, g reduced further and reaches up to 60 nm the sensitivity remained nearly constant at 550 nm/RIU. Finally, at the separation distance, $g = 10$ nm the sensitivity increases rapidly and reaches up to 660 nm/RIU as shown by the red curve. Similarly, the sensitivity dependence of the $LiTaO_3$ stacked antenna with the separation distance shown by the black curve. The highest sensitivity of the $LiTaO_3$ stacked antenna was achieved nearly 770 nm/RIU when $g = 10$ nm and reduces gradually with the increase in the separation distance. Finally, after $g = 60$ nm remained nearly constant as shown by the black curve, and at $g = 100$ nm the sensitivity was obtained up to 555 nm/RIU. When the separation distance, g is higher, effectively these metallic antennas are uncoupled and achieved 555 nm/RIU and 545 nm/RIU sensitivity when they can be considered as isolated. However, as the separation distance, g is reduced these two isolated antennas are now coupled and formed an effective dimer and their sensitivity reached up to 660 nm/RIU and 770 nm/RIU for hybrid Al_2O_3 and $LiTaO_3$ structure, respectively. So, it is demonstrated here that, sensitivity of the hybrid $LiTaO_3$ and Al_2O_3 paired nano structure is always higher than that of single metallic nano structure. Tsai *et al.* also [97] reported that by using a coupled nano ring, sensitivity can be enhanced up to 50 % but our work shows that for elliptical nano structure the sensitivity values can be further increased by more than 150 % while using a much smaller overall size of the antenna compared to [122] and a further sensitivity enhancement is shown in this work by using the stacked antenna nanostructure. Hence, this can be an attractive method for detecting the heavy metals, biochemicals, air quality, and water purity, this is more efficient and cost-effective (it they are fabricated in bulk), as well as opening up new ways for both healthcare and environmental monitoring applications.

7.4 Summary

In Conclusion, I have reported a study of a hybrid ($LiTaO_3$ and Al_2O_3) stacked metallic nano plasmonic sensor. The designed and optimized sensor with $a = 100$ nm, $b = 10$ nm, $g = 10$ nm, $h_1 = 10$ nm, and $h_2 = 10$ nm has been evaluated in various surrounding refractive indices from 1.0 to 1.5 to calculate their corresponding sensitivity. The transmission, absorption, reflection spectra and modal field profiles have also been calculated to observe the sensor performance. The designed hybrid sensor has been compared with single metallic nanoantenna when $a = 100$ nm, $b = 10$ nm, $g = 10$ nm, and $h = 100$ nm to observe the sensitivity enhancement. From the above shown results, it can be stated that the sensitivity can be enhanced by nearly 1.5 times by using Al_2O_3 stacked antenna and more than 2 times by using $LiTaO_3$. It is also shown that sensitivity can be further increased by reducing metal height, h_1 and dielectric height, h_2 or separation distance, g . But for the fair comparison the values of these are taken as 10 nm. The normalized electric field intensity of the $LiTaO_3$ and Al_2O_3 stacked antennas were stronger, nearly 6.5×10^4 V/m and 5.4×10^4 V/m respectively, which was approximately more than 10.5 times of the single metallic nanostructure for $LiTaO_3$ and 9 times for Al_2O_3 stacked antenna. The proposed nano-enhanced antenna's sensitivity is proven by using of a full-wave electromagnetic simulation. Our suggested nano-antenna may be used for different nano inter- and intra-chip photonic sensor systems to develop cutting-edge detecting devices for measuring the quality of water, air, and soils. Furthermore, due of its wide frequency coverage, this suggested antenna may be employed for biosensing, optical energy harvesting (also known as nano-rectenna or Nantenna) and optical sensing applications.

Chapter 8

Conclusion and Future Work

In this dissertation, consideration has been given to modelling, optimisation, and plasmonic effects by using metallic nano antenna. In Chapter 1 I have mentioned the objectives and motivations behind this work. The benefits associated to work with nano structures. I have presented the difference between traditional and recent nano structures, and the effect of geometrical variations discussed so far. Finally, Chapter 1 ends with the history related development of nano antenna and the application and procedures which are involved in Nano antenna optimization/fabrications. I have also discussed the various application of this which are subsequently mentioned in the earlier chapters. Outlines of the work are briefly described according to the Chapter 1. Chapter 2 discusses the physics behind these nano antenna and I have discussed the techniques which dominantly considered metallic nano structures simulations. Henceforth, I have started from the basic of the *EM* waves such as Maxwell's Equations in both the forms and later on discussed about the Surface Plasmon Resonance and its characteristics which is induced when *EM* waves interacts with any metallic structures. Additionally, I have discussed the Drude-Lorentz model for accurate optimization of free electrons present in the metallic nano antennas. I have carried out all the simulation using FEM method with the help of COMSOL multiphysics. The main objectives was to develop a Finite Element Method (*FEM*) to clearly visualize the effect of nano antenna arrays in terms

Conclusion and Future Work

of domain and geometrical variations with less computation time. The advantage of using this finite element method with other numerical methods is briefly discussed in Chapter 2. This chapter also shows some benchmarking outcomes, as I have carried out these in order to build confidence as I embarked on new designs. I have compared the published results with our results which are generated from the in-house developed model. Computation domain is terminated by *PML* boundary to reduce the reflections from the outer boundaries in simulations. Several benchmarking results have been shown in Chapter 2 which shows the validity of in-house FEM model designed in COMSOL multiphysics to reduce the simulation times. Free space propagation of the electromagnetic wave has also been shown and the speed obtained with the in-house model is compared with the normalised value. Furthermore, I have use different meshes to optimise the results and checked the response of plasmonic peak. Regular and irregular mesh arrangements were considered and compared in terms of accuracy and convergency of the results. Irregular meshes can use dense mesh inside the core, while coarse mesh can be used outside the core to further reduce the computational times in comparison to when using a regular mesh arrangement. Chapter 3 discusses the modelling approaches used to evaluate the optical behaviour of the array surface are described in depth in this chapter. The nano particle and the substrate interaction has been discussed. This chapter also delves over the sensing mechanism with finite element method (*FEM*) modelling and the evolution of the computational model employed in the study. Chapter 4 presented the combination of paired gold nano structures developed based on its property of LSPRs and calculated the highest sensitivity as nearly 526-530 nm/RIU, around 110 nm *FWHM* and 8.1 Q-Factor achieved which can be used for the dedicated sensing applications. In this chapter, I have also shown the effect of the structure orientation on the sensitivity which is important aspect to overcome the fabrication imperfections of nano structures. *FEM* simulation results were perceived to give an optimum explanation of the presented designs, and this also showed the most substantial coupling effect in optimized design and the lesser effect of

the performance of further designs for plasmonic structures. The strongest transmission dip and reflection peak achieved at nearly 850 nm for optimized design while plasmonic loss shifted towards higher wavelength. Chapter 5 discussed a novel way to design and optimise electromagnetic plasmonic nanoparticles relying on an *ANN* based computationally inexpensive technique. The nano particles in this work were designed through using the Finite Element Method (*FEM*), and afterwards Artificial Intelligence (*AI*) has been used to predict associated sensitivity (*S*), Full Width Half Maximum (*FWHM*), Figure of Merit (*FOM*), and Surface plasmon resonance wavelength (*SPRW*) for various paired nanostructures. At commencement, a computational model is created by preparing the dataset using a Finite Element Method (*FEM*). To create the dataset, the input variables were the Major axis, *a*, the Minor axis, *b*, and the separation gap, *g*, were considered to determine the associated sensitivity (nm/RIU), *FWHM* (nm), *FOM*, and plasmonic wavelength (nm). Second, the neural network was created in such a way that the number of hidden layers and neurons were improved as part of a complete evaluation to increase the ML model's performance. This method was used to produce predictions for certain inputs and their related outcomes after successfully optimising the computational model. This chapter also examined the difference in inaccuracy between anticipated and simulated results. For estimating outputs for multiple input device settings, this methodology outperforms conventional computational. Chapter 6 presented a *DL* framework for transmission, reflection, and absorption spectra predictions by grasping the hidden correlation between the independent nanostructure properties and their corresponding optical responses. The proposed *DL* framework is shown to require a sufficient amount of training data to achieve an accurate approximation of the optical performance derived from computational models. A fully trained framework can outperform a traditional *EM* solution based on the COMSOL Multiphysics approach by three orders of magnitude. Furthermore, employing deep learning methodologies, the proposed *DL* framework makes an effort to optimise design elements that influence the geometrical

Conclusion and Future Work

dimensions of the nanostructure, offering insight into the universal transmission, reflection, and absorption spectrum predictions at the nanoscale. This paradigm improves the viability of complicated nanostructure design and analysis, and it has a lot of potential applications involving exotic light-matter interactions between nanostructures and electromagnetic fields. In terms of computational times, the designed algorithm is around 40 times faster as compare to conventional *FEM* method. Hence, this approach paves the way for fast yet universal methods for the characterization and analysis of the optical response of nanophotonic systems. Chapter 7 shows the study of a hybrid (*LiTaO₃* and *Al₂O₃*) stacked metallic nano plasmonic sensor. The designed and optimized sensor with $a = 100$ nm, $b = 10$ nm, $g = 10$ nm, $h_1 = 10$ nm, and $h_2 = 10$ nm has been evaluated in various surrounding refractive indices to calculate their corresponding sensitivity. The transmission, absorption, reflection spectra and modal field profiles have also been calculated to observe the sensor performance. The designed hybrid sensor has been compared with single metallic nanoantenna when $a = 100$ nm, $b = 10$ nm, $g = 10$ nm, and $h = 100$ nm to observe the sensitivity enhancement. From the results shown, it can be stated that the sensitivity can be enhanced by nearly 1.5 times by using *Al₂O₃* stacked antenna and more than 2 times by using *LiTaO₃*. It is also shown that sensitivity can be further increased by reducing metal height, h_1 and dielectric height, h_2 or separation distance, g . But for the fair comparison the values of these are taken as 10 nm. The normalized electric field intensity of the *LiTaO₃* and *Al₂O₃* stacked antennas were stronger, nearly 6.5×10^4 V/m and 5.4×10^4 V/m respectively, which was approximately more than 10.5 times of the single metallic nanostructure for *LiTaO₃* and 9 times for *Al₂O₃* stacked antenna. The proposed nano-enhanced antenna's sensitivity is proven by using of a full-wave electromagnetic simulation. Our suggested nano-antenna may be used for different nano inter- and intra-chip photonic sensor systems to develop cutting-edge detecting devices for measuring the quality of water, air, and soils. Furthermore, due of its wide frequency

coverage, this suggested antenna may be employed for biosensing, optical energy harvesting (also known as nano-rectenna or Nantenna) and optical sensing applications.

8.1 Future Scope

While above shown results obtained during this research are promising, but further work is required to improve the sensing mechanisms and evaluate the model. The required investigations, referring to both the innovative LSPR based biosensor and involvement of artificial intelligence, are described below.

8.1.1 Future possibilities in the LSPR based sensors

As I have to demonstrate the proposed nanoantenna and develop the innovative applications and designed geometries can enhance the performance in number of applications to help researchers to make the more efficient and compact devices. These days no one want to carry big and sophisticated devices and tools so this can be a great potential. Only a single unit cell device can detect the number of deceases in term of sensing application. I can also use this method to enhance the performance of nano solar cells implementation. Some researchers uses it in optical switching, and further work can be extended based on the plasmonic heat than I can kill the targeted molecules which are dangerous to humans or it would be a great candidate for targeting and treating a particular molecule which is very highly efficient application in medical field. The performance of this nano structures would be more than 100 times has been achieved compare to the ordinary device. Finally, this exciting and cutting edge research work are expected to create interest in exploiting these designs. Some issues as high computation cost are still untouched in this work, and I tried to improve this with the help of the artificial intelligence so it could show much more robustness in near future.

8.1.2 Future possibilities in the Artificial intelligence based optical properties predictions

The fascinating strength of *AI* is its capacity to solve a wide range of electromagnetic-based issues that are intractable by other known methodologies utilising a number of frameworks. It can thus yield not just new or improved solution and forecasts, but also additional physical knowledge into the system at present. Many of the world's top nano photonics research organisations already are researching into *AI* applications and building photonic *AI* implementations. Engineering of artificial electromagnetic materials is one of the major difficulties being tackled (optimization of metamaterial and other nanostructural geometries to achieve specific, targeted optical properties). Nano photonic technique, platform, and system architecture optimization (e.g. adaptively reconfigurable waveguide structures for arbitrary input/output operations). Photonic materials discovery, optimization, synthesis, and processing (identification of materials providing selected desirable properties for photonic applications). Sources of complicated electromagnetic fields, such as phase singularities, super-oscillatory foci, and so on, are being developed (design of field structures themselves and evolution of strategies for generating, characterising and utilising such fields). Photonic reservoirs, neuromorphic optical computing, photonic deep neural networks, all optical photonic cognitive networks, and optical oracles are all being developed. As a result, I can develop computationally cost-effective micro photonic structures, which are in high demand these days, utilising novel *AI*-based methods. I have also demonstrated the *AI* algorithm's potential to produce considerable outcomes. As a result, it can be concluded that the future of *AI* using plasmonics has a lot of potential in terms of avoiding excessive computing costs.

In near future this *AI* algorithm can be used for the reverse analysis as they greatly needed nanophotonic devices and brought optimized performance. However, the use of inverse design for plasmonic structures has been challenging due to local field concentrations that

can lead to errors in gradient calculation when the continuum adjoint method is used. On the other hand, with the discrete adjoint method one can achieve the exact gradient. Historically the discrete version is exclusively used with a Finite Element model, and applying the Finite Difference Time-Domain (*FDTD*) method in inverse design of plasmonic structures is rarely attempted. Due to the popularity of using FEM in simulating plasmonic structures, I can integrate the discrete adjoint method with Comsol and can present a framework to carry out inverse design of plasmonic structures using density-based topology optimization. In this way, I can demonstrate the exactness of the gradient calculation for a plasmonic block structure with varying permittivity. Another challenge that is unique with plasmonic structures is that non-physical amplification caused by poorly chosen material interpolation can destroy a stable convergence of the optimization. To avoid this, I can adopt a non-linear material interpolation scheme in the FEM solver. In addition, filtering-and-projection regularization is incorporated to ensure manufacturability of the designed structures. As an example of this framework, successful reconstruction of electric fields of different plasmonic apertures.

References

- [1] A. McWilliams, “The maturing nanotechnology market: products and applications,” *BCC Research: Wellesley, MA, USA*, pp. 8–20, 2016.
- [2] M. E. Vance, T. Kuiken, E. P. Vejerano, S. P. McGinnis, M. F. Hochella Jr, D. Rejeski, and M. S. Hull, “Nanotechnology in the real world: Redeveloping the nanomaterial consumer products inventory,” *Beilstein Journal of Nanotechnology*, vol. 6, no. 1, pp. 1769–1780, 2015.
- [3] J. Fletcher, “Electromagnetic wave energy converter,” Sep. 18 1973, US Patent 3,760,257.
- [4] F. Benfenati, E. Di Fabrizio, and V. Torre, *Novel Approaches for Single Molecule Activation and Detection*. Springer, 2014, vol. 4.
- [5] A. M. Marks, “Super submicron electron beam writer,” Jan. 17 1989, US Patent 4,798,959.
- [6] T. Atay, J.-H. Song, and A. V. Nurmikko, “Strongly interacting plasmon nanoparticle pairs: from dipole-dipole interaction to conductively coupled regime,” *Nano Letters*, vol. 4, no. 9, pp. 1627–1631, 2004.
- [7] B. Lahiri, A. Z. Khokhar, M. Richard, S. G. McMeekin, and N. P. Johnson, “Asymmetric split ring resonators for optical sensing of organic materials,” *Optics Express*, vol. 17, no. 2, pp. 1107–1115, 2009.
- [8] C. D’Andrea, J. Bochterle, A. Toma, C. Huck, F. Neubrech, E. Messina, B. Fazio, O. M. Marago, E. Di Fabrizio, d. Lamy, C. La, P. G. G. Marc, and A. Pucci, “Optical nanoantennas for multiband surface-enhanced infrared and Raman spectroscopy,” *ACS Nano*, vol. 7, no. 4, pp. 3522–3531, 2013.
- [9] J. Calderón, J. Álvarez, J. Martinez-Pastor, and D. Hill, “Bowtie plasmonic nanoantenna arrays for polarimetric optical biosensing,” in *Frontiers in Biological Detection: From Nanosensors to Systems VI*, vol. 8933. International Society for Optics and Photonics, 2014, p. 89330I.
- [10] H. Chen, A. M. Bhuiya, R. Liu, D. M. Wasserman, and K. C. Toussaint Jr, “Design, fabrication, and characterization of near-ir gold bowtie nanoantenna arrays,” *The Journal of Physical Chemistry C*, vol. 118, no. 35, pp. 20 553–20 558, 2014.

References

- [11] B. J. Roxworthy, K. D. Ko, A. Kumar, K. H. Fung, E. K. Chow, G. L. Liu, N. X. Fang, and K. C. Toussaint Jr, "Application of plasmonic bowtie nanoantenna arrays for optical trapping, stacking, and sorting," *Nano Letters*, vol. 12, no. 2, pp. 796–801, 2012.
- [12] J. Calderón, J. Álvarez, J. Martínez-Pastor, and D. Hill, "Polarimetric plasmonic sensing with bowtie nanoantenna arrays," *Plasmonics*, vol. 10, no. 3, pp. 703–711, 2015.
- [13] A. E. Cetin and H. Altug, "Fano resonant ring/disk plasmonic nanocavities on conducting substrates for advanced biosensing," *ACS Nano*, vol. 6, no. 11, pp. 9989–9995, 2012.
- [14] N. A. Cinel, S. Bütün, and E. Özbay, "Electron beam lithography designed silver nano-disks used as label free nano-biosensors based on localized surface plasmon resonance," *Optics Express*, vol. 20, no. 3, pp. 2587–2597, 2012.
- [15] J. Chen, P. Albella, Z. Pirzadeh, P. Alonso-González, F. Huth, S. Bonetti, V. Bonanni, J. Åkerman, J. Nogués, A. D. J. A. R. Vavassori, Paolo, and Hillenbrand, "Plasmonic nickel nanoantennas," *Small*, vol. 7, no. 16, pp. 2341–2347, 2011.
- [16] A. Kabashin, P. Evans, S. Pastkovsky, W. Hendren, G. Wurtz, R. Atkinson, R. Pollard, V. Podolskiy, and A. Zayats, "Plasmonic nanorod metamaterials for biosensing," *Nature Materials*, vol. 8, no. 11, p. 867, 2009.
- [17] S. Aksu, A. A. Yanik, R. Adato, A. Artar, M. Huang, and H. Altug, "High-throughput nanofabrication of infrared plasmonic nanoantenna arrays for vibrational nanospectroscopy," *Nano Letters*, vol. 10, no. 7, pp. 2511–2518, 2010.
- [18] I. Ament, J. Prasad, A. Henkel, S. Schmachtel, and C. Sonnichsen, "Single unlabeled protein detection on individual plasmonic nanoparticles," *Nano Letters*, vol. 12, no. 2, pp. 1092–1095, 2012.
- [19] R. M. Bakker, V. P. Drachev, Z. Liu, H.-K. Yuan, R. H. Pedersen, A. Boltasseva, J. Chen, J. Irudayaraj, A. V. Kildishev, and V. M. Shalaev, "Nanoantenna array-induced fluorescence enhancement and reduced lifetimes," *New Journal of Physics*, vol. 10, no. 12, p. 125022, 2008.
- [20] Z. Liu, A. Boltasseva, R. H. Pedersen, R. Bakker, A. V. Kildishev, V. P. Drachev, and V. M. Shalaev, "Plasmonic nanoantenna arrays for the visible," *Metamaterials*, vol. 2, no. 1, pp. 45–51, 2008.
- [21] R. Adato, A. A. Yanik, C.-H. Wu, G. Shvets, and H. Altug, "Radiative engineering of plasmon lifetimes in embedded nanoantenna arrays," *Optics Express*, vol. 18, no. 5, pp. 4526–4537, 2010.
- [22] N. Kumara, Y.-F. C. Chau, J.-W. Huang, H. J. Huang, C.-T. Lin, and H.-P. Chiang, "Plasmonic spectrum on 1d and 2d periodic arrays of rod-shape metal nanoparticle pairs with different core patterns for biosensor and solar cell applications," *Journal of Optics*, vol. 18, no. 11, p. 115003, 2016.

- [23] O. Limaj, D. Etezadi, N. J. Wittenberg, D. Rodrigo, D. Yoo, S.-H. Oh, and H. Altug, "Infrared plasmonic biosensor for real-time and label-free monitoring of lipid membranes," *Nano Letters*, vol. 16, no. 2, pp. 1502–1508, 2016.
- [24] B. Mehta and M. E. Zaghoul, "Effect of rounding on the sensitivity of optical antennas based sensors," in *Sensors, 2014*. IEEE, 2014, pp. 1391–1394.
- [25] S.-C. Lin, N. A. Hatab, B. Gu, B.-K. Chao, J.-H. Li, and C.-H. Hsueh, "Free-standing gold elliptical nanoantenna with tunable wavelength in near-infrared region for enhanced Raman spectroscopy," *Applied Physics A*, vol. 122, no. 7, p. 674, 2016.
- [26] T. Wang, Z. Zhang, F. Liao, Q. Cai, Y. Li, S.-T. Lee, and M. Shao, "The effect of dielectric constants on noble metal/semiconductor SERS enhancement: FDTD simulation and experiment validation of Ag/Ge and Ag/Si substrates," *Scientific Reports*, vol. 4, p. 4052, 2014.
- [27] Y. Yu-Yang, Y. Zong-Heng, L. Xiao-Nan, W. Jun, Z. Wen-Tao, and Y. Song, "Absorption enhancement and sensing properties of Ag diamond nanoantenna arrays," *Chinese Physics B*, vol. 24, no. 7, p. 074206, 2015.
- [28] N. Kumar and S. Kumbhat, *Essentials in Nanoscience and Nanotechnology*. John Wiley & Sons, 2016.
- [29] S. Bhaviripudi, E. Mile, S. A. Steiner, A. T. Zare, M. S. Dresselhaus, A. M. Belcher, and J. Kong, "CVD synthesis of single-walled carbon nanotubes from gold nanoparticle catalysts," *Journal of the American Chemical Society*, vol. 129, no. 6, pp. 1516–1517, 2007.
- [30] L. Yang and L. Yang, "Carbon nanostructures: New materials for orthopedic applications," *Nanotechnol.-Enhanc. Orthop. Mater*, vol. 6, no. 7, pp. 97–120, 2015.
- [31] J. Jeevanandam, A. Barhoum, Y. S. Chan, A. Dufresne, and M. K. Danquah, "Review on nanoparticles and nanostructured materials: history, sources, toxicity and regulations," *Beilstein Journal of Nanotechnology*, vol. 9, no. 1, pp. 1050–1074, 2018.
- [32] Z. Han, M. Luo, L. Chen, J. Chen, and C. Li, "A photoelectrochemical immunosensor for detection of α -fetoprotein based on Au-ZnO flower-rod heterostructures," *Applied Surface Science*, vol. 402, pp. 429–435, 2017.
- [33] Y. Dong, S. Li, H. Xu, M. Yan, X. Xu, X. Tian, Q. Liu, and L. Mai, "Wrinkled-graphene enriched MoO_3 nanobelts with increased conductivity and reduced stress for enhanced electrochemical performance," *Physical Chemistry Chemical Physics*, vol. 15, no. 40, pp. 17 165–17 170, 2013.
- [34] Y. Huang, H. Li, M.-S. Balogun, H. Yang, Y. Tong, X. Lu, and H. Ji, "Three-dimensional TiO_2/CeO_2 nanowire composite for efficient formaldehyde oxidation at low temperature," *RSC Advances*, vol. 5, no. 10, pp. 7729–7733, 2015.
- [35] H. H. Al-Kayiem, S. C. Lin, and A. Lukmon, "Review on nanomaterials for thermal energy storage technologies," *Nanoscience & Nanotechnology-Asia*, vol. 3, no. 1, pp. 60–71, 2013.

References

- [36] T. Y. Poh, N. Ali, M. Mac Aogáin, M. H. Kathawala, M. I. Setyawati, K. W. Ng, and S. H. Chotirmall, “Inhaled nanomaterials and the respiratory microbiome: clinical, immunological and toxicological perspectives,” *Particle and Fibre Toxicology*, vol. 15, no. 1, pp. 1–16, 2018.
- [37] Y. LeCun, Y. Bengio, and G. Hinton, “Deep learning,” *Nature*, vol. 521, no. 7553, pp. 436–444, 2015.
- [38] A. Massa, D. Marcantonio, X. Chen, M. Li, and M. Salucci, “DNNs as applied to electromagnetics, antennas, and propagation—a review,” *IEEE Antennas and Wireless Propagation Letters*, vol. 18, no. 11, pp. 2225–2229, 2019.
- [39] S. Chibani and F.-X. Coudert, “Machine learning approaches for the prediction of materials properties,” *APL Materials*, vol. 8, no. 8, p. 080701, 2020.
- [40] J. Zhou, B. Huang, Z. Yan, and J.-C. G. Bünzli, “Emerging role of machine learning in light-matter interaction,” *Light: Science & Applications*, vol. 8, no. 1, pp. 1–7, 2019.
- [41] R. T. Jones, “Machine learning methods in coherent optical communication systems,” *International Series of Monographs on Physics; Technical University of Denmark: Kongens Lyngby, Denmark*, 2019.
- [42] J. Baxter, A. C. Lesina, J.-M. Guay, and L. Ramunno, “Machine learning applications in plasmonics,” in *2018 Photonics North (PN)*. IEEE, 2018, pp. 1–1.
- [43] Z. A. Kudyshev, S. Bogdanov, A. V. Kildishev, A. Boltasseva, and V. M. Shalaev, “Machine learning assisted plasmonics and quantum optics,” in *Metamaterials, Metadevices, and Metasystems 2020*, vol. 11460. SPIE, 2020, p. 1146018.
- [44] E. Kakkava, B. Rahmani, N. Borhani, U. Teğın, D. Loterie, G. Konstantinou, C. Moser, and D. Psaltis, “Imaging through multimode fibers using deep learning: The effects of intensity versus holographic recording of the speckle pattern,” *Optical Fiber Technology*, vol. 52, p. 101985, 2019.
- [45] K. Schulz, R. Hänsch, and U. Sörgel, “Machine learning methods for remote sensing applications: an overview,” in *Earth resources and environmental remote sensing/GIS applications IX*, vol. 10790. International Society for Optics and Photonics, 2018, p. 1079002.
- [46] R. Horisaki, “Optical sensing and control based on machine learning,” in *In Computational Optical Sensing and Imaging 2018 Jun 25 (pp. CW3B-2)*. Optica Publishing Group. Optical Society of America, 2018, pp. CW3B–2.
- [47] M. J. Amin and N. Riza, “Machine learning enhanced optical distance sensor,” *Optics Communications*, vol. 407, pp. 262–270, 2018.
- [48] U. Michelucci, M. Baumgartner, and F. Venturini, “Optical oxygen sensing with artificial intelligence,” *Sensors*, vol. 19, no. 4, p. 777, 2019.
- [49] L. Ma, Y. Liu, X. Zhang, Y. Ye, G. Yin, and B. A. Johnson, “Deep learning in remote sensing applications: A meta-analysis and review,” *ISPRS Journal of Photogrammetry and Remote Sensing*, vol. 152, pp. 166–177, 2019.

- [50] Y. Khan, A. Samad, U. Iftikhar, S. Kumar, N. Ullah, J. Sultan, H. Ali, and M. L. Haider, "Mathematical modeling of photonic crystal based optical filters using machine learning," in *2018 International Conference on Computing, Electronic and Electrical Engineering (ICE Cube)*. IEEE, 2018, pp. 1–5.
- [51] K. A. Brown, S. Brittman, N. Maccaferri, D. Jariwala, and U. Celano, "Machine learning in nanoscience: big data at small scales," *Nano Letters*, vol. 20, no. 1, pp. 2–10, 2019.
- [52] X. Zhang, Z. Ma, H. Zheng, T. Li, K. Chen, X. Wang, C. Liu, L. Xu, X. Wu, D. Lin, and H. Lin, "The combination of brain-computer interfaces and artificial intelligence: applications and challenges," *Annals of Translational Medicine*, vol. 8, no. 11, 2020.
- [53] H.-C. Ruiz Euler, M. N. Boon, J. T. Wildeboer, B. van de Ven, T. Chen, H. Broersma, P. A. Bobbert, and W. G. van der Wiel, "A deep-learning approach to realizing functionality in nanoelectronic devices," *Nature nanotechnology*, vol. 15, no. 12, pp. 992–998, 2020.
- [54] H. Bai and S. Wu, "Deep-learning-based nanowire detection in afm images for automated nanomanipulation," *Nanotechnology and Precision Engineering*, vol. 4, no. 1, p. 013002, 2021.
- [55] G. M. Casañola-Martin and H. Pham, "Machine learning applications in nanomedicine and nanotoxicology: An overview," *International Journal of Applied Nanotechnology Research (IJANR)*, vol. 4, no. 1, pp. 1–7, 2019.
- [56] S. Raiyan Kabir, B. M. A. Rahman, A. Agrawal, and K. T. V. Grattan, "Elimination of numerical dispersion from electromagnetic time domain analysis by using resource efficient finite element technique," *Progress In Electromagnetics Research*, vol. 137, pp. 487–512, 2013.
- [57] C. R. Pollock, *Fundamentals of Optoelectronics*. Irwin, 1995.
- [58] G. R. Werner and J. R. Cary, "A stable FDTD algorithm for non-diagonal, anisotropic dielectrics," *Journal of Computational Physics*, vol. 226, no. 1, pp. 1085–1101, 2007.
- [59] G. R. Werner, C. A. Bauer, and J. R. Cary, "A more accurate, stable, FDTD algorithm for electromagnetics in anisotropic dielectrics," *Journal of Computational Physics*, vol. 255, pp. 436–455, 2013.
- [60] M. Clemens and T. Weiland, "Discrete electromagnetism with the finite integration technique," *Progress In Electromagnetics Research*, vol. 32, pp. 65–87, 2001.
- [61] B. M. A. Rahman and A. Agrawal, *Finite Element Modeling Methods for Photonics*. Artech House, 2013.
- [62] R. W. Wood, "On a remarkable case of uneven distribution of light in a diffraction grating spectrum," *Proceedings of the Physical Society of London*, vol. 18, no. 1, p. 269, 1902.
- [63] S. A. Maier, *Plasmonics: Fundamentals and Applications*. Springer, 2007, vol. 1.

References

- [64] J. Sambles, G. Bradbery, and F. Yang, “Optical excitation of surface plasmons: an introduction,” *Contemporary physics*, vol. 32, no. 3, pp. 173–183, 1991.
- [65] P. B. Johnson and R.-W. Christy, “Optical constants of the noble metals,” vol. 6, no. 12, p. 4370, 1972.
- [66] D. J. Barber and I. C. Freestone, “An investigation of the origin of the colour of the lycurgus cup by analytical transmission electron microscopy,” *Archaeometry*, vol. 32, no. 1, pp. 33–45, 1990.
- [67] G. Mie, “Beiträge zur optik trüber medien, speziell kolloidaler metallösungen,” *Annalen der Physik*, vol. 330, no. 3, pp. 377–445, 1908.
- [68] C. Louis and O. Pluchery, *Gold nanoparticles for physics, chemistry and biology*. World Scientific, 2017.
- [69] T. Wriedt, “Mie theory: a review,” *The Mie Theory*, pp. 53–71, 2012.
- [70] R. Gans, “Über die form ultramikroskopischer goldteilchen,” *Annalen der Physik*, vol. 342, no. 5, pp. 881–900, 1912.
- [71] S. W. Prescott and P. Mulvaney, “Gold nanorod extinction spectra,” *Journal of Applied Physics*, vol. 99, no. 12, p. 123504, 2006.
- [72] Mieplot. [Online]. Available: <http://www.philiplaven.com/mieplot.htm>
- [73] P. Chylek and J. Zhan, “Absorption and scattering of light by small particles: the interference structure,” *Applied Optics*, vol. 29, no. 28, pp. 3984–3984, 1990.
- [74] J. Cottom, P. Abellan, F. Hage, Q. Ramasse, K. Critchley, and R. Brydson, “Fabrication and characterisation of an adaptable plasmonic nanorod array for solar energy conversion,” in *Journal of Physics: Conference Series*, vol. 902, no. 1. IOP Publishing, 2017, p. 012025.
- [75] S. Farooq and R. E. de Araujo, “Engineering a localized surface plasmon resonance platform for molecular biosensing,” *Open Journal of Applied Sciences*, vol. 8, no. 3, pp. 126–139, 2018.
- [76] S. Rizzato, E. Primiceri, A. G. Monteduro, A. Colombelli, A. Leo, M. G. Manera, R. Rella, and G. Maruccio, “Interaction-tailored organization of large-area colloidal assemblies,” *Beilstein Journal of Nanotechnology*, vol. 9, no. 1, pp. 1582–1593, 2018.
- [77] L. Wu, P. Bai, X. Zhou, and E. Li, “Reflection and transmission modes in nanoholearray-based plasmonic sensors,” *IEEE Photonics Journal*, vol. 4, no. 1, pp. 26–33, 2011.
- [78] E. Synge, “Xxxviii. a suggested method for extending microscopic resolution into the ultra-microscopic region,” *The London, Edinburgh, and Dublin Philosophical Magazine and Journal of Science*, vol. 6, no. 35, pp. 356–362, 1928.
- [79] J. Wessel, “Surface-enhanced optical microscopy,” *JOSA B*, vol. 2, no. 9, pp. 1538–1541, 1985.

- [80] H. Fischer and O. J. Martin, "Engineering the optical response of plasmonic nanoantennas," *Optics Express*, vol. 16, no. 12, pp. 9144–9154, 2008.
- [81] J. N. Anker, W. P. Hall, O. Lyandres, N. C. Shah, J. Zhao, and R. P. Van Duyne, "Biosensing with plasmonic nanosensors," *Nanoscience and Technology: A Collection of Reviews from Nature Journals*, pp. 308–319, 2010.
- [82] L. B. Sagle, L. K. Ruvuna, J. A. Ruemmele, and R. P. Van Duyne, "Advances in localized surface plasmon resonance spectroscopy biosensing," *Nanomedicine*, vol. 6, no. 8, pp. 1447–1462, 2011.
- [83] C.-T. Chou Chao, Y.-F. Chou Chau, H. J. Huang, N. Kumara, M. R. R. Kooh, C. M. Lim, and H.-P. Chiang, "Highly sensitive and tunable plasmonic sensor based on a nanoring resonator with silver nanorods," *Nanomaterials*, vol. 10, no. 7, p. 1399, 2020.
- [84] R. E. Armstrong, M. Horáček, and P. Zijlstra, "Plasmonic assemblies for real-time single-molecule biosensing," *Small*, vol. 16, no. 52, p. 2003934, 2020.
- [85] E. Mauriz and L. M. Lechuga, "Plasmonic biosensors for single-molecule biomedical analysis," *Biosensors*, vol. 11, no. 4, p. 123, 2021.
- [86] K. V. Sreekanth, Y. Alapan, M. ElKabbash, E. Ilker, M. Hinczewski, U. A. Gurkan, A. De Luca, and G. Strangi, "Extreme sensitivity biosensing platform based on hyperbolic metamaterials," *Nature Materials*, vol. 15, no. 6, pp. 621–627, 2016.
- [87] Y. Lee, S.-J. Kim, H. Park, and B. Lee, "Metamaterials and metasurfaces for sensor applications," *Sensors*, vol. 17, no. 8, p. 1726, 2017.
- [88] D. Garoli, E. Calandrini, G. Giovannini, A. Hubarevich, V. Caligiuri, and F. De Angelis, "Nanoporous gold metamaterials for high sensitivity plasmonic sensing," *Nanoscale Horizons*, vol. 4, no. 5, pp. 1153–1157, 2019.
- [89] C. F. Bohren and D. R. Huffman, *Absorption and Scattering of Light by Small Particles*. John Wiley & Sons, 2008.
- [90] P. Swanglap, L. S. Slaughter, W.-S. Chang, B. Willingham, B. P. Khanal, E. R. Zubarev, and S. Link, "Seeing double: coupling between substrate image charges and collective plasmon modes in self-assembled nanoparticle superstructures," *ACS Nano*, vol. 5, no. 6, pp. 4892–4901, 2011.
- [91] P. Nordlander and E. Prodan, "Plasmon hybridization in nanoparticles near metallic surfaces," *Nano Letters*, vol. 4, no. 11, pp. 2209–2213, 2004.
- [92] M. W. Knight, Y. Wu, J. B. Lassiter, P. Nordlander, and N. J. Halas, "Substrates matter: influence of an adjacent dielectric on an individual plasmonic nanoparticle," *Nano Letters*, vol. 9, no. 5, pp. 2188–2192, 2009.
- [93] R. P. Van Duyne, A. J. Haes, and A. D. McFarland, "Nanoparticle optics: sensing with nanoparticle arrays and single nanoparticles," in *Physical Chemistry of Interfaces and Nanomaterials II*, vol. 5223. International Society for Optics and Photonics, 2003, pp. 197–207.

References

- [94] J. I. Chen, Y. Chen, and D. S. Ginger, "Plasmonic nanoparticle dimers for optical sensing of dna in complex media," *Journal of the American Chemical Society*, vol. 132, no. 28, pp. 9600–9601, 2010.
- [95] D. Punj, R. Regmi, A. Devilez, R. Plauchu, S. B. Moparthi, B. Stout, N. Bonod, H. Rigneault, and J. Wenger, "Self-assembled nanoparticle dimer antennas for plasmonic-enhanced single-molecule fluorescence detection at micromolar concentrations," *ACS Photonics*, vol. 2, no. 8, pp. 1099–1107, 2015.
- [96] W. Zhao, S. Xiao, Y. Zhang, D. Pan, J. Wen, X. Qian, D. Wang, H. Cao, W. He, M. Quan *et al.*, "Binary "island" shaped arrays with high-density hot spots for surface-enhanced Raman scattering substrates," *Nanoscale*, vol. 10, no. 29, pp. 14 220–14 229, 2018.
- [97] C.-Y. Tsai, J.-W. Lin, C.-Y. Wu, P.-T. Lin, T.-W. Lu, and P.-T. Lee, "Plasmonic coupling in gold nanoring dimers: observation of coupled bonding mode," *Nano Letters*, vol. 12, no. 3, pp. 1648–1654, 2012.
- [98] K.-P. Chen, V. P. Drachev, J. D. Borneman, A. V. Kildishev, and V. M. Shalaev, "Drude relaxation rate in grained gold nanoantennas," *Nano Letters*, vol. 10, no. 3, pp. 916–922, 2010.
- [99] V. P. Drachev, A. V. Kildishev, J. D. Borneman, K.-P. Chen, V. M. Shalaev, K. Yamnitskiy, R. A. Norwood, N. Peyghambarian, L. A. P. S. W. T. R. E. D. J. H. Marder, Seth R, and E. W. V. Stryland, "Engineered nonlinear materials using gold nanoantenna array," *Scientific Reports*, vol. 8, no. 1, pp. 1–9, 2018.
- [100] S. Cakmakyapan, N. A. Cinel, A. O. Cakmak, and E. Ozbay, "Validation of electromagnetic field enhancement in near-infrared through sierpinski fractal nanoantennas," *Optics Express*, vol. 22, no. 16, pp. 19 504–19 512, 2014.
- [101] Y. Sun and Y. Xia, "Increased sensitivity of surface plasmon resonance of gold nanoshells compared to that of gold solid colloids in response to environmental changes," *Analytical Chemistry*, vol. 74, no. 20, pp. 5297–5305, 2002.
- [102] H. Chen, X. Kou, Z. Yang, W. Ni, and J. Wang, "Shape-and size-dependent refractive index sensitivity of gold nanoparticles," *Langmuir*, vol. 24, no. 10, pp. 5233–5237, 2008.
- [103] W. J. Galush, S. A. Shelby, M. J. Mulvihill, A. Tao, P. Yang, and J. T. Groves, "A nanocube plasmonic sensor for molecular binding on membrane surfaces," *Nano Letters*, vol. 9, no. 5, pp. 2077–2082, 2009.
- [104] M. D. Malinsky, K. L. Kelly, G. C. Schatz, and R. P. Van Duyne, "Chain length dependence and sensing capabilities of the localized surface plasmon resonance of silver nanoparticles chemically modified with alkanethiol self-assembled monolayers," *Journal of the American Chemical Society*, vol. 123, no. 7, pp. 1471–1482, 2001.
- [105] S. Nishiuma, Y. Handa, T. Imamura, M. Ogino, T. Yamada, K. Furusawa, and R. Kuroda, "Localized surface plasmon resonant metal nanostructures as refractive index sensors," *Japanese Journal of Applied Physics*, vol. 47, no. 3R, p. 1828, 2008.

- [106] S.-W. Lee, K.-S. Lee, J. Ahn, J.-J. Lee, M.-G. Kim, and Y.-B. Shin, “Highly sensitive biosensing using arrays of plasmonic au nanodisks realized by nanoimprint lithography,” *ACS Nano*, vol. 5, no. 2, pp. 897–904, 2011.
- [107] J. McPhillips, A. Murphy, M. P. Jonsson, W. R. Hendren, R. Atkinson, F. Hook, A. V. Zayats, and R. J. Pollard, “High-performance biosensing using arrays of plasmonic nanotubes,” *ACS Nano*, vol. 4, no. 4, pp. 2210–2216, 2010.
- [108] N. Laman and D. Grischkowsky, “Terahertz conductivity of thin metal films,” *Applied Physics Letters*, vol. 93, no. 5, 2008.
- [109] B. Rahmani, D. Loterie, G. Konstantinou, D. Psaltis, and C. Moser, “Multimode optical fiber transmission with a deep learning network,” *Light: Science & Applications*, vol. 7, no. 1, pp. 1–11, 2018.
- [110] G. A. Silva, “A new frontier: The convergence of nanotechnology, brain machine interfaces, and artificial intelligence,” *Frontiers in Neuroscience*, p. 843, 2018.
- [111] J. Smajic, C. Hafner, L. Raguin, K. Tavzarashvili, and M. Mishrikey, “Comparison of numerical methods for the analysis of plasmonic structures,” *Journal of Computational and Theoretical Nanoscience*, vol. 6, no. 3, pp. 763–774, 2009.
- [112] P. R. Wiecha and O. L. Muskens, “Deep learning meets nanophotonics: a generalized accurate predictor for near fields and far fields of arbitrary 3d nanostructures,” *Nano Letters*, vol. 20, no. 1, pp. 329–338, 2019.
- [113] W. McKinney, “Pandas, python data analysis library,” URL <http://pandas.pydata.org>, 2015.
- [114] F. Pedregosa, G. Varoquaux, A. Gramfort, V. Michel, B. Thirion, O. Grisel, M. Blondel, P. Prettenhofer, D. V. Weiss, Ron, J. Vanderplas, A. Passos, D. Cournapeau, M. Brucher, M. Perrot, and E. Duchesnay, “Scikit-learn: Machine learning in python,” *The Journal of Machine Learning Research*, vol. 12, pp. 2825–2830, 2011.
- [115] W. McKinney, *Python for data analysis: Data wrangling with Pandas, NumPy, and IPython*. O’Reilly Media, Inc., 2012.
- [116] H. Miller, P. Haller, E. Burmako, and M. Odersky, “Instant pickles: Generating object-oriented pickler combinators for fast and extensible serialization,” in *Proceedings of the 2013 ACM SIGPLAN International Conference on Object oriented programming systems languages & applications*, 2013, pp. 183–202.
- [117] B. Lorica, “Why AI and machine learning researchers are beginning to embrace pytorch,” O’Reilly Media Radar: Farnham, UK, 2017.
- [118] A. D. I. Pytorch, “Pytorch,” 2018.
- [119] S. Yegulalp, “Facebook brings GPU-powered machine learning to python,” *InfoWorld*, vol. 19, 2017.
- [120] M. Patel, “When two trends fuse: Pytorch and recommender systems,” O’Reilly Media. [https://www.oreilly.com/ideas/when-two-trends-fuse-pytorch . . .](https://www.oreilly.com/ideas/when-two-trends-fuse-pytorch...), 2018.

References

- [121] R. Collobert, K. Kavukcuoglu, and C. Farabet, “Torch7: A matlab-like environment for machine learning,” in *BigLearn, NIPS workshop*, no. CONF, 2011.
- [122] S. Verma, S. Ghosh, and B. M. A. Rahman, “All-opto plasmonic-controlled bulk and surface sensitivity analysis of a paired nano-structured antenna with a label-free detection approach,” *Sensors*, vol. 21, no. 18, p. 6166, 2021.
- [123] F. N. Khan, Q. Fan, C. Lu, and A. P. T. Lau, “An optical communication’s perspective on machine learning and its applications,” *Journal of Lightwave Technology*, vol. 37, no. 2, pp. 493–516, 2019.
- [124] D. P. Kingma and J. Ba, “Adam: A method for stochastic optimization,” *arXiv preprint arXiv:1412.6980*, 2014.
- [125] Y.-F. C. Chau, C.-T. C. Chao, H. J. Huang, U. Anwar, C. M. Lim, N. Y. Voo, A. H. Mahadi, N. Kumara, and H.-P. Chiang, “Plasmonic perfect absorber based on metal nanorod arrays connected with veins,” *Results in Physics*, vol. 15, p. 102567, 2019.
- [126] G. A. Seber and A. J. Lee, *Linear regression analysis*. John Wiley & Sons, 2012.
- [127] X. Ni, Z. J. Wong, M. Mrejen, Y. Wang, and X. Zhang, “An ultrathin invisibility skin cloak for visible light,” *Science*, vol. 349, no. 6254, pp. 1310–1314, 2015.
- [128] A. V. Kildishev, A. Boltasseva, and V. M. Shalaev, “Planar photonics with metasurfaces,” *Science*, vol. 339, no. 6125, p. 1232009, 2013.
- [129] N. Yu and F. Capasso, “Flat optics with designer metasurfaces,” *Nature Materials*, vol. 13, no. 2, pp. 139–150, 2014.
- [130] P. Albella, M. A. Poyli, M. K. Schmidt, S. A. Maier, F. Moreno, J. J. Sáenz, and J. Aizpurua, “Low-loss electric and magnetic field-enhanced spectroscopy with sub-wavelength silicon dimers,” *The Journal of Physical Chemistry C*, vol. 117, no. 26, pp. 13 573–13 584, 2013.
- [131] A. Kinkhabwala, Z. Yu, S. Fan, Y. Avlasevich, K. Müllen, and W. E. Moerner, “Large single-molecule fluorescence enhancements produced by a bowtie nanoantenna,” *Nature Photonics*, vol. 3, no. 11, pp. 654–657, 2009.
- [132] A. B. Evlyukhin, C. Reinhardt, and B. N. Chichkov, “Multipole light scattering by nonspherical nanoparticles in the discrete dipole approximation,” *Physical Review B*, vol. 84, no. 23, p. 235429, 2011.
- [133] B. T. Draine and P. J. Flatau, “Discrete-dipole approximation for scattering calculations,” *JOSA A*, vol. 11, no. 4, pp. 1491–1499, 1994.
- [134] J.-M. Jin, *The Finite Element Method in Electromagnetics*. John Wiley & Sons, 2015.
- [135] “Comsol multiphysics® v. 5.6. www.comsol.com. comsol AB, Stockholm, Sweden.”
- [136] R. F. Harrington, *Field Computation by Moment Methods*. Wiley-IEEE Press, 1993.

-
- [137] A. Taflove, S. C. Hagness, and M. Picket-May, “Computational electromagnetics: The finite-difference time-domain method,” *The Electrical Engineering Handbook*, vol. 3, 2005.
- [138] “FDTD: 3d electromagnetic simulator lumerical inc. Artech: Norwood, MA, 2005.”
- [139] J. Chen and Q. H. Liu, “Discontinuous Galerkin time-domain methods for multiscale electromagnetic simulations: A review,” *Proceedings of the IEEE*, vol. 101, no. 2, pp. 242–254, 2012.
- [140] Q. Zhan, Q. Sun, Q. Ren, Y. Fang, H. Wang, and Q. H. Liu, “A discontinuous Galerkin method for simulating the effects of arbitrary discrete fractures on elastic wave propagation,” *Geophysical Journal International*, vol. 210, no. 2, pp. 1219–1230, 2017.
- [141] P. Wen, Q. Ren, J. Chen, A. Chen, and Y. Zhang, “Improved memory-efficient subdomain level discontinuous Galerkin time domain method for periodic/quasi-periodic structures,” *IEEE Transactions on Antennas and Propagation*, vol. 68, no. 11, pp. 7471–7479, 2020.
- [142] N. Liu, M. Hentschel, T. Weiss, A. P. Alivisatos, and H. Giessen, “Three-dimensional plasmon rulers,” *Science*, vol. 332, no. 6036, pp. 1407–1410, 2011.
- [143] C. Sönnichsen, B. M. Reinhard, J. Liphardt, and A. P. Alivisatos, “A molecular ruler based on plasmon coupling of single gold and silver nanoparticles,” *Nature Biotechnology*, vol. 23, no. 6, pp. 741–745, 2005.
- [144] P. Baldi, P. Sadowski, and D. Whiteson, “Searching for exotic particles in high-energy physics with deep Learning,” *Nature Communications*, vol. 5, no. 1, pp. 1–9, 2014.
- [145] W. J. Brouwer, J. D. Kubicki, J. O. Sofo, and C. L. Giles, “An investigation of machine learning methods applied to structure prediction in condensed matter,” *arXiv preprint arXiv:1405.3564*, 2014.
- [146] K. Hansen, G. Montavon, F. Biegler, S. Fazli, M. Rupp, M. Scheffler, O. A. Von Lilienfeld, A. Tkatchenko, and K.-R. Müller, “Assessment and validation of machine learning methods for predicting molecular atomization energies,” *Journal of Chemical Theory and Computation*, vol. 9, no. 8, pp. 3404–3419, 2013.
- [147] P. B. Wigley, P. J. Everitt, A. van den Hengel, J. W. Bastian, M. A. Sooriyabandara, G. D. McDonald, K. S. Hardman, C. D. Quinlivan, P. Manju, C. C. Kuhn, I. R. Petersen, J. J. H. A. N. Luiten, N. P. Robins, and M. R. Hush, “Fast machine-learning online optimization of ultra-cold-atom experiments,” *Scientific Reports*, vol. 6, no. 1, pp. 1–6, 2016.
- [148] L. Waller and L. Tian, “Machine learning for 3d microscopy,” *Nature*, vol. 523, no. 7561, pp. 416–417, 2015.
- [149] C. L. Chen, A. Mahjoubfar, L.-C. Tai, I. K. Blaby, A. Huang, K. R. Niazi, and B. Jalali, “Deep learning in label-free cell classification,” *Scientific Reports*, vol. 6, no. 1, pp. 1–16, 2016.

References

- [150] K. Yao, R. Unni, and Y. Zheng, “Intelligent nanophotonics: merging photonics and artificial intelligence at the nanoscale,” *Nanophotonics*, vol. 8, no. 3, pp. 339–366, 2019.
- [151] A. Y. Piggott, J. Lu, K. G. Lagoudakis, J. Petykiewicz, T. M. Babinec, and J. Vučković, “Inverse design and demonstration of a compact and broadband on-chip wavelength demultiplexer,” *Nature Photonics*, vol. 9, no. 6, pp. 374–377, 2015.
- [152] Y. Li, Y. Xu, M. Jiang, B. Li, T. Han, C. Chi, F. Lin, B. Shen, X. Zhu, L. Lai, and Z. Fang, “Self-learning perfect optical chirality via a deep neural network,” *Physical Review Letters*, vol. 123, no. 21, p. 213902, 2019.
- [153] I. Goodfellow, Y. Bengio, and A. Courville, *Deep Learning*. MIT press, 2016.
- [154] L. Noriega, “Multilayer perceptron tutorial,” *Lecture Series, School of Computing, Staffordshire University*, 2005.
- [155] K. O’Shea and R. Nash, “An introduction to convolutional neural networks,” *arXiv preprint arXiv:1511.08458*, 2015.
- [156] L. Medsker and L. C. Jain, *Recurrent neural networks: design and applications*. CRC press, 1999.
- [157] L. Metz, B. Poole, D. Pfau, and J. Sohl-Dickstein, “Unrolled generative adversarial networks,” *arXiv preprint arXiv:1611.02163*, 2016.
- [158] H. Im, H. Shao, Y. I. Park, V. M. Peterson, C. M. Castro, R. Weissleder, and H. Lee, “Label-free detection and molecular profiling of exosomes with a nano-plasmonic sensor,” *Nature Biotechnology*, vol. 32, no. 5, pp. 490–495, 2014.
- [159] P. Strobbia, E. R. Languirand, and B. M. Cullum, “Recent advances in plasmonic nanostructures for sensing: A review,” *Optical Engineering*, vol. 54, no. 10, p. 100902, 2015.
- [160] M. I. Stockman, “Nanoplasmonic sensing and detection,” *Science*, vol. 348, no. 6232, pp. 287–288, 2015.
- [161] V. G. Kravets, A. V. Kabashin, W. L. Barnes, and A. N. Grigorenko, “Plasmonic surface lattice resonances: a review of properties and applications,” *Chemical Reviews*, vol. 118, no. 12, pp. 5912–5951, 2018.
- [162] C. Valsecchi and A. G. Brolo, “Periodic metallic nanostructures as plasmonic chemical sensors,” *Langmuir*, vol. 29, no. 19, pp. 5638–5649, 2013.
- [163] F. Amato, A. López, E. M. Peña-Méndez, P. Vañhara, A. Hampl, and J. Havel, “Artificial neural networks in medical diagnosis,” *Journal of Applied Biomedicine*, vol. 11, no. 2, pp. 47–58, 2013.
- [164] J. J. Wang, L. Chen, S. Tai, X. Deng, P. F. Sciortino, J. Deng, and F. Liu, “Wafer-based nanostructure manufacturing for integrated nano optic devices,” *Journal of Lightwave Technology*, vol. 23, no. 2, p. 474, 2005.

- [165] X. Y. Xiong, L. J. Jiang, W. E. Sha, Y. H. Lo, and W. C. Chew, "Compact nonlinear yagi-uda nanoantennas," *Scientific Reports*, vol. 6, no. 1, pp. 1–9, 2016.
- [166] C. A. Thraskias, E. N. Lallas, N. Neumann, L. Schares, B. J. Offrein, R. Henker, D. Plettemeier, F. Ellinger, J. Leuthold, and I. Tomkos, "Survey of photonic and plasmonic interconnect technologies for intra-datacenter and high-performance computing communications," *IEEE Communications Surveys & Tutorials*, vol. 20, no. 4, pp. 2758–2783, 2018.
- [167] J. Guo, J. Li, C. Liu, Y. Yin, W. Wang, Z. Ni, Z. Fu, H. Yu, Y. Xu, Y. Shi *et al.*, "High-performance silicon- graphene hybrid plasmonic waveguide photodetectors beyond 1.55 μm ," *Light: Science & Applications*, vol. 9, no. 1, pp. 1–11, 2020.
- [168] M. Klein, B. H. Badada, R. Binder, A. Alfrey, M. McKie, M. R. Koehler, D. G. Mandrus, T. Taniguchi, K. Watanabe, B. J. LeRoy, and J. R. Schaibley, "2D semiconductor nonlinear plasmonic modulators," *Nature Communications*, vol. 10, no. 1, pp. 1–7, 2019.
- [169] M. Cohen, R. Shavit, and Z. Zalevsky, "Enabling high efficiency nanoplasmonics with novel nanoantenna architectures," *Scientific Reports*, vol. 5, no. 1, pp. 1–9, 2015.
- [170] L. Lin and Y. Zheng, "Optimizing plasmonic nanoantennas via coordinated multiple coupling," *Scientific Reports*, vol. 5, no. 1, pp. 1–11, 2015.
- [171] G. N. Malheiros-Silveira, G. S. Wiederhecker, and H. E. Hernández-Figueroa, "Dielectric resonator antenna for applications in nanophotonics," *Optics Express*, vol. 21, no. 1, pp. 1234–1239, 2013.
- [172] L. Novotny and N. Van Hulst, "Antennas for light," *Nature Photonics*, vol. 5, no. 2, pp. 83–90, 2011.
- [173] Z. Pan and J. Guo, "Enhanced optical absorption and electric field resonance in diabolical metal bar optical antennas," *Optics Express*, vol. 21, no. 26, pp. 32 491–32 500, 2013.
- [174] T. D. James, T. J. Davis, and A. Roberts, "Optical investigation of the j-pole and vee antenna families," *Optics Express*, vol. 22, no. 2, pp. 1336–1341, 2014.
- [175] L. Yousefi and A. C. Foster, "Waveguide-fed optical hybrid plasmonic patch nanoantenna," *Optics Express*, vol. 20, no. 16, pp. 18 326–18 335, 2012.
- [176] K. J. Ooi, P. Bai, M. X. Gu, and L. K. Ang, "Design of a monopole-antenna-based resonant nanocavity for detection of optical power from hybrid plasmonic waveguides," *Optics Express*, vol. 19, no. 18, pp. 17 075–17 085, 2011.
- [177] D. Dai and S. He, "A silicon-based hybrid plasmonic waveguide with a metal cap for a nano-scale light confinement," *Optics Express*, vol. 17, no. 19, pp. 16 646–16 653, 2009.
- [178] M. Alam, J. Meier, J. Aitchison, and M. Mojahedi, "Propagation characteristics of hybrid modes supported by metal-low-high index waveguides and bends," *Optics Express*, vol. 18, no. 12, pp. 12 971–12 979, 2010.

References

- [179] D. Dai, Y. Shi, S. He, L. Wosinski, and L. Thylen, “Gain enhancement in a hybrid plasmonic nano-waveguide with a low-index or high-index gain medium,” *Optics Express*, vol. 19, no. 14, pp. 12 925–12 936, 2011.
- [180] N. Kashyap, Z. A. Wani, R. Jain, V. Dinesh Kumar *et al.*, “Investigation of a nanostrip patch antenna in optical frequencies,” *Applied Physics A*, vol. 117, no. 2, pp. 725–729, 2014.
- [181] M. Saad-Bin-Alam, M. I. Khalil, A. Rahman, and A. M. Chowdhury, “Hybrid plasmonic waveguide fed broadband nanoantenna for nanophotonic applications,” *IEEE Photonics Technology Letters*, vol. 27, no. 10, pp. 1092–1095, 2015.
- [182] L. Yousefi, “Highly directive hybrid plasmonic leaky wave optical nano-antenna,” *Progress In Electromagnetics Research Letters*, vol. 50, pp. 85–90, 2014.
- [183] P. Sharma and V. D. Kumar, “Investigation of multilayer planar hybrid plasmonic waveguide and bends,” *Electronics Letters*, vol. 52, no. 9, pp. 732–734, 2016.
- [184] P. Sharma and D. Kumar, V, “All optical logic gates using hybrid metal insulator metal plasmonic waveguide,” *IEEE Photonics Technology Letters*, vol. 30, no. 10, pp. 959–962, 2018.
- [185] P. Sharma and D. Kumar, “Hybrid insulator metal insulator planar plasmonic waveguide-based components,” *IEEE Photonics Technology Letters*, vol. 29, no. 16, pp. 1360–1363, 2017.
- [186] P. Biagioni, J.-S. Huang, and B. Hecht, “Nanoantennas for visible and infrared radiation,” *Reports on Progress in Physics*, vol. 75, no. 2, p. 024402, 2012.
- [187] R. Fernández-García, Y. Sonnefraud, A. I. Fernández-Domínguez, V. Giannini, and S. A. Maier, “Design considerations for near-field enhancement in optical antennas,” *Contemporary Physics*, vol. 55, no. 1, pp. 1–11, 2014.
- [188] T. Feichtner, O. Selig, M. Kiunke, and B. Hecht, “Evolutionary optimization of optical antennas,” *Physical Review Letters*, vol. 109, no. 12, p. 127701, 2012.
- [189] Z. Zhu, B. Bai, O. You, Q. Li, and S. Fan, “Fano resonance boosted cascaded optical field enhancement in a plasmonic nanoparticle-in-cavity nanoantenna array and its sers application,” *Light: Science & Applications*, vol. 4, no. 6, pp. e296–e296, 2015.
- [190] K. J. Savage, M. M. Hawkeye, R. Esteban, A. G. Borisov, J. Aizpurua, and J. J. Baumberg, “Revealing the quantum regime in tunnelling plasmonics,” *Nature*, vol. 491, no. 7425, pp. 574–577, 2012.
- [191] C. Ciraci, R. Hill, J. Mock, Y. Urzhumov, A. Fernández-Domínguez, S. Maier, J. Pendry, A. Chilkoti, and D. Smith, “Probing the ultimate limits of plasmonic enhancement,” *Science*, vol. 337, no. 6098, pp. 1072–1074, 2012.
- [192] T. B. Hoang, G. M. Akselrod, and M. H. Mikkelsen, “Ultrafast room-temperature single photon emission from quantum dots coupled to plasmonic nanocavities,” *Nano Letters*, vol. 16, no. 1, pp. 270–275, 2016.

- [193] P. Anger, P. Bharadwaj, and L. Novotny, “Enhancement and quenching of single-molecule fluorescence,” *Physical Review Letters*, vol. 96, no. 11, p. 113002, 2006.
- [194] G. M. Akselrod, M. C. Weidman, Y. Li, C. Argyropoulos, W. A. Tisdale, and M. H. Mikkelsen, “Efficient nanosecond photoluminescence from infrared PbS quantum dots coupled to plasmonic nanoantennas,” *ACS Photonics*, vol. 3, no. 10, pp. 1741–1746, 2016.
- [195] F. Zhou, Y. Liu, and W. Cai, “Huge local electric field enhancement in hybrid plasmonic arrays,” *Optics Letters*, vol. 39, no. 5, pp. 1302–1305, 2014.
- [196] Y. Bao, Y. Hou, and Z. Wang, “Huge electric field enhancement of magnetic resonator integrated with multiple concentric rings,” *Plasmonics*, vol. 10, no. 2, pp. 251–256, 2015.
- [197] W. Li and Y. Hou, “Electromagnetic field hugely enhanced by coupling to optical energy focusing structure,” *Optics Express*, vol. 25, no. 7, pp. 7358–7368, 2017.
- [198] J.-N. Liu, Q. Huang, K.-K. Liu, S. Singamaneni, and B. T. Cunningham, “Nanoantenna–microcavity hybrids with highly cooperative plasmonic–photonic coupling,” *Nano Letters*, vol. 17, no. 12, pp. 7569–7577, 2017.
- [199] A. I. Kuznetsov, A. E. Miroshnichenko, M. L. Brongersma, Y. S. Kivshar, and B. Luk’yanchuk, “Optically resonant dielectric nanostructures,” *Science*, vol. 354, no. 6314, p. aag2472, 2016.
- [200] Z.-J. Yang, R. Jiang, X. Zhuo, Y.-M. Xie, J. Wang, and H.-Q. Lin, “Dielectric nanoresonators for light manipulation,” *Physics Reports*, vol. 701, pp. 1–50, 2017.
- [201] M. Decker and I. Staude, “Resonant dielectric nanostructures: a low-loss platform for functional nanophotonics,” *Journal of Optics*, vol. 18, no. 10, p. 103001, 2016.
- [202] M. Khorasaninejad and F. Capasso, “Metalenses: Versatile multifunctional photonic components,” *Science*, vol. 358, no. 6367, p. eaam8100, 2017.
- [203] E. Arbabi, A. Arbabi, S. M. Kamali, Y. Horie, and A. Faraon, “Controlling the sign of chromatic dispersion in diffractive optics with dielectric metasurfaces,” *Optica*, vol. 4, no. 6, pp. 625–632, 2017.
- [204] S. Jahani and Z. Jacob, “All-dielectric metamaterials,” *Nature Nanotechnology*, vol. 11, no. 1, pp. 23–36, 2016.
- [205] X. Zhu, W. Yan, U. Levy, N. A. Mortensen, and A. Kristensen, “Resonant laser printing of structural colors on high-index dielectric metasurfaces,” *Science Advances*, vol. 3, no. 5, p. e1602487, 2017.
- [206] R. M. Bakker, D. Permyakov, Y. F. Yu, D. Markovich, R. Paniagua-Domínguez, L. Gonzaga, A. Samusev, Y. Kivshar, B. Luk’yanchuk, and A. I. Kuznetsov, “Magnetic and electric hotspots with silicon nanodimers,” *Nano Letters*, vol. 15, no. 3, pp. 2137–2142, 2015.

References

- [207] M. Caldarola, P. Albella, E. Cortés, M. Rahmani, T. Roschuk, G. Grinblat, R. F. Oulton, A. V. Bragas, and S. A. Maier, “Non-plasmonic nanoantennas for surface enhanced spectroscopies with ultra-low heat conversion,” *Nature Communications*, vol. 6, no. 1, pp. 1–8, 2015.
- [208] Y. Yang, V. A. Zenin, and S. I. Bozhevolnyi, “Anapole-assisted strong field enhancement in individual all-dielectric nanostructures,” *ACS Photonics*, vol. 5, no. 5, pp. 1960–1966, 2018.
- [209] Z.-J. Yang, Q. Zhao, and J. He, “Boosting magnetic field enhancement with radiative couplings of magnetic modes in dielectric nanostructures,” *Optics Express*, vol. 25, no. 14, pp. 15 927–15 937, 2017.
- [210] H. Wang, P. Liu, Y. Ke, Y. Su, L. Zhang, N. Xu, S. Deng, and H. Chen, “Janus magneto–electric nanosphere dimers exhibiting unidirectional visible light scattering and strong electromagnetic field enhancement,” *ACS Nano*, vol. 9, no. 1, pp. 436–448, 2015.
- [211] R. Guo, E. Rusak, I. Staude, J. Dominguez, M. Decker, C. Rockstuhl, I. Brener, D. N. Neshev, and Y. S. Kivshar, “Multipolar coupling in hybrid metal–dielectric metasurfaces,” *ACS Photonics*, vol. 3, no. 3, pp. 349–353, 2016.
- [212] T. Feng, Y. Xu, W. Zhang, and A. E. Miroshnichenko, “Ideal magnetic dipole scattering,” *Physical Review Letters*, vol. 118, no. 17, p. 173901, 2017.
- [213] T. Shibanuma, G. Grinblat, P. Albella, and S. A. Maier, “Efficient third harmonic generation from metal–dielectric hybrid nanoantennas,” *Nano Letters*, vol. 17, no. 4, pp. 2647–2651, 2017.
- [214] Z.-J. Yang, Q. Zhao, Y.-H. Deng, D. Zhang, and J. He, “Efficient second harmonic generation in gold–silicon core–shell nanostructures,” *Optics Express*, vol. 26, no. 5, pp. 5835–5844, 2018.
- [215] Q. Zhao, Z.-J. Yang, and J. He, “Fano resonances in heterogeneous dimers of silicon and gold nanospheres,” *Frontiers of Physics*, vol. 13, no. 3, pp. 1–7, 2018.
- [216] Y. Yang, O. D. Miller, T. Christensen, J. D. Joannopoulos, and M. Soljagic, “Low-loss plasmonic dielectric nanoresonators,” *Nano Letters*, vol. 17, no. 5, pp. 3238–3245, 2017.
- [217] A. Devilez, B. Stout, and N. Bonod, “Compact metallo-dielectric optical antenna for ultra directional and enhanced radiative emission,” *ACS nano*, vol. 4, no. 6, pp. 3390–3396, 2010.
- [218] K. Moutzouris, G. Hloupis, I. Stavrakas, D. Triantis, and M.-H. Chou, “Temperature dependent visible to near-infrared optical properties of 8 mol% mg-doped lithium tantalate,” *Optical Materials Express*, vol. 1, no. 3, pp. 458–465, 2011.